1984

# New laser spectroscopic technique for stable-isotope ratio analysis

William G. Tong
*Iowa State University*

## Recommended Citation

Tong, William G., "New laser spectroscopic technique for stable-isotope ratio analysis " (1984). *Retrospective Theses and Dissertations*. 8222.
https://lib.dr.iastate.edu/rtd/8222

INFORMATION TO USERS

This reproduction was made from a copy of a document sent to us for microfilming. While the most advanced technology has been used to photograph and reproduce this document, the quality of the reproduction is heavily dependent upon the quality of the material submitted.

The following explanation of techniques is provided to help clarify markings or notations which may appear on this reproduction.

1. The sign or "target" for pages apparently lacking from the document photographed is "Missing Page(s)". If it was possible to obtain the missing page(s) or section, they are spliced into the film along with adjacent pages. This may have necessitated cutting through an image and duplicating adjacent pages to assure complete continuity.

2. When an image on the film is obliterated with a round black mark, it is an indication of either blurred copy because of movement during exposure, duplicate copy, or copyrighted materials that should not have been filmed. For blurred pages, a good image of the page can be found in the adjacent frame. If copyrighted materials were deleted, a target note will appear listing the pages in the adjacent frame.

3. When a map, drawing or chart, etc., is part of the material being photographed, a definite method of "sectioning" the material has been followed. It is customary to begin filming at the upper left hand corner of a large sheet and to continue from left to right in equal sections with small overlaps. If necessary, sectioning is continued again—beginning below the first row and continuing on until complete.

4. For illustrations that cannot be satisfactorily reproduced by xerographic means, photographic prints can be purchased at additional cost and inserted into your xerographic copy. These prints are available upon request from the Dissertations Customer Services Department.

5. Some pages in any document may have indistinct print. In all cases the best available copy has been filmed.

University
Microfilms
International

300 N. Zeeb Road
Ann Arbor, MI 48106

8505876

Tong, William G.

# NEW LASER SPECTROSCOPIC TECHNIQUE FOR STABLE-ISOTOPE RATIO ANALYSIS

*Iowa State University* Ph.D. 1984

University
Microfilms
International 300 N. Zeeb Road, Ann Arbor, MI 48106

# New laser spectroscopic technique for stable-isotope ratio analysis

by

William G Tong

A Dissertation Submitted to the
Graduate Faculty in Partial Fulfillment of the
Requirements for the Degree of
DOCTOR OF PHILOSOPHY

Department: Chemistry
Major: Analytical Chemistry

Approved:

In Charge of Major Work

For the Major Department

For the Graduate College

Iowa State University
Ames, Iowa

1984

## TABLE OF CONTENTS

# CHAPTER I. INTRODUCTION TO LASER OPTOGALVANIC SPECTROSCOPY

## Review

The development of efficient and powerful tunable lasers has revolutionized spectroscopy and opened a new class of spectroscopic techniques that take advantage of the unique properties of these lasers. The tremendous impact of lasers on spectroscopy in the past several years has been documented with an avalanche of publications. Laser spectroscopy has achieved improvements in selectivity, accuracy and spectral resolution to levels previously thought impractical.

Among the several different types of narrow-bandwidth tunable lasers developed in the past decade, the organic dye laser has been the most prominent type used in atomic and molecular spectroscopy. This new powerful spectroscopic tool has led to an accelerated growth in the nonlinear spectroscopy of atoms and molecules. Availability of wide tunable spectral region, the narrow spectral bandwidth and strong intensity per unit spectral range of these dye lasers have made it feasible to expand the realm of classic spectroscopic techniques such as; absorption, emission and fluorescence spectroscopy. Atomic energy levels which previously could not be efficiently excited by conventional light sources can now be studied by selective step-wise excitation using these new dye lasers.

Technological advances have made it possible to achieve extremely small spectral linewidth in lasers. This yields a spectral resolution which may exceed that of the largest spectrographs by several orders of magnitude. Spectroscopists no longer need giant spectrographs to study hyperfine structures. In laser spectroscopy, the resolution is often not limited by the instrumental bandwidth but rather by the spectral linewidth of the absorbing or emitting atoms or molecules.

The main goal of the research presented in this dissertation is the development of laser optogalvanic spectroscopy as an analytical tool to study atomic hyperfine structure and to analyze isotope ratio at high spectral resolution using tunable single frequency ring dye laser. Laser optogalvanic (LOG) spectroscopy is a simple, sensitive and powerful technique (1) with applications in many areas of research such as combustion and plasma physics high resolution atomic and molecular spectroscopy, trace element detection and chemical analysis (2). Discovered more than fifty years ago by Penning (3), the optogalvanic effect has awaited the development of tunable lasers to demonstrate its extensive applicability. Many advantages of LOG spectroscopy over conventional absorption methods will be presented in the course of this chapter. Hyperfine structure and isotope shifts of Cu I 578.2 nm transition are examined in the next chapter. Also discussed are the calculation of hyperfine component strength and the determination of copper 63 and copper 65 isotope ratio by matching theorectical and experimental Doppler-limited optogalvanic spectra. Some relevant advantages of this isotope ratio analysis scheme over conventional technique such as mass spectrometry is presented.

Optogalvanic signals arise when the impedance of electrical gas discharges changes in responce to the absorption of laser radiation by atomic or molecular species present in the discharge. Large changes of impedance can be induced by laser wavelengths corresponding to nonionizing transitions of species present. By monitoring the change in voltage across the discharge tube and scanning the wavelength of the laser probing the discharge, an optogalvanic spectrum can be conveniently recorded. This technique is a valuable spectroscopic tool since the discharge is both a source and a convenient detector for atoms and molecules. Because the optogalvanic effect relies on a voltage change, no optical measurement is required in observing the absorption process. Consequently, problems associated with the measurement of weak signals such as collection efficiency and scattered excitation light do not limit the sensitivity and dynamic range. This simple and sensitive spectroscopic technique has been applied in analytical chemistry (4 - 7), wavelength measurements and calibration (8 - 10), laser stabilization (11), atomic ion transitions (12 - 20) and isotope enrichment (21,22). More recently LOG spectroscopy using discharges has demostrated its applicability for studying molecular species (23 - 27).

In these LOG spectroscopic techniques, lasers have been used to pump atomic or molecular transitions by single-photon excitation while relying upon resultant changes in thermal or collisional ionization to yield galvanic signals. Sensitivity of LOG spectroscopy is greatly enhanced by using multiphoton excitation techniques. Ausschnitt et al. demonstrated the application of multiphoton optogalvanic spectroscopy to hydrogen plasma diagnostics (28). Large enhancements of optogalvanic signal in hollow cathode tubes, up to two orders of magnitude, were obtained by Shuker et al. (29) and by

Wakata et al. (30) using two-photon excitation scheme.

Some new LOG spectroscopic techniques were demonstrated by several groups. Cornelissen and Burgmans studied the Stark broadening and Stark shift of the sodium 3S-4D transition in a Na-Ne discharge using Doppler-free two-photon spectroscopy (31). Schawlow et al. measured hyperfine splitting using intermodulated optogalvanic spectroscopy, a new method of Doppler-free saturation spectroscopy (32,33). Siegel et al. studied Molybdenum isotope shifts in a hollow cathode discharge tube with Doppler-free intermodulated fluorescence and optogalvanic spectroscopy and observed a homogeneous linewidth of 25 MHz (34). Suzuki observed optogalvanic effects in a radio-frequency (rf) discharge (35). The rf LOG spectroscopy is particularly useful for studying unstable molecules which are reactive to metal electrodes in a conventional discharge tube. Apel et al. demonstrated that the optogalvanic effect in a hollow cathode discharge can be used as an element specific detector without the use of a laser or an expensive monochromator (36).

As stated in the preceding paragraphs, many areas of research have benefited from the optogalvanic effect in the discharge. LOG has also proven to be a powerful spectroscopic tool using atmospheric pressure analytical flames. To detect optogalvanic signal in a flame, a constant voltage source is passed through the flame and the resulting change in flame conductivity in response to the absorption of tunable laser light is monitored. This new technique is not limited by the many noise sources of conventional flame spectrometry (37 - 39), while maintaining the advantages of the analytical flame, such as continuous and convenient sampling, ease of operation and low cost.

Green et al. (40) first reported the optogalvanic effect in flames or laser-enhanced ionization, and later improved the technique and demonstrated its applicability to analytical chemistry (5, 41 - 45). Schenck et al. first reported the application of LOG in flame to study molecular species (46). Turk et al. demonstrated that step-wise excitation laser-enhanced ionization (LEI), utilizing two electronic transitions connected by a common intermediate level, yields improved degree of selectivity and detection limits over single-photon LEI (47,48). Zalewski et al. proved that optogalvanic effect in a hollow cathode discharge can be used as a selective detector specific to the intracavity absorption of analyte species in a flame, thus eliminating the need for a high resolution spectrograph (49). A good review of LEI spectroscopy is given by Travis et al. (50).

The mechanism of optogalvanic effect (OGE) was first postulated in 1925 by Foote and Mohler (51) and later observed experimentally by Penning (3). Mohler explained that ionization events, resulted in photoexcitation of atomic cesium in a thermionic didode cell, were not purely thermal collisional-energy augmentation process, and later proved the process to be associative ionization (52):

$$2\,Cs \xrightarrow{h\nu} Cs^* + Cs \longrightarrow Cs_2^* \longrightarrow Cs_2^+ + e^- \tag{1}$$

where the outer electron is promoted to the ionization potential by a sequence of collisional and optical excitations.

In 1928, Penning observed a change in the voltage drop across a neon discharge when illuminated by a second neon discharge and explained that the light from the second discharge perturbed the energy level populations in the first discharge and hence changed the ionization rate. These early observations of optical enhancement of collisional ionization had awaited the advent of lasers to be fully appreciated as a great potential for development of a valuable spectroscopic tool.

Optogalvic effect (OGE), the production of ionization by a combination collisional and discrete optical processes, is presented in Figure 1. Since both resonance and non-resonance transitions are possible for laser optogalvanic spectroscopy, it has also proved to be a spectroscopic technique with high selectivity. It also allows one to choose a suitable excitation wavelength where there is minimal spectral interference from impurity or from the Ne discharge gas. Many resonance and non-resonance lines of several elements have been successfully used for LOG spectroscopy. The sodium 589.0 nm resonance transition line yields one of the strongest LOG signals (1). An example of non-resonance transition line that provide good LOG signal is Cu I 578.2 nm line. Detailed study of this transition line is presented in the following chapters.

Because of the complicated plasma physics involved in the discharges, magnitude and polarity of LOG signals in hollow cathode lamps vary depending on the discharge conditions and on the nature of the atomic states being radiatively coupled. There are four possible processes by which a sputtered analyte species M may be ionized in a neon discharge:

Figure 1. Energy level representation of resonance optogalvanic effect (a) and non-resonance optogalvanic effect (b)

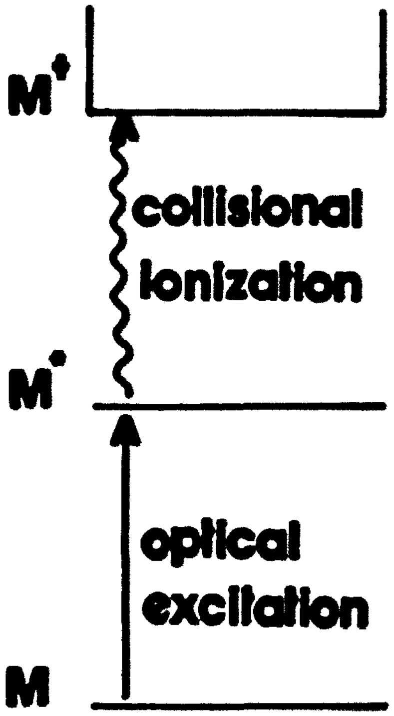

RESONANCE
OGE

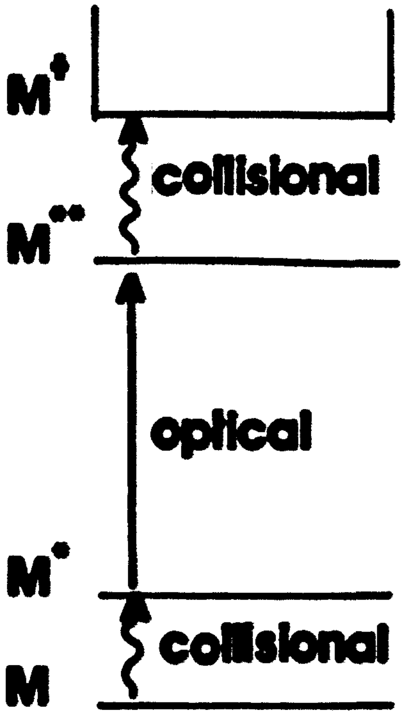

NON-
RESONANCE
OGE

1. Penning ionization

$$Ne^{*} + M \longrightarrow M^{+} + Ne + e^{-} \qquad (2)$$

2. Electron impact

$$M + e^{-} \longrightarrow M^{+} + 2e^{-} \qquad (3)$$

3. Photoionization

$$M + h\nu \longrightarrow M^{+} + e^{-} \qquad (4)$$

4. Charge transfer

$$Ne^{+} + M \longrightarrow M^{+} + Ne \qquad (5)$$

where M is an atomic species (a sputtered metal atom) and Ne is a metastable neon excited state. These possible mechanisms were investigated for analyte (minor) species when the laser wavelength was tuned to a neon discharge gas transition (53). As expected, it was demonstrated that electron impact ionization is the dominant mode of ionization at normal operating discharge current (10 - 40 mA), due to the increased electron flux in the hollow cathode cavity. It is interesting to note that at low discharge current (5 mA), Penning ionization become the dominant ionization process. Collisional excitation energy generated in the hollow cathode cavity could be optimized by using a proper design and geometry of cathode.

In rare gas discharge lamps, the various allowed electronic transitions yield LOG signals of different polarity. The more common type, negative LOG signal, corresponds to optical transition which enhanced the net collisional ionization rate in the discharge. When the absorbed radiation produces transitions to higher states from which electron collisional ionization proceeds more easily, the discharge voltage will decrease, because the electron temperature (electric field) required to sustain the ionization rate is decreased. However, when the absorbed radiation depletes a well-populated metastable level, higher electron temperature is required to sustain the discharge and hence increasing the discharge voltage (6, 8, 21). At normal operating discharge current (10 - 40 mA), the first effect plays a dominant role. As discharge current increases, both the net collisional ionization and the cathode sputtering efficiency increase.

Since electric field, electron concentration, electron energy distribution and neon excited state concentration vary across the cathode cavity, the magnitude and polarity of LOG signal varies as different parts of the cathode cavity are irradiated. More relevant characteristics and parameter of hollow cathode discharges are discussed in a later chapter along with the design of demountable hollow cathode lamp.

## Relevant Laser Properties

LOG spectroscopy is one of the many new spectroscopic techniques which have benefited from the advent of the lasers. It is important to discuss some relevant characteristics of lasers that make them unique as an excitation source for LOG spectroscopy.

### Monochromaticity

Hyperfine structure studies by high resolution spectroscopy demand extremely small spectral linewidth and high monochromaticity of lasers. Doppler broadening of the spectral line of atoms in a gas is in the order of a few GHz or about $10^{-6}$ times the frequency. (For example, the Doppler width of Cu I 578.2 nm line is about 1.5 GHz or 0.0017 nm at 2 - 10 torr of gas pressure.) It is very difficult to resolve these narrow atomic lines using conventional light sources and spectrometers. Conventional light sources which emit many statistically independent wave trains have linewidths that are many orders of magnitude wider than Doppler widths of atoms and molecules. Also, the resolution of a conventional spectrometer is instrumentally limited. On the contrary, laser linewidth as small as a few MHz or even KHz is achievable and hence the resolving power of laser spectroscopy is limited by the spectral linewidth of the atoms or molecules under study rather than the linewidth of the laser. Using Doppler-free spectroscopic techniques (54, 55), even sub-Doppler resolution can be achieved. Higher spectral resolution also enhances signal and improves detection sensitivity in absorption spectroscopy (54).

Great selectivity enhancement of monochromatic laser light over conventional light sources is one of the most important advantages of lasers. The narrow laser linewidth favors the selectivity of optical excitation and results in the exclusive population of single atomic or molecular state. This allows one to perform spectroscopy of not only electronic ground states but also that of excited states. Using a laser, one could selectively study an atomic transition in the presence of many other absorbing or emitting species with little or no spectral interference. Selectivity is further enhanced by using multiphoton step-wise excitation schemes.

Monochromaticity of lasers can be advantageously used for stray-light rejection in conventional spectroscopy such as emission and fluorescence spectroscopy. However, it is not necessary for LOG spectroscopy which is insensitive to stray light or any kind of light scattering since no optical measurement is made.

## Tunability

Lasers with tunable wavelength region ranging from the vacuum ultraviolet to the submillimeter are now available. The frequency of these lasers can be tuned within a narrow absorption or fluorescence linewidth around the appropriate frequency with a wide variety of tuning speed. Rapid scan rate could be used for spectroscopic investigations of short-lived intermediate radicals in chemical reactions. More frequency stabilized and slower scan mechanism could be used for line profile measurements of absorbing atomic and molecular transitions with high accuracy. The single-frequency ring dye laser employed in this research work is an example of these new generation lasers which can scan several GHz around the transition frequency in single-mode with a minimum of frequency jitter. This kind of tuning capability is certainly necessary for accurate measurements of isotope shifts in atomic hyperfine structures.

### Power

Considering the sharp linewidth and the narrow beam divergence attainable, the laser is incomparable in spectral power density. The energy density per unit frequency interval available is many orders of magnitude higher than conventional incoherent light sources. The power density is further amplified by several orders of magnitude when the laser beam is focused to a spot of very small dimension. This allows one to utilize laser photon fluxes for irradiation of very small volumes with high efficiency. High power density could also significantly reduce detector or background noise and hence improve the signal-to-noise ratio. Large excitation intensity is also useful in new nonlinear spectroscopic techniques such as Doppler-free two-photon excitation (31) and saturation spectroscopy (32, 33, 34), which yield higher resolution and selectivity.

### Spatial coherence

The laser emits very directive beam of spatially coherent light. Spatial coherence of the laser output depends on the resonant modes and spatial distributions of the electromagnetic fields in the laser cavity. For the linearly-polarized transverse electromagnetic (TEM) field, eigenmodes exist in the optical cavity which has finite rectangular or circular mirror apertures. The eigenmodes of rectangular symmetry can be designated by TEM $_{ijk}$ where i, j and k-1 are the number of modes in the x, y and z directions respectively; with z direction being the axis of the cavity. Since the cross-sectional field distribution of a mode in the xy plane is almost independent of the large number of longitudinal modes k, it is easier to use TEM to represent these field patterns. The amplitude of the laser light exhibits a Gaussian distribution around the beam axis when the laser is operated using the lowest-order mode, namely TEM $_{00}$. The optical field across the beam is

$$E(r) = E_0 \exp ( - r^2 / w^2 ) \tag{6}$$

where w is the beam radius at the beam waist. The angular distribution of the optical field can be represented as

$$E(\theta) = A \exp [- ( \theta / d\theta )^2 ] \tag{7}$$

where $d\theta$ is the beam divergence and related to wavelength and beam waist by

$$d\theta = \lambda / \Pi w \tag{8}$$

A laser beam of uniphase $TEM_{00}$ mode has the lowest diffraction loss and the electric field has a constant phase across the entire wavefront. It also has the smallest angular divergence outside the cavity and the beam can be focused down to the smallest spot size to obtain highest power density. The spot size is given by $fd\theta$, where $f$ is the focal length. Conventional spatially-incoherent light, with many TEM modes present, can not be focused without sacrificing power. Thus, lasers have definite advantage for spectroscopic methods which require high spatial resolution. Since the magnitude of optogalvanic signal varies as different parts of the hollow cathode cavity are irradiated, it is important to use a well-collimated laser beam to achieve spatially optimized LOG signal. Concentration of the laser beam intensity also yields a strong optical field, which can induce a wide variety of nonlinear optical effects in multiphoton LOG spectroscopic techniques.

### Temporal coherence

The ability of pulsed or mode-locked lasers to provide short and intense light pulses with pulse widths as narrow as $10^{-14}$ s allows the study of fast transient phenomena. High temporal resolution of pulsed lasers can be advantageously used to investigate transient laser transition rates using pulsed optogalvanic effect (16). Time resolution is also useful for discrimination of stray radiation and Rayleigh scattering in some spectroscopic detection such as fluorescence; but it is not necessary for LOG detection since no optical measurement is made. However pulsed optogalvanic signal collection can be employed to suppress electrical interferences using appropriate synchronous detection and electronic gating (45). Nonlinear LOG spectroscopic techniques enjoy the high peak power available from pulsed lasers (28, 29, 48).

### Polarization

Lasers are either normally plane polarized or forced to be plane polarized by the use of intracavity optics. This laser property is useful in some light-detecting spectroscopic methods for rejection of Raman and Rayleigh scattering by using proper orientation of the detector with respect to the laser polarization. It is not applicable to LOG spectroscopy since LOG detection scheme is insensitive to any kind of optical background noise. However, laser polarization can be advantageously used to study some polarization dependent optogalvanic effects to obtain new spectral information. It was demonstrated that different optogalvanic signals were observed for some nonlinear transition schemes when irradiated by a linearly polarized laser and a circularly polarized laser (30). The new information obtained from polarization dependent LOG signals could be used to assist spectral assignment of complicated spectra.

## Advantages of Laser Optogalvanic Spectroscopy

As discussed in the preceding sections, it is apparent that optogalvanic detection scheme has been successfully employed in an increasing number of linear and nonlinear spectroscopic techniques. The principle advantages of LOG spectroscopy that have attracted spectroscopists from many research areas are outlined here.

### Direct electrical signal generation

In LOG spectroscopy electrical signal is directly generated from optical absorption. Since the primary signal is electric, no intermediate step of optical-to-electrical transformation is necessary for signal display. Because no optical detection is made, it also eliminates all collection and dispersion optics, monochromators, photodiodes and photomultipliers. The best feature is the fact that all optical background noises such as Rayleigh and Raman scattering, room light and flame background noise are irrelevant in LOG spectroscopy.

### Narrow linewidth

Most laser linewidths are much narrower than the Doppler or Lorenzian linewidths of atoms in discharge or flame. Since the electrical signal is generated directly from optical absorption in LOG spectroscopy, the experimental resolution is limited by the analyte bandwidth rather than the spectrometer slit function as in conventional spectroscopic technique.

### Selectivity

Taking advantage of useful contribution of collisional processes, it is feasible to observe optogalvanic effect in discharges for both resonance and non-resonance transitions. The unsual sensitivity of non-resonance lines (transitions originating from excited states) in addition to resonance lines allows one to choose an appropriate excitation wavelength where there is minimal spectral interference.

High selectivity also help in confirmation of spectral identifications in complicated spectra.

### Sensitivity

Detection limits of several elements established for flame LOG spectroscopy vary depending on the ionization potential of the element. Although sensitivity for some elements (Sr, Cr, Pd, Cu) does not seem to be as good as that of other flame spectroscopic techniques, many others yield much superior detection limits. For example, Li detection limit of 1 pg/ml is approaching the theorectical limit of 100 % ionization and collection efficiency (50). For Na, the potential sensitivity exceeds the ability of the researcher to avoid contamination during sample preparation.

### Collisional excitation

In fluorescence spectrometry, collisional processes often decrease the quantum efficiency (56). Conversely in LOG spectroscopy, collisional processes are the essential forces for the overall excitation scheme. Furthermore, high-lying metastable states play a special role in collisional ionization rate in a rare gas discharge (57). They could induce a large energy level change that is many times the energy of the excitation photons, by getting promoted to a short-lived state and then rapidly decaying to the ground state (58). This energy amplification yields enhancement of collisional ionization rate, because the collisional ionization rate is exponentially proportional to the electron binding energy (59).

### Multiphoton optogalvanic effect

Transitions from ground states to high-lying level (7.2 eV) normally have low absorption coefficients and require very high laser power at short wavelengths. These problems can be overcome by using multiphoton excitation schemes where absorption cross sections are generally more favorable. Sensitivity improvement of a few orders of magnitude was demonstrated for two-photon stepwise excitation (47). Selectivity is also significantly improved since the probability of both transitions simultaneously coinciding with two transitions of another element is extremely small. Several oxides of refractory elememts (46) and non- volatile metals and compounds have also been successfully analyzed by LOG spectroscopy using analytical flames.

### Dynamic range

Linear dynamic range of 4 - 5 orders of magnitude has been observed for several elements.

### Effective use of higher laser power

In laser-induced fluorescence spectroscopy, if too much laser power is used, optical absorption is saturated while source light scattering increases proportionally with laser power. Optical and electrical saturation also restrict the signal increase with laser power in LOG spectroscopy. However, because of the absence of optical noise generation, LOG spectroscopy has the advantage of having higher limit of useful laser power.

# CHAPTER II. INTRODUCTION TO ANALYSIS OF ATOMIC HYPERFINE STRUCTURE

## Review

Hyperfine structures and isotope shifts of optical transitions have been studied for several elements since the early observation of hyperfine splitting by Merton in 1919 (60) and the interpretation of nuclear structure from it by Bohr in 1922 (61). Many spectroscopic techniques have been developed for the analysis of hyperfine structures and precision measurements of electric and magnetic moments of the nucleus. Before the advent of lasers, high spectral resolution necessary to study hyperfine splittings was achieved by using Fabry-Perot etalons and several variations of specially designed hollow cathode lamps (62 - 70). Atomic beam sources (70 - 73) were also developed and used to minimize the Doppler broadening of the linewidths. Improved Fabry-Perot interferometers were used later to study isotope shifts in many elements including Sn (74), Pb II (75), Mo (76, 77), Hf II (78), Ni (79), and Ce (80). Steudel, Heilig and many other workers employed Fabry-Perot spectrometers with scanning and recording capabilities to measure isotope shifts of light elements (81, 82) and several other nuclei (83 - 90). Other kinds of interferometers such as Hilger quartz Lummer-Gehrcke interferometer (91) and reflecting Echelon interferometer (92) were also demonstrated to be useful. While interferometers seemed to be the choice tool for hyperfine structure studies at the time, some workers still enjoyed reasonable results using more conventional but elaborate tools such as Fastie-Ebert type vacuum spectrograph with photographic recording (93), or 9.1-m focal-length Czerny-Turner type spectrometer (94). In addition to the hyperfine structure analysis of stable elements, some studies have also been done on unstable short-lived isotopes (95) and radio-active materials (96, 97).

Although hyperfine structure studies have been made for several decades, it was not until the recent developments of tunable dye lasers that measurements for a large number of elements with high spectral resolution and precision were possible at optical transitions ranging from infrared to ultra-violet regions. New laser-based techniques were developed and many optical transitions for several elements were studied at a rapid pace. Griffith et al. suggested measuring hyperfine splittings with high accuracy by determining the heterodyne beat frequency between two lasers locked to different transitions of atoms in an atomic beam (98). Lewis et al. employed continuous wave (cw) tunable dye laser and atomic-beam techniques to achieve improved sensitivity and significant narrowing of linewidth (99, 100). Doppler-free saturation spectroscopy (101) and two-photon techniques (102 - 106) were utilized by other workers.

Constant improvement of dye laser technology assures increasing accuracy and reliability of hyperfine structure measurements for more elements. In this chapter and in Chapter III, we will discuss the measurement of hyperfine splittings using a state-of-the-art ring dye laser and the optogalvanic detection scheme.

## Analysis of Atomic Hyperfine Structure

Since Michelson (107) and Fabry and Perot (108) discovered nearly a century ago that there were groups of closely spaced lines inside a fine structure, many suggestions have been made to explain the theory behind the complex of these components. Initially it was assumed that different isotopes emitted at slightly shifted frequencies because of the difference in nuclear mass. However, this effect alone was not enough to explain the rather wide range that hyperfine components could spread out. For example, Pb-207 isotope could disperse its four hyperfine components in a range as wide as 18 GHz or 0.6 $cm^{-1}$ in the Pb I 601.2 nm transition. Furthermore, splitting of hyperfine components was still observed even after eliminating the isotope shift effect by using a pure single-isotope source element. It was Pauli (109) who first proposed that hyperfine splitting was due to the interaction of the magnetic moment of the nucleus with the magnetic field induced by the electrons. So it became clear that the experimentally observed groups of closely spaced lines were indeed the result of both isotope shift effect and hyperfine splitting. Isotope shift is dependent on the mass difference of isotopes and the changes in the radial moments of the nuclear charge distribution between isotopes, while hyperfine splitting is due to the nuclear-electron electric and magnetic interactions. The development of quantum mechanics accelerated the process of understanding the nuclear and atomic properties, and many theoretical developments were made on both hyperfine splitting and isotope shift effects.

For the benefit of discussions presented later in this chapter, these effects are very briefly reviewed here.

## Isotope shift

The isotope shift (IS) observed in atomic spectra is the sum of field shift (FS) or volume shift and mass shift (MS).

$$IS = FS + MS \tag{9}$$

**Field shift** The FS is due to changes in the electronic charge density at the nucleus and the mean square charge radius between two isotopes. The FS between two isotopes with mass $A_i$ and $A_j$ (where $j = i+1$) in electronic transition $t$ is given by

$$\delta \nu_t^{A_i A_j} \text{ (field shift)} = F_t \, C^{A_i A_j} \tag{10}$$

$F_t$ depends only on electronic properties and can be presented as a product of electronic factor $E_t$ and correction factor $f(Z)$.

$$F_t = E_t \; f(Z) \tag{11}$$

Electronic factor $E_t$ is proportional to $\Delta|\psi(0)|^2_t$ , the change of the total non-relativistic electron density at a point nucleus, and

$$E_t = ( \Pi a_0^3 / Z ) \Delta|\psi(0)|^2_t \tag{12}$$

where $a_0$ is the Bohr radius and Z is the nuclear charge. The function f(Z) includes corrections to $E_t$ due to relativistic effects and finite nuclear charge distribution. It is related to the theoretical isotope shift constant for a uniformly charged nuclear sphere, $K^{A_iA_j}_{unif}$ as

$$f(Z) = K^{A_iA_j}_{unif} [ R_{eq} / R_0 A^{-1/3} ]^{2\sigma-2}$$

$$[ (5/2) A^{-1/3} / r_0^2 (A_j - A_i) ] \tag{13}$$

$$\text{where } R_{eq}^2 = (5/3) < r^2 > \tag{14}$$

$$A = (A_i + A_j) / 2 \tag{15}$$

$$\sigma = (1 - \alpha^2 Z^2 )^{1/2} \tag{16}$$

and $< r^2 >$ is the mean square radius of the proton distribution.

The factor $C^{A_iA_j}$ characterizes the changes in the radial nuclear charge distribution between the isotopes.

$$C^{A_iA_j} = \delta\langle r^2\rangle^{A_iA_j} - (K_2/K_1)\,\delta\langle r^4\rangle^{A_iA_j} - (K_3/K_1)\,\delta\langle r^6\rangle^{A_iA_j} - \;.....\qquad (17)$$

Seltzer (110) calculated the $K_n$ values for 1s levels using self-consistent-field (SCF) solutions of the Dirac equation, and the result of $K_n/K_1$ values indicated that the contributions of the higher charge moments are negligible, and the electron wavefunction is nearly constant over the nuclear volume. Thus it is approximated that $C^{A_iA_j}$ is proportional to the change of a single moment $\delta\langle r^{2\sigma}\rangle$

$$C^{A_iA_j} \simeq \delta\langle r^{2\sigma}\rangle \qquad (18)$$

For light elements $\sigma = (1-\alpha^2 Z^2)^{1/2}$ approaches 1 and the field shift becomes proportional to the change in mean square radius between the isotopes.

Mass shift Neglecting spin-orbit coupling, Hughes and Eckart (111) suggested that the MS can be presented as the sum of normal mass shift (NMS) and specific mass shift (SMS).

$$MS = NMS + SMS \qquad (19)$$

$$\delta\nu_t^{A_i A_j} \text{(mass shift)} = [(A_j - A_i)/A_i A_j][M_t\text{(normal)} + M_t\text{(specific)}] \qquad (20)$$

The NMS is the reduced mass correction and calculated from

$$M_t\text{(normal)} = \nu_t / 1836.1 \qquad (21)$$

where $\nu_t$ is the frequency of the transition in $cm^{-1}$.

The specific mass shift is due to the effect of electron-electron correlation on the recoil kinetic energy of the nucleus. It depends on the number of atomic electrons and inversely proportional to the square of the nuclear mass. The absolute value of $M_t$(specific) could be many times larger than $M_t$(normal) and hence not negligible. Unfortunately, the calculation of the SMS have been less successful and caused difficulties for extraction of field shift from the experimentally observed isotope shift.

Among all kinds of shifts mentioned above, only the NMS is always positive (i.e. the heavier isotope shifted toward higher frequency). The SMS could shift to higher or lower frequency, depending on both nuclear and atomic factors. The field shift (FS) could also have positive or negative shift depending on whether the upper or lower level has the larger electronic charge density at the nucleus.

More detailed discussions of theoretical outline and experimental observation of optical isotope-shift parameters can be found in some review papers (82, 100, 112, 113).

## Hyperfine splitting

While isotope shifts reveal characteristics of changes in the radial nuclear charge distribution between isotopes, hyperfine structure yields accurate information on nuclear magnetic dipole moments and electric quadrupole moments. Spectral splitting of a single isotope into two or more hyperfine components is due to the interaction of the nuclear magnetic moment with electronic magnetic field. The number of hyperfine splittings F depends on the nuclear angular momentum of the isotope I, and the electronic angular momentum J.

$$F = (I+J),\ (I+J)-1,\ (I+J)-2,\ \ldots\ldots\ldots\ (I-J) \qquad (22)$$

For the Cu I 578.2 nm ( $^2D_{3/2}$ - $^2P_{1/2}$ ) transition, $J'=3/2$ and $J=1/2$, and both Cu-63 and Cu-65 has $I=3/2$. Therefore, for each isotope, there are two hyperfine splittings $F = 2, 1$ at the upper level and four hyperfine splittings $F'= 3, 2, 1, 0$ at the lower level. The selection rule, $\Delta F= \pm 1, 0$, allows six hyperfine transitions $K_{F'F}$ as shown in Figure 2. Consequently, each Cu-63 and Cu-65 isotope has a set of six hyperfine components, and thus resulting in a 12-component hyperfine structure.

## Hyperfine component strengths

In order to simulate theoretical hyperfine structure for isotope ratio analysis, one must first determine the strengths of all hyperfine components. Relative hyperfine component strengths of a set of hyperfine lines are well defined, and can be calculated based on their direct relation to the excitation or emission rate. Excitation rate is directly proportional to $\xi^2$ , where $\xi$ can be defined by the equation

$$\xi = \langle \alpha JIFM_F | \hat{\varepsilon} \cdot \bar{F} | \alpha' J' IF' M_{F'} \rangle \tag{23}$$

for weak fields, assuming that no optical, fine structure or hyperfine structure pumping effects exist. $\alpha$ , J, F and $M_F$

are parameters for the upper level and $\alpha'$, J', F' and $M_{F'}$ are parameters for the lower level of the atomic transition. $\hat{\varepsilon}$ is the polarization vector and $\bar{r}$ is the position vector. For linear polarization along the z axis,

$$\xi = \left\langle \alpha JIFM_F \middle| z \middle| \alpha' J' IF' M_F \right\rangle \tag{24}$$

$$= \left\langle \alpha JIFM_F \middle| (4\pi/3)^{1/2}\, r\, T_q^{(K)} \middle| \alpha' J' IF' M_{F'} \right\rangle \tag{25}$$

where $T_q^{(K)}$ is a spherical tensor of rank k in J space with k=1 and q=0. Thus,

$$\xi_{[F'M_{F'},FM_F]} = \left\langle \alpha JIFM_F \middle| (4\pi/3)^{1/2}\, r\, T_0^{(1)} \middle| \alpha' J' IF' M_{F'} \right\rangle \tag{26}$$

The Wigner-Eckart theorem (114) is then used to remove the dependence of matrix elements of $T_0^{(1)}$ on the magnetic quantum numbers $M_F$ and $M_{F'}$. The result is

$$\xi = (-1)^{F-M_F} \begin{pmatrix} F & 1 & F' \\ -M_F & 0 & M_{F'} \end{pmatrix} \left\langle \alpha JIF \middle\| (4\pi/3)^{1/2}\, r\, T^{(1)} \middle\| \alpha' J' IF' \right\rangle \tag{27}$$

where $\begin{pmatrix} F & 1 & F' \\ -M_F & 0 & M_{F'} \end{pmatrix}$ is a 3j symbol and

$\left\langle \alpha JIF \middle\| (4\pi/3)^{1/2}\, r\, T^{(1)} \middle\| \alpha' J' IF' \right\rangle$ is a reduced matrix element and is independent of $M_F$, $M_{F'}$ and q .

Now, $rT^{(1)}$ operates only in the J space, and nuclear coordinate is no longer involved. The reduced matrix element can be defined (114) by the equation

$$\langle \alpha JIF \| r\, T^{(1)} \| \alpha' J' I F' \rangle =$$

$$(-1)^{J+I+F'+1}[(2F+1)(2F'+1)]^{1/2} \begin{Bmatrix} F & 1 & F' \\ J' & I & J \end{Bmatrix} \langle \alpha J \| rT^{(1)} \| \alpha' J' \rangle \tag{28}$$

where $\begin{Bmatrix} F & 1 & F' \\ J' & I & J \end{Bmatrix}$ is a 6j symbol. By combining equation 28, 27 and 23, it is apparent that the excitation rate $\xi^2$ is directly proportional to the transition strength K and

$$K_{[F'M_{F'} \rightarrow FM_F]} = \begin{pmatrix} F & 1 & F' \\ -M_F & 0 & M_{F'} \end{pmatrix}^2 (2F+1)(2F'+1) \begin{Bmatrix} F & 1 & F' \\ J' & I & J \end{Bmatrix} \tag{29}$$

To find the total strength $K_{[F'-F]}$, equation 29 must be summed over all $M_F$ and then over all $M_{F'}$. For $M_F = M_{F'}$,

$$K_{[F'-F]} = \sum_{\substack{M_F \\ M_{F'}}} K_{[F'M_{F'} - FM_F]} \tag{30}$$

$$= (2F+1)(2F'+1) \begin{Bmatrix} F & 1 & F' \\ J' & I & J \end{Bmatrix}^2 \sum_{\substack{M_F \\ M_{F'}}} \begin{pmatrix} F & 1 & F' \\ -M_F & 0 & M_{F'} \end{pmatrix}^2 \tag{31}$$

Since the last term in equation 31 becomes unity (114), the final expression for the relative hyperfine component strength is

$$K_{F',F} = (2F+1)(2F'+1)\begin{Bmatrix} F & 1 & F' \\ J' & I & J \end{Bmatrix}^2 \qquad (32)$$

Similarly, one can calculate the decay rate or spontaneous emission rate, $\left|\langle \alpha' J' I F' M_{F'} \right| \bar{r} \left| \alpha J I F M_F \rangle\right|^2$ using

$$\bar{r} = (4\pi/3)^{1/2} \sum_{q=-1}^{1} (-1)^q \; \hat{\varepsilon}_{-q} \; T_q^{(-1)} \qquad (33)$$

and derive the intensity in spontaneous emission for thermally populated distribution as

$$I_{F\rightarrow F'} = (2F'+1)(2F+1)\begin{Bmatrix} F' & 1 & F \\ J & I & J' \end{Bmatrix}^2 \qquad (34)$$

Equation 34 is the same as equation 32, since the two 6j symbols $\begin{Bmatrix} F' & 1 & F \\ J & I & J' \end{Bmatrix}$ and $\begin{Bmatrix} F & 1 & F' \\ J' & I & J \end{Bmatrix}$ are identical. Thus, the hyperfine component strengths determined from both excitation and emission rates yield the identical results.

Using equation 32 or 34, the six hyperfine component strengths $K_{32}$, $K_{21}$, $K_{22}$, $K_{11}$, $K_{12}$ and $K_{01}$ of the Cu I 578.2 nm line, as shown in Figure 2, are calculated and the results agree with the experimentally measured strengths.

## Simulation of Doppler-broadened hyperfine profile

The natural linewidth of an atomic line is broadened by two major effects, the Doppler and Lorentzian broadening. The Doppler broadening is the frequency variations due to the thermal motion of the atoms. For a given atomic line, the Doppler full width at half maximum (FWHM) depends only on the translational temperature and can be defined by the expression

$$\Delta v_D = 7.162 \times 10^{-7}\, v_0\, (T/A)^{1/2} \qquad (35)$$

where $v_0$ is the center frequency, $\Delta v_D$ is the Doppler FWHM, T is the absolute temperature and A the atomic weight. The Lorentzian broadening is due to the collision of radiating particles with one another and the consequent interruption of absorption or emission of radiation. Since the frequency of collisions is directly proportional to the density, the

Figure 2. Hyperfine transitions of copper-63 or copper-65 isotope for the Cu I 5782 Å line

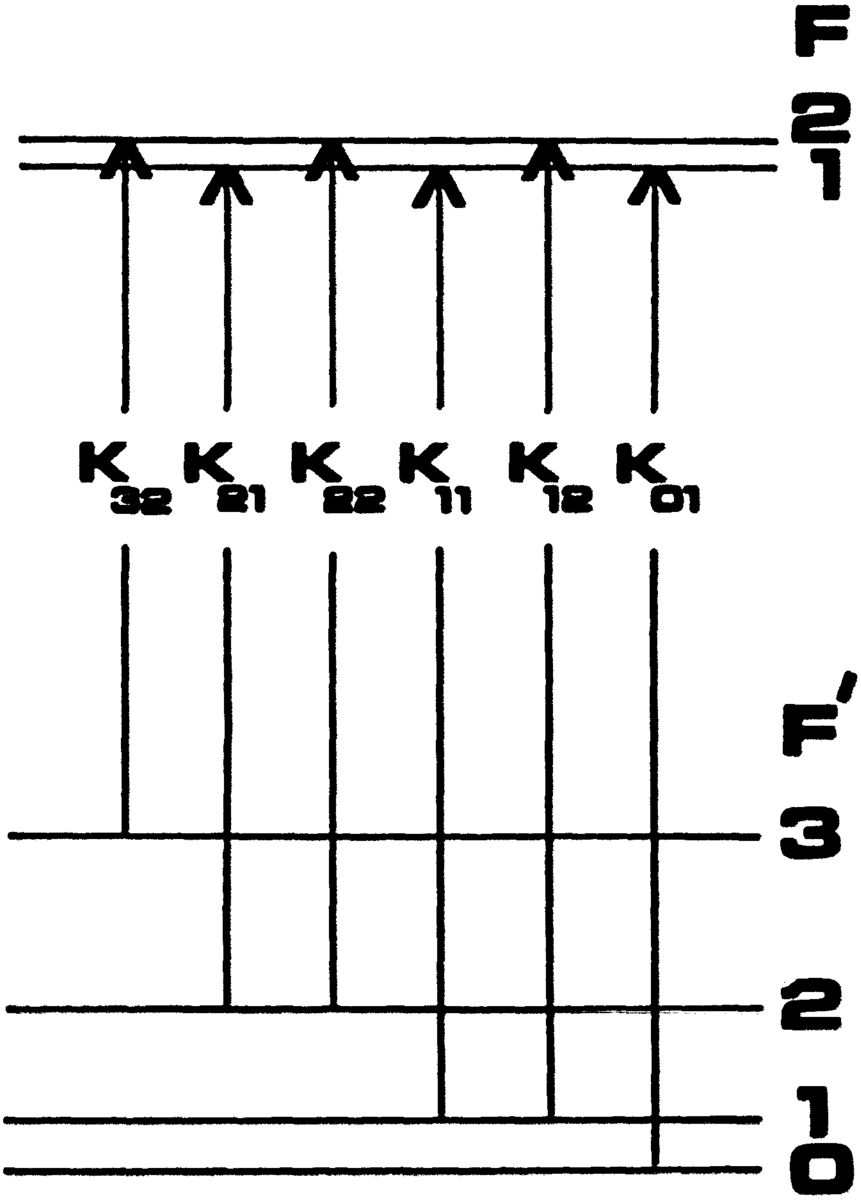
F
2
1
$K_{32}$
$K_{21}$
$K_{22}$
$K_{11}$
$K_{12}$
$K_{01}$
F'
3
2
1
0

Lorentzian linewidth (FWHM) is proportional to the density or pressure. The normal operating gas pressure inside a hollow-cathode lamp is only 2 - 5 torr, and thus the Lorentzian broadening is very small and negligible compared to the Doppler broadening. Therefore, simulation of actual absorption profiles can be done reliably by considering the Doppler broadening alone.

A Doppler-broadened hyperfine profile can be computed point by point as a function of frequency using the following Gaussian frequency distribution equation

$$K_V = K_0 \exp\left[(-Ac^2/2R_gT)\left\{(V-V_0)/V_0\right\}^2\right] \qquad (36)$$

where $K_0$ is the relative peak intensity at central frequency, A is the mass of atom (or isotope), c is the speed of light, $R_g$ is the gas constant and T the temperature. For the Cu I 578.2 nm transition, there are 12 hyperfine components, and the simulated atomic hyperfine profile can be computed by summing over the 12 individual Doppler-broadened contributions. Therefore,

$$K_V = \sum_{n=1}^{m} K_{0,n} \exp\left[(-A_nc^2/2R_gT)\left\{(V-V_{0,n})/V_{0,n}\right\}^2\right] \qquad (37)$$

Here m is the total number of hyperfine components.

To simulate the actual absorption profiles using equation 37, one must next find $V_{0,n}$ values, the magnitudes of the hyperfine shifts. For the Cu I 578.2 nm transition, there are 12 hyperfine-component central frequencies and the hyperfine shift values $\Delta_n$ ( i.e. $V_{0,n+1} - V_{0,1}$ ) have been reported by other workers using various types of high resolution measurement methods (115 - 118). However, these values vary slightly, depending on the measurement method, the electric field and the geometry and dimension of the discharge electrodes used. Since it is essential to obtain these values with high accuracy (within $\pm 0.0005$ $cm^{-1}$) for the isotope ratio calculations, one must determine them for the specific type of discharge plasma used. This is accomplished by least-squares fitting of experimental hyperfine profiles collected from a sample with known isotope abundances while varying each $V_{0,n}$ by 0.001 $cm^{-1}$ at a time until a set of $V_{0,n}$ which yields the best matching theoretical profile is obtained.

Once all the $K_{0,n=1,12}$ values (the relative hyperfine-component strengths) and $V_{0,n=1,12}$ values (the hyperfine-component frequencies) have been determined, one can simulate theoretical hyperfine profiles for various combinations of isotope ratio R, and plasma temperature T using equation 37. R is the ratio of isotope abundances of copper-63 and copper-65 isotopes. It is used to adjust the relative absorption strengths of the two isotopes, $K_{0,n}$ (Cu-63) and $K_{0,n}$ (Cu-65). Figure 3 shows the two 6-component sets of hyperfine structure simulated for Cu-63 and Cu-65, using the natural-abundance ratio Cu-63/Cu-65 of 2.235, and plasma temperature of 1400 °K for the upper trance and the 20 °K for the lower traces. Six hyperfine components for each Cu-63 and Cu-65 isotopes are displayed with dashed line and solid line respectively. The upper trace is simulated to match an actual experimental absorption profile collected by optogalvanic detection using a hollow-cathode discharge. The isotope ratio of an unknown analyte sample can be calculated by matching the experimental hyperfine profile to these theoretical profiles and picking the set which yields the least sum of squares of the deviations (SSD).

The extraction of isotope ratio information from the atomic hyperfine structure data, and the application of this technique to real samples, using a specially constructed demountable hollow cathode discharge, will be discussed in the following chapter.

Figure 3. Doppler-broadened atomic hyperfine structure of Cu I 5782 Å transition. Simulated for 1400 K ( Top ) and 20 K ( Bottom ) with hyperfine components of Cu-63 and Cu-65 shown as dashed lines and solid lines respectively

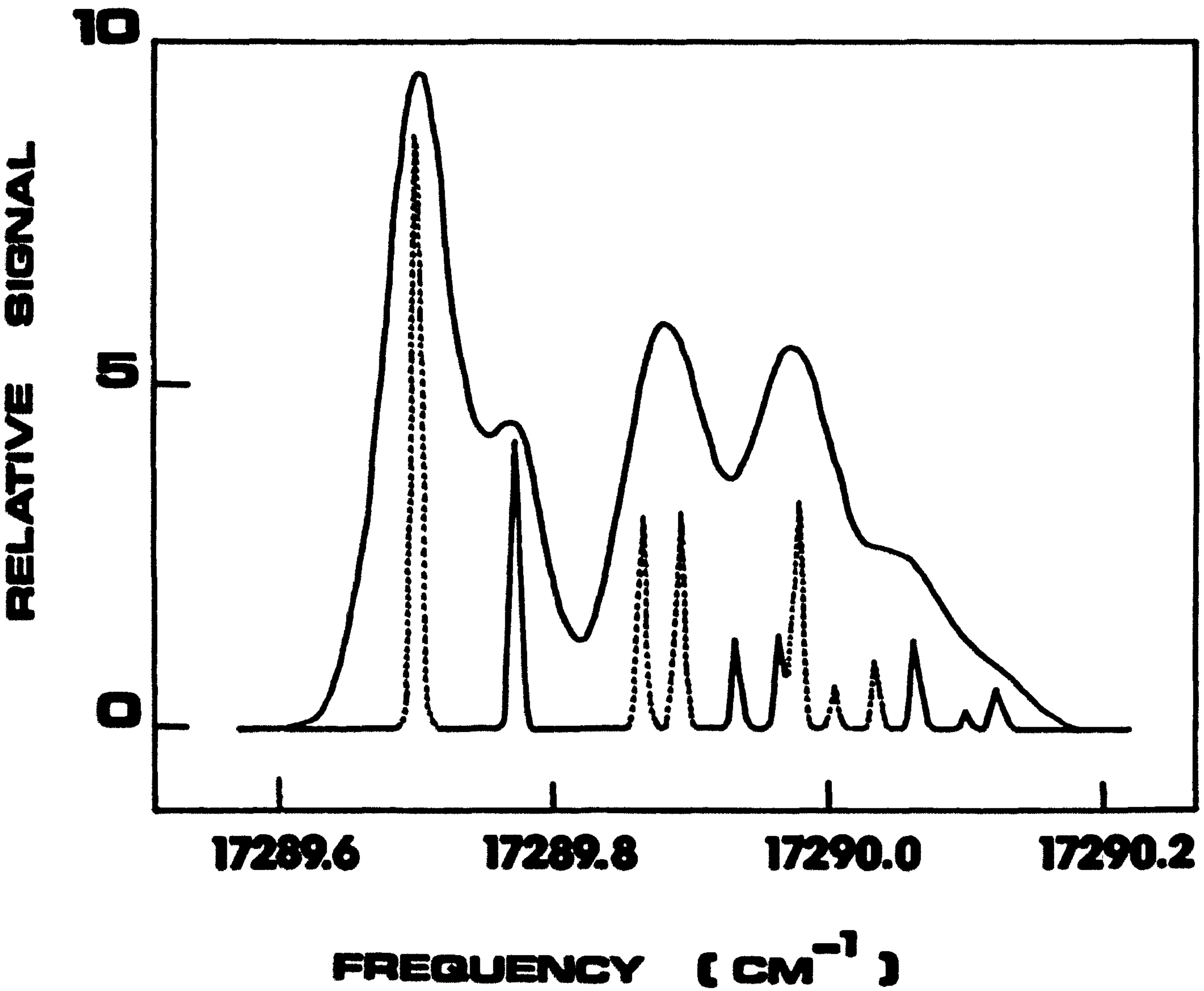
10
5
0
RELATIVE SIGNAL
17289.6
17289.8
17290.0
17290.2
FREQUENCY ( CM$^{-1}$ )

# CHAPTER III. STABLE ISOTOPE RATIO ANALYSIS BASED ON ATOMIC HYPERFINE STRUCTURE AND OPTOGALVANIC SPECTROSCOPY

## Review

Reliable and safe application of isotopes as analytical tracers is highly essential in many areas, including biomedical, environmental and geochronological sciences. Because of their unique properties, both radioactive and non-radioactive isotopes have been readily employed in various tracer techniques in these fields. It is well-known that the presence of trace levels of both essential and non-essential elements can vitally affect biological processes. Various diseases have been diagnosed as the direct results of toxic effects of some trace elements, deficiencies of certain trace elements or genetically defective mineral metabolism (119). It is important to investigate how and where mineral elements are absorbed, allocated and accumulated in various parts of the body. Chemical balance studies and administration of radioactive tracers have been the most frequently used techniques for these studies. Many disadvantages of the balance method include: the inability to differentiate the unabsorbed dietary losses and the endogenous loss, the requirement of several weeks of time to establish equilibrium in the level of intake, and the tedious laboratory determinations of intake and output. Techniques employing radioactive isotopes yield faster and more accurate results compared to the balance method. Scheinberg et al. (120) and Neumann et al. (121) employed the radioactive copper-64 isotope to study the metabolic pathways of red blood cell copper in Wilson's disease, the progressive fatal copper toxicity caused by the defect in the regulation of copper metabolism. Wrenn et al. used the radioactive thorium-229 isotope as tracer for the analysis of human tissues (122).

Some radioactive isotopes have also been used for sample analysis in environmental and geochronological sciences. Radioisotope Pb-212 was used as yield tracer for determination of lead concentration and distribution in sea water (123). Pb-210 in surface soil sample was measured by using Gamma spectrometry (124). However, the application of these radioisotopes in humans and other radiation-sensitive subjects is severely limited because of their hazardous nature.

Measurements of abundances of stable isotopes have been reported using various techniques, such as neutron activation analysis (125 - 127) and a variety of mass spectrometric methods, including GC-MS (128, 129), thermal ionization MS (130), field ionization MS (131), ICP-MS (132, 133), fast atom bombardment MS (135) and spark source MS (136, 137). Some of these techniques require extensive sample preparation such as separation and chelation of analyte metal. The major disadvantage of all mass spectrometric methods is the interference caused by other ions having exactly the same m/e value as the analyte. The resolving power of most commercial mass spectrometers is not sufficient to avoid interference caused by some ions (134), and the overall sensitivity decreases if higher resolving powers are used.

In this chapter, we present a new approach to stable isotope ratio analysis based on atomic hyperfine structure available from the optical absorption profile. This analytical spectroscopic scheme is virtually interference-free because of the highly selective and specific nature of atomic hyperfine structures. Each atomic hyperfine structure is a spectroscopic "fingerprint" of an atomic species and has its own unique shape and profile within a range of frequency equal to or narrower than 15 GHz or 0.5 $cm^{-1}$. It is virtually impossible to have a hyperfine structure of another element with identical lineshape at the same frequency. Thus one could study a minor constituent in a complex matrix without extensive sample preparation.

A single-frequency tunable continuous-wave ring dye laser is used as the optical excitation source. Samples are electrodeposited on the cathode of a specially designed and constructed demountable hollow-cathode lamp which serves both as the atomizer and detector. Doppler-broadened hyperfine profiles are collected by monitoring the optogalvanic signal generated between the two electrodes of the discharge when the laser frequency is scanned across the optical transition. All hyperfine components that are convoluted under the Doppler-limited spectrum can be recovered by matching the experimental and theoretical hyperfine profiles using a least-squares criterion, and the relative isotopic abundances of all isotopes present can be determined with good accuracy and precision. This scheme will be demonstrated for the analysis of Cu-63 and Cu-65 isotopes using the hyperfine structure of the Cu I 578.2 nm, $^2D_{3/2}$ - $^2P_{1/2}$ transition.

## Experimental

A schematic diagram of the experimental setup for optogalvanic measurement of atomic hyperfine structure is shown in Figure 4. A Control argon ion laser Model 554A (Orlando, FL) operating at 3.3 W all-line output is used to pump a Spectra-Physics Model 380A single-frequency cw ring dye laser (Mountain View, CA). The ring dye laser is passively stabilized to provide tunable single-frequency radiation (40 MHz jitter, peak-to-peak) which can be electronically scanned over 30 GHz with selectable starting frequency and scanning rate. Rhodamine 590 dye (Exciton Chemical Co., Dayton, OH) is used in the ring dye laser to obtain about 250 mW of stable single-frequency output power using 3.3 W of pump power. A small fraction of the dye laser beam is sent to a Burleigh Instruments Model WA-20 wavemeter (Fishers, NY) for laser frequency calibration. The I/O port of the wavemeter is interfaced to a Digital Equipment Corp. PDP 11/10 minicomputer (Maynard, MA) to collect and store the frequency values. Since the wavemeter measures the laser frequency in vacuum, all frequency values collected in the computer are the vacuum frequency values and accurate to 0.01 $cm^{-1}$. A Rofin Model 7510 mechanical chopper (Newton Upper Falls, MA) is used to modulate the

Figure 4. Block diagram of the experimental arrangement for optogalvanic measurement of atomic hyperfine structure. Optical paths are shown as dashed lines and electrical connections are shown as solid lines

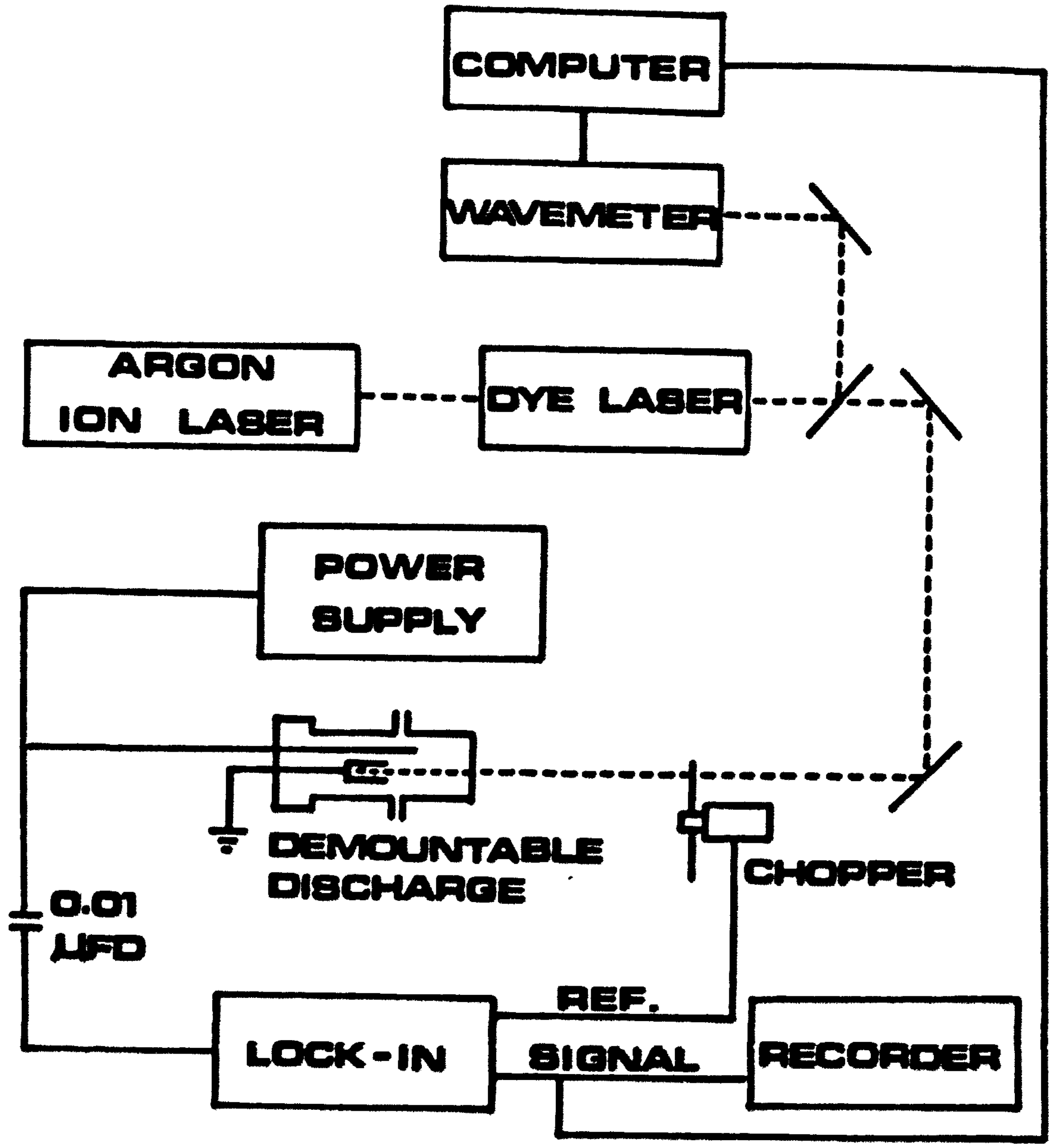
COMPUTER
WAVEMETER
ARGON ION LASER
DYE LASER
POWER SUPPLY
DEMOUNTABLE DISCHARGE
CHOPPER
0.01 µFD
REF.
SIGNAL
LOCK-IN
RECORDER

laser beam at 1 KHz modulation frequency. The dye laser beam is directed into the cathode cavity of the home-made demountable hollow-cathode discharge operated by a constant-current power supply. The resulting optogalvanic signal is sent to a Princeton Applied Research Model HR-8 lock-in amplifier (Princeton, NJ) where a 1-sec time constant is used. The output of the lock-in amplifier is connected to a Keithley Model 160B digital voltmeter (Cleveland, OH), and the analog output of the voltmeter is digitized via one of the ADC channels of the Laboratory Peripheral System (LPS-11) of the minicomputer. The computer takes simultaneous readings of both optogalvanic signal from the lock-in amplifier and the laser frequency from the wavemeter every 0.5 sec, and the real-time spectrum is displayed on a Visual Technology Inc. Model 550 graphics video terminal (Tewksbury, MA). The real-time spectrum monitoring is useful in detecting any experimental defects such as laser mode-hopping, while the experiment is in progress. All experimental hyperfine profiles are collected using the scan range of 27 GHz ( 0.9 $cm^{-1}$ ) and the scan time of 100 sec.

## Demountable hollow-cathode lamp (DHCL) as atomizer-detector

Because of its ability to provide an intense source of narrow lines for most elements, the hollow-cathode lamp has been most commonly used in atomic absorption spectroscopy. Several types of demountable hollow cathode lamps (DHCL) with interchangable cathodes have been reported to yield satisfactory results and some of these economically more efficient lamps are available commercially (138 - 145). However, DHCLs currently available utilize a rather large piece of analyte metal as cathode material, and therefore it is impossible to use them as both atomizer and detector for trace concentration analysis. In our research work, the DHCL not only serves as an atomizer and sample holder but also as a detector for optogalvanic signal. For trace concentration analysis, it requires that the lamp's demountable "host" cathode be able to hold a small amount (a few microgram) of analyte material and still provides the advantages of a sealed hollow-cathode lamp such as rapid warm-up, narrow linewidth, high sputtering of analyte material, stability, long lifetime and ease of operation. A DHCL which has all these qualities was specially designed and constructed using materials available at the Ames Laboratory storerooms.

Figure 5. Demountable hollow-cathode atomizer-detector

(A) Nylon bolt for securing vacuum for cathode rod
(B) Nylon vacuum flange
(C) 2-in long 1/4-in-20 bolts
(D) Stainless-steel vacuum flange
(E) O-rings
(F) O-rings
(G) Screw-mount cathode assembly (See Figure 6 for close-up)
(H) Quartz window
(I) Tungsten anode
(J) Pyrex-to-Kovar joint
(K) Nylon bolt for securing vacuum for anode rod

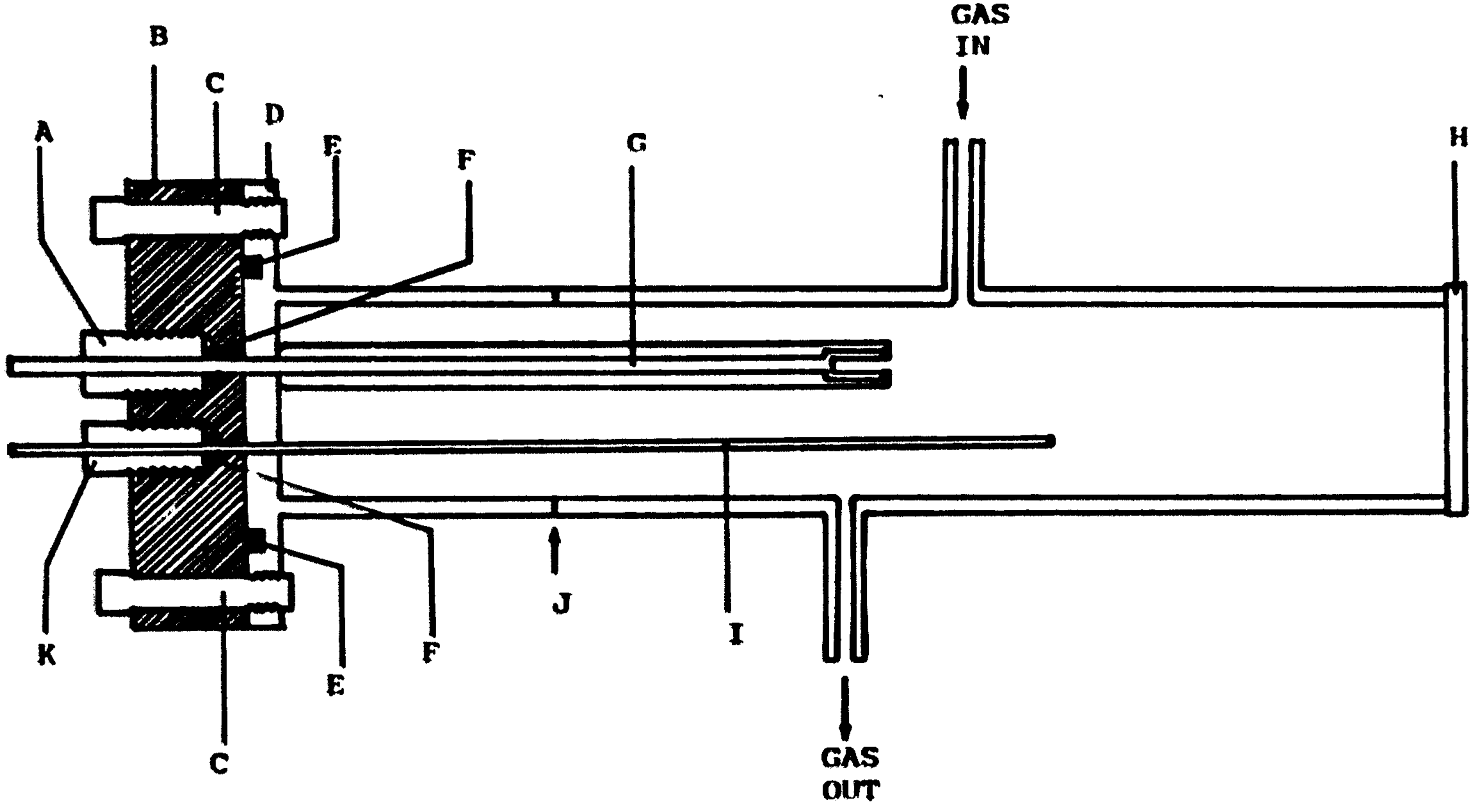
B
C
D
A
E
F
G
GAS IN
H
K
C
E
F
J
I
GAS OUT

Figure 6. Close-up of demountable hollow-cathode assembly

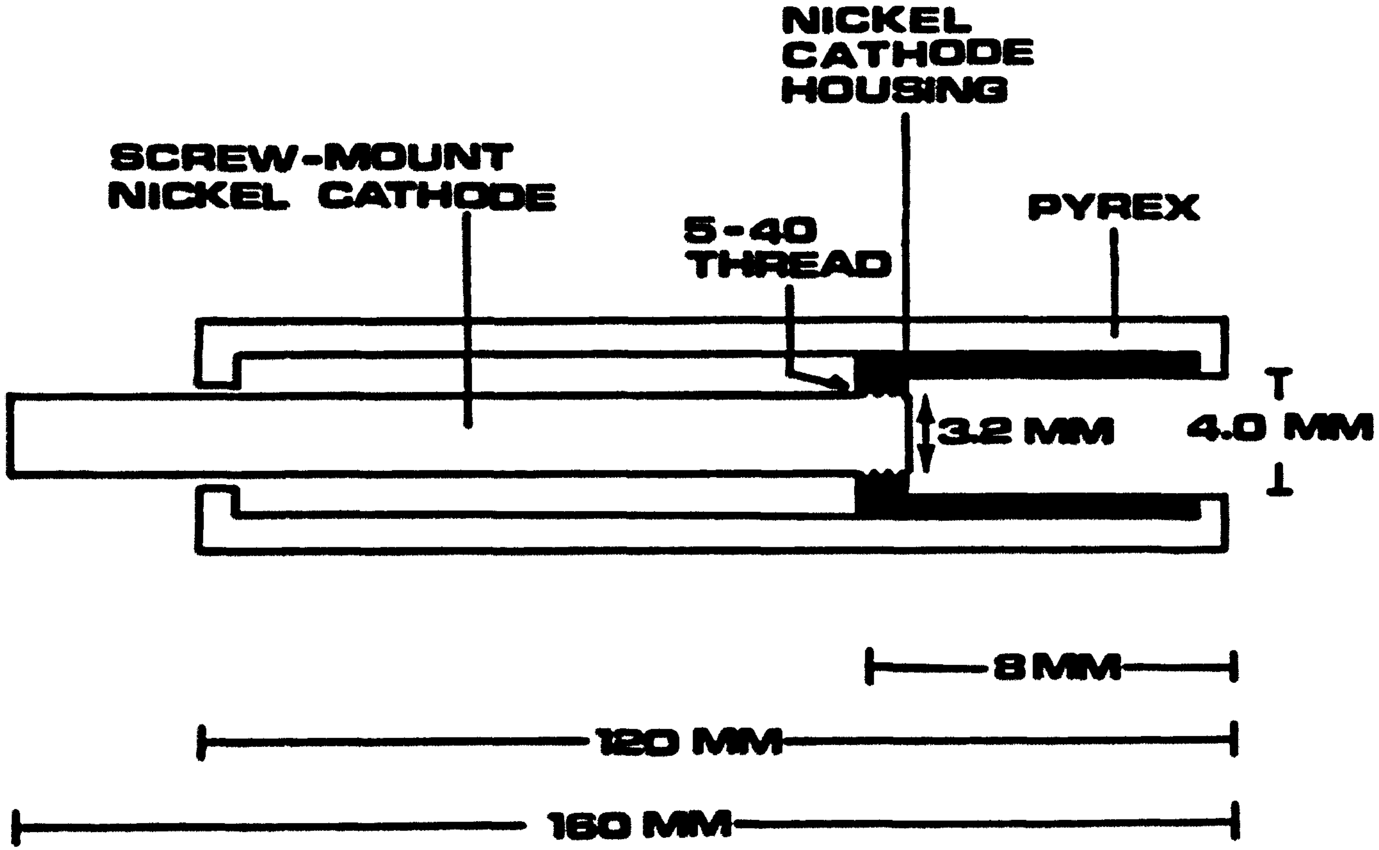
NICKEL CATHODE HOUSING
SCREW-MOUNT NICKEL CATHODE
PYREX
5-40 THREAD
3.2 MM
4.0 MM
8 MM
120 MM
160 MM

## DHCL design

As shown in Figure 5, the DHCL is constructed using a 1.5-in outside diameter (o.d.) 6-in. long Pyrex-to-Kovar joint. A quartz window is attached on the Pyrex end of the joint using Armstrong A-12 adhesive (Armstrong Products Co., Warsaw, IN). A 3-in diameter stainless-steel vacuum flange is welded on the Kovar end of the joint. A 3-in diameter, 3/4-in thick nylon flange, mounted with cathode and anode, serves as a two-conductor electrical vacuum feedthrough. A 1-7/8 in o.d., 1/8-in wall O-ring and six 2-in long 1/4-in-20 bolts are used to secure the vacuum between the nylon flange and the stainless-steel flange. The cathode and anode are mounted on the nylon flange through the central axis of 3/8-in o.d. and 1/2-in o.d. nylon bolts respectively. The nylon bolts are screwed onto the nylon flange through O-rings to achieve vacuum seal.

Figure 6 shows the close-up of the demountable hollow-cathode assembly. A 1/8-in diameter nickel rod (or copper rod) serving as the cathode is screw-mounted in a 4-mm inner diameter, 8-mm long nickel cathode housing through 5-40 thread. (The high-purity nickel used for cathode housing, containing less than 0.9 ppm copper, was obtained locally from the Ames Laboratory.) Pyrex tubing is sealed on the cathode assembly to insulate the outer surfaces of cathode rod and cathode housing from the electric field, and thus confining the cathode sputtering inside the cathode cavity. A 1/16-in diameter, 7-in long tungsten welding rod (Welders Engineering Research Co., Charlotte, NC, Cleaned Finish) is used as the anode. The gap between the cathode and the anode is 9 mm. The anode rod is approximately 1-in longer than the cathode assembly so that the sharp edge of the tip of the anode is facing away from the cathode cavity. This reduces the chance of electrical arcing between the electrodes, especially at higher lamp current (more than 60 mA), and gas pressure (more than 10 torr). The analyte, at trace level, is electrodeposited onto the small 1/8-in diameter end surface of the tip of the cathode rod.

### DHCL vacuum system

To avoid copper contamination, no brass tubing or valve is used throughout the vacuum line. Stainless-steel Cajon Ultra-torr fittings (Macedonia, OH) provide vacuum-tight seal with reusable, quick, finger-tight connections between the glass inlet and outlet of the lamp and the vacuum system. Matheson research grade (99.9999%) neon gas (East Rutherford, NJ) is used as the buffer gas, and the gas pressure is monitored by a MKS Instruments Model 221A capacitance manometer (Burlington, MA) which has a 0 - 10 torr full scale pressure range. Both static and flowing gas modes provide satisfactory lamp stability and performance. In flowing gas mode, fresh neon gas is continuously delivered to the lamp and thus providing virtually an unlimited lamp lifetime with high stability. Static mode, with sealed-off neon discharge gas inside the lamp, provides equally good lamp stability, and therefore most frequently used for all data collections. A 1/3 HP mechanical vacuum pump (General Electric, Fort Wayne, IN) is used for the vacuum system.

The DHCL can be disassembled and assembled, and the electrodes replaced, within a few seconds. While disconnecting the lamp from the vacuum system or breaking the vacuum, the mechanical pump is always left on to assure that no oil vapor from the pump is sucked into the lamp. The DHCL must be maintained hydrocarbon-free as much as possible to achieve good stability. After the vacuum has been broken and the electrodes exposed to the atmosphere, a baking period of 10 minutes is sufficient to restore a noise-free discharge baseline. Baking is done by simply firing the lamp at normal operating current (30 mA) and then flushing with the discharge gas. A reasonably stable galvanic baseline can be obtained even without any baking, each time the lamp is reassembled after exposure to the atmosphere. The lamp intensity and optogalvanic signal generated by this DHCL are comparable to or better than those of a commercial hollow-cathode lamp (Perkin-Elmer Corp., Norwalk, CT) at similar lamp current.

### Electrodeposition of sample on cathode

Analyte is introduced into the DHCL atomizer-detector by depositing the material on the tip of the cathode rod. A simple operational circuit as shown in Figure 7 is constructed to perform controlled-potential electrodeposition using the cathode rod as the working electrode, a platinum wire as the counter electrode and a saturated-calomel electrode as the reference electrode. For the electrodeposition of copper, a controlled-potential of -0.35 V vs. SCE is applied to the cathode rod. All the cathode rod surface that is submerged in the solution, except the flat tip surface area, is insulated by Teflon tape so that the electrodeposition is concentrated on the small area (0.013 sq. in.) of the cathode tip. It is important, especially at trace level analysis, that all deposited material is concentrated on the flat tip and not in the screw threads of the cathode rod, since only the flat tip area of the cathode rod is exposed to the discharge sputtering inside the cathode cavity. All electrodepositions are done at pH 2 with potassium nitrate as supporting electrolyte. After deposition, the Teflon

**Figure 7.** **Operational circuit for controlled-potential electrodeposition**

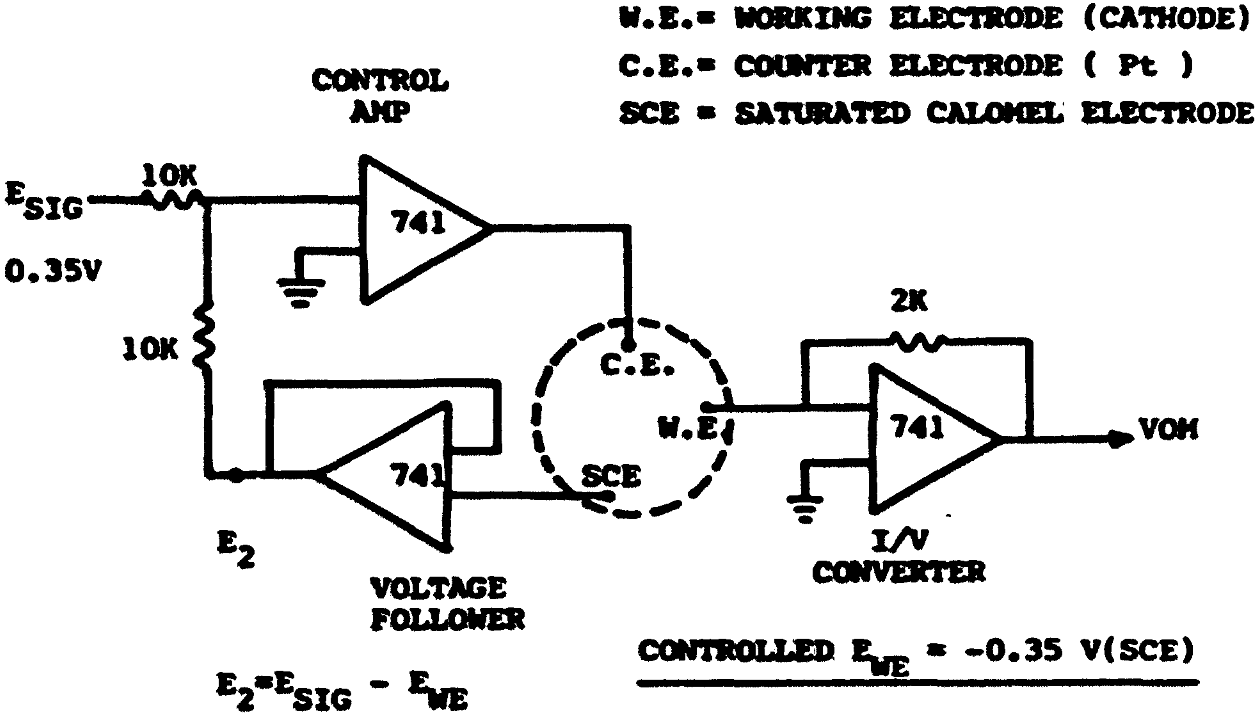
W.E.= WORKING ELECTRODE (CATHODE)
C.E.= COUNTER ELECTRODE ( Pt )
SCE = SATURATED CALOMEL ELECTRODE
CONTROL AMP
$E_{SIG}$
0.35V
10K
10K
741
741
741
2K
C.E.
W.E.
SCE
VOM
$E_2$
VOLTAGE FOLLOWER
I/V CONVERTER
$E_2 = E_{SIG} - E_{WE}$
CONTROLLED $E_{WE}$ = -0.35 V(SCE)

tape is removed and the cathode rod is rinsed with triply-distilled deionized water and air dried before installation in the cathode housing. Before sealing the lamp, final cleansing is done by wiping the Pyrex tubing of the cathode assembly, the anode and the interior surface of the nylon flange with methanol to remove any fingerprints or trace organic contaminants.

All copper stock solutions were prepared using triply-distilled deionized water, stored in polyethylene bottles and used the same day as prepared. Enriched isotopes Cu-63 (99.89 %) and Cu-65 (99.69 %) were purchased from the Oak Ridge National Laboratory and stock solutions were prepared by dissolving the isotopes in 10% nitric acid (containing less than 0.05 ppm copper). Natural-abundance copper stock solutions were prepared by dissolving electrolytic copper metal powder (Fisher Scientific Co., Fairlawn, NJ, Electrolytic Purified) in 2% nitric acid.

## Digestion of human whole blood sample

In order to extract trace amount of copper from the human whole blood sample, first it is necessary to digest it. A miniaturized Bethge digestion apparatus (146), as shown in Figure 8, was used for wet ashing of blood samples under total reflux and the unique control of the oxidizing

Figure 8. Miniaturized Bethge digestion apparatus

(A) Water-cooled reflux condenser
(B) Cooling-water inlet and outlet
(C) Reflux collector
(D) Three-way stopcock
(E) Water-distillate outlet
(F) 50-ml round-bottom digestion bottle
(G) Hemispherical heating mantle

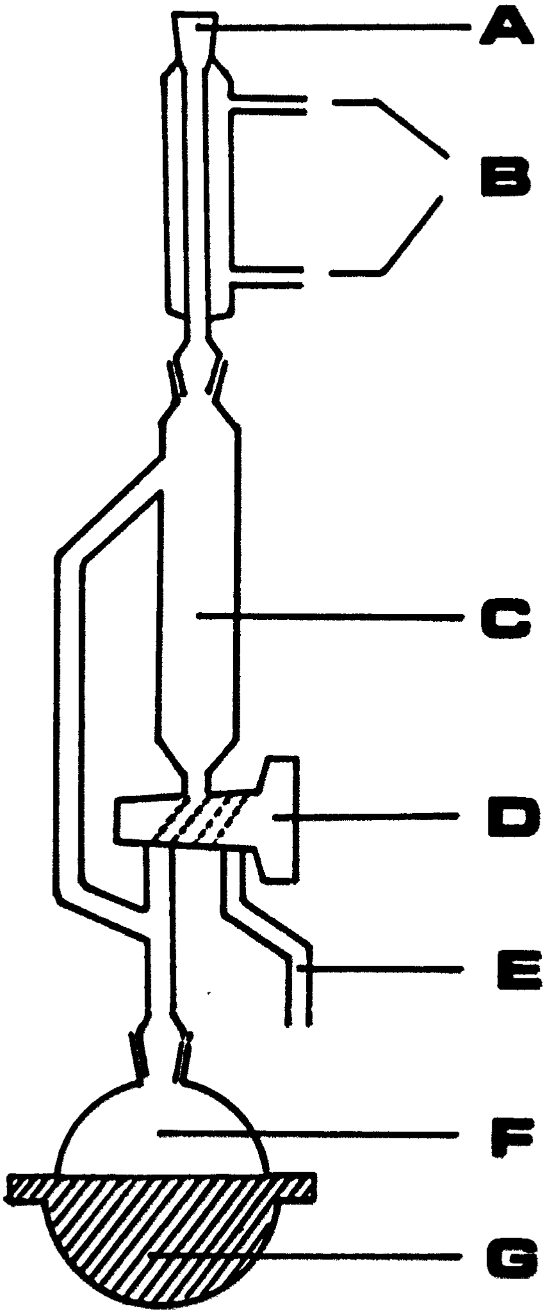
A
B
C
D
E
F
G

power of perchloric acid. Human whole blood samples were obtained from the Ames Laboratory medical department. Each 3-ml portions of whole blood samples were digested with 20 ml of a 1:1 volume/volume mixture of 70% perchloric and 70% nitric acids in the Bethge apparatus. Digestion was done under total reflux to prevent loss of volatile metal chlorides. A reflux time of 30 minutes was sufficient to transform the dark-colored mixture of blood and acids into a clear solution.

By adjusting the three-way stopcock, water condensate can be removed from the side-arm of the Bethge apparatus or returned to the boiling mixture. The oxidizing power of perchloric acid is directly proportional to its percent composition (concentration). For larger amounts of blood samples, water condensate can be removed from the side-arm in order to raise the perchloric acid concentration and increase the oxidizing power inside the digestion bottle.

### Wavemeter-computer interface

Accuracy, precision and sensitivity of this isotopic-ratio analysis scheme rely significantly on the reproducibility of good experimental hyperfine structures. The ring dye laser has a fairly good electronic wavelength-scanning mechanism with minimum scan-rate deviation. However, for our fitting scheme of hyperfine-component frequencies with ± 0.0005 $cm^{-1}$ accuracy, even slight deviation is unacceptable. Hence the Burleigh wavemeter is interfaced to the PDP 11 minicomputer so that signal data can be collected simultaneously with the corresponding frequency values. The I/O port (25-pin "D" connector) of the wavemeter is connected to the LPSDR Digital I/O port of the LPS-11 Laboratory Peripheral System as shown in Table 1. The LPS-11 real-time sub-system is interfaced with the PDP-11 computer via the Unibus. The LPSDR Digital I/O system consists of a 16-bit buffered input register and a 16-bit buffered output register. The programmed instructions control the transfer of data between the digital I/O registers and memory. The laser frequency value from the wavemeter in BCD code is read and converted to base-10 number by subroutine WAVE3, a program written in FORTRAN (See Appendix for all computer program listings). The frequency value is then displayed on the Laboratory Peripheral System's LEDs in real-time.

The wavemeter measures the laser wavelength by comparing the wavelength of the unknown laser with that of a prealigned built-in He-Ne laser. The measurement is made repeatedly and the frequency (or wavelength) value is updated on the LED display every 1.6 sec. The reliability of wavemeter-computer interface can be checked by comparing

Table 1. Pin Assignments for wavemeter-computer interface

| Burleigh wavemeter<br>I/O port 1 | | LPSDR Digital<br>I/O port | |
|---|---|---|---|
| Pin # | Designation | Pin # | Designation |
| 17 | BCD1 | 16 | RC2E1N1 |
| 5 | BCD2 | 15 | RC2E1N2 |
| 18 | BCD4 | 4 | RC2E1N3 |
| 6 | BCD8 | 12 | RC2E1N4 |
| 7 | Decimal pt. scan | 7 | RC2E1N5 |
| 1 | D6 scan | 13 | RC2E1N6 |
| 8 | End of scan | 6 | RC2E1N7 |
| 4 | D0 scan | 18 | RC2E1N8 |
| 16 | D1 scan | 22 | RC2E1N9 |
| 3 | D2 scan | 10 | RC2E1N10 |
| 15 | D3 scan | 19 | RC2E1N11 |
| 20 | Error scan | 24 | RC2E1N12 |
| 8 | End of scan | 2 | Ext. New Data Rdy. |

the frequency value displayed on the wavemeter LEDs with the one simultaneously displayed on the computer LEDs. (Not a single disagreement or error between the two values was detected for a test of as many as 10,000 consecutive comparisons.)

The wavemeter frequency-updating rate (every 1.6 sec) is too slow for our data-collection rate (every 0.5 sec). The result is inadequate resolution along the frequency coordinate with three or more optogalvanic signal values recorded for each frequency value, as shown in Figure 9. This problem is solved by using a 5-point data-smoothing routine to smooth the frequency coordinate. This is justified because the ring dye laser itself is stable to 40 MHz, whereas the wavemeter has a resolution of only 300 MHz. With simultaneous digitization of signal data and frequency values at high level of accuracy, excellent reproducibility of all experimental hyperfine profiles is achieved.

## Data treatment

All experimental hyperfine profiles are collected using the program OGE2M. The subroutine WAVE3 is called to collect the wavemeter frequency values. The program OGE2M collects 2

Figure 9. A typical, untreated experimental hyperfine profile digitized and stored in the computer (without smoothing of frequency coordinate)

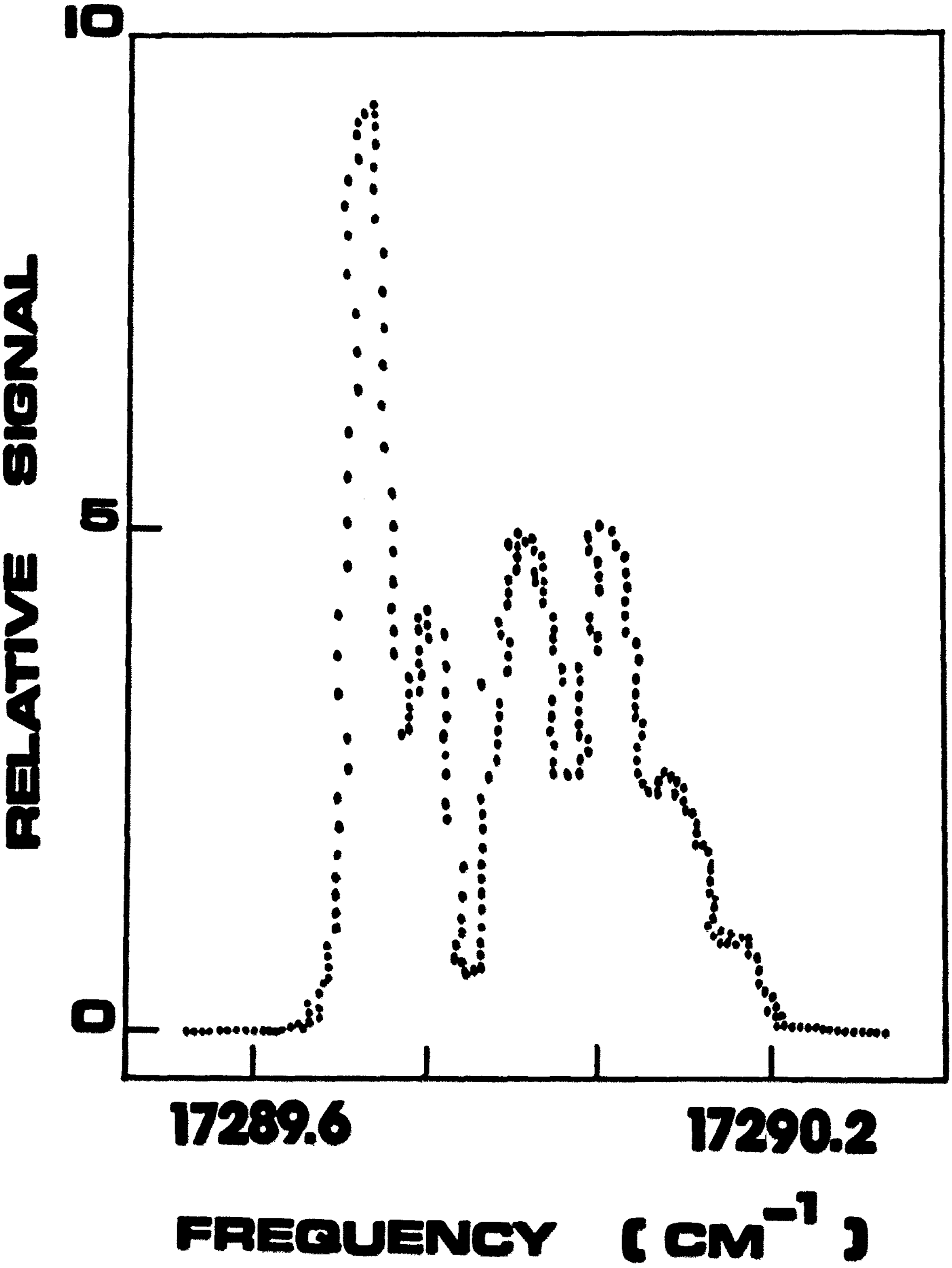
10
5
0
RELATIVE SIGNAL
17289.6
17290.2
FREQUENCY ( CM$^{-1}$ )

signal data and corresponding frequency values simultaneously every second, and displays the hyperfine structure on the graphics terminal. The optogalvanic signal data and the laser frequency values are alternatively displayed on the computer LEDs. Exact synchronization of starting time between the laser scan and the data-collection program is not necessary, since spectrum matching of all profiles is frequency-based rather than time-based. At the end of the laser scan, the hyperfine structure is stored under a previously specified FTN file number.

All calculations, including generation of theoretical profiles and least-squares fitting of experimental profiles, are done by using a Digital Equipment Corp. PDP 11/45 minicomputr (Maynard, MA) with a floating-point processor. Program RTCU generates theoretical hyperfine profiles using various ratio R and temperature T values. A single profile or a table of profiles (20x10 or 10x5 table) can be generated and stored on the disk within a few seconds.

Program GRAPH3 is used to inspect the reproducibility of all collected experimental profiles, by superimposing them on the graphics monitor. It is also used to determine the central frequencies $V_{0,n=1,12}$ of all the hyperfine components for a particular design of hollow-cathode lamp. Before matching the profiles, the computer determines the baseline of each experimental profile. Then an adjusted baseline is determined, and the whole profile is normalized with respect to its area. Theoretical profiles are generated for the scan range of 0.9 $cm^{-1}$ (27 GHz) using 200 data points with 0.0045 $cm^{-1}$ frequency increments. However, the same data point number (i.e. 1st to 200th) of the experimental profile may not have the identical frequency value. Hence a new set of frequency values, identical to that of the theoretical profile, is assigned to the experimental profile, and the corresponding optogalvanic signal intensities are computed. This allows the nth (n=1-200) data point of both profiles to have the same frequency value to the nearest $\pm 0.0005$ $cm^{-1}$. Least-squares fitting of profiles yields more reliable result by using this frequency-alignment routine.

Program LARA2 takes a baseline-substracted, area-normalized and frequency-aligned experimental profile and matches with each theoretical profile stored in the reference tables. The sum of squares of the deviations (SSD) is calculated for each theoretical profile. The isotope ratio information is then obtained from the theoretical profile that yields the least SSD. For experimental profiles with noisy background, 5 to 21-point third-degree polynomial smoothing routines are available in

LARA2 to reduce the noise level without substantially degrading the spectral resolution.

## Results and Discussion

### Hyperfine-component strengths

The six relative hyperfine-component strengths $K_{F'F}$ for both the copper 63 and copper 65 isotopes are calculated using equation 32, and tabulated in Table 2. The 6j symbols are calculated using the FORTRAN program 6J. Numerical values of some of the 6j symbols are also listed by Weissbluth (147). Both isotopes yield the same K values since they have the same nuclear angular momentum of $I=3/2$. Table 3 lists all twelve relative hyperfine-component strengths in the order they appear along frequency coordinate. Natural-abundance isotope ratio R of 2.235 is used to adjust the relative absorption strengths of the two isotopes, $K_{F'F}$ (Cu-63) and $K_{F'F}$ (Cu-65).

### Hyperfine-component central frequencies

Using the $K_{F'F}$ values listed in Table 3, the hyperfine-component central frequencies, $V_{0,n=1,12}$ , are calculated from data generated by a hollow-cathode lamp

Table 2. Relative hyperfine-component strengths for each copper isotope (For Cu I 578.2 nm line)[a]

---

$K_{32} = 1.0000$

$K_{21} = 0.3571$

$K_{22} = 0.3571$

$K_{11} = 0.3571$

$K_{12} = 0.0715$

$K_{01} = 0.1429$

---

[a] Both Cu-63 and Cu-65 isotopes have identical values.

Table 3. Relative hyperfine-component strengths for all twelve components (For Cu I 578.2 nm line)

---

$K_{32}$ ($^{63}$Cu) = 1.0000

$K_{32}$ ($^{65}$Cu) = 0.4474

$K_{21}$ ($^{63}$Cu) = 0.3571

$K_{22}$ ($^{63}$Cu) = 0.3571

$K_{21}$ ($^{65}$Cu) = 0.1598

$K_{22}$ ($^{65}$Cu) = 0.1598

$K_{11}$ ($^{63}$Cu) = 0.3571

$K_{12}$ ($^{63}$Cu) = 0.0715

$K_{01}$ ($^{63}$Cu) = 0.1429

$K_{11}$ ($^{65}$Cu) = 0.1598

$K_{12}$ ($^{65}$Cu) = 0.0320

$K_{01}$ ($^{65}$Cu) = 0.0639

---

which has a cathode made of copper with known isotope ratio. Table 4 lists the central frequencies calculated by using a solid copper cathode in our demountable hollow-cathode lamp, operated at 30 mA. The data calculated for a commercial hollow-cathode lamp (Perkin-Elmer Corp., Norwalk, CT) are also compared in Table 4. The slight difference between the central frequencies of the commercial lamp and the home-made lamp is mainly due to the difference in electric field strengths available for the two discharges. The electric field effect on hyperfine shift will be discussed later in this chapter. The Cu-63 - Cu-65 isotope shift is determined to be 0.067 ± 0.0005 $cm^{-1}$ and compares well with results reported by other workers as shown in Table 5 (101, 115 - 117).

The reliability of this isotopic-ratio measurement scheme depends significantly on how accurately these central frequencies of the hyperfine lines can be determined. To double check our calculated $V_{0,n}$ values, we used enriched copper-63 and copper-65 isotopes respectively for calculations of $V_{0,n=1-6}$ (Cu-63) and $V_{0,n=1-6}$ (Cu-65) separately. Copper-63 and copper-65 cathodes are prepared by depositing the individual isotope on a blank nickel cathode rod using a solution containing only the 99.89% enriched Cu-63 or 99.69% enriched Cu-65 isotopes

Table 4. Calculated hyperfine-component central frequencies

| | Commercial cathode | Demountable cathode |
|---|---|---|
| $V_{0,1}$ | 17289.724 $cm^{-1}$ | 17289.726 $cm^{-1}$ |
| $V_{0,2}$ | 17289.791 | 17289.796 |
| $V_{0,3}$ | 17289.882 | 17289.890 |
| $V_{0,4}$ | 17289.915 | 17289.918 |
| $V_{0,5}$ | 17289.959 | 17289.960 |
| $V_{0,6}$ | 17289.995 | 17289.991 |
| $V_{0,7}$ | 17290.000 | 17290.003 |
| $V_{0,8}$ | 17290.029 | 17290.031 |
| $V_{0,9}$ | 17290.057 | 17290.060 |
| $V_{0,10}$ | 17290.082 | 17290.091 |
| $V_{0,11}$ | 17290.116 | 17290.128 |
| $V_{0,12}$ | 17290.143 | 17290.148 |

Table 5. The Cu-63 - Cu-65 isotope shift for
Cu I 578.2 nm line

| | | |
|---|---|---|
| This work | 0.067 cm$^{-1}$ | + 0.0005 cm$^{-1}$ |
| Gerstenberger et al. (101) | 0.0655 | + 0.002 |
| Murakawa (117) | 0.0674 | + 0.0007 |
| Schuler and Schmidt (116) | 0.066 | |
| Ritschl (115) | 0.073 | |

respectively. Table 6 shows the central frequencies determined for each isotope and the combined result for all 12 hyperfine lines. Hyperfine structures of individual copper-63 and copper-65 isotopes are displayed in Figure 10 and Figure 11 respectively. Figure 12 illustrates the resulting convoluted spectrum for both isotopes. It is confirmed that the central frequencies determined by using separate individual isotopes agree very well with those determined from a natural-abundance copper sample.

### Abundance analysis

Theoretical profiles generated by using these $K_{F'F}$ and $V_{0,n}$ values are stored in reference tables in the computer for various values of isotope ratio R and temperature T. A typical reference table containing 20x10 theoretical profiles is illustrated in Figure 13. Theoretical profiles generated for different temperature values and an identical ratio value are stored in each row of the reference table. In each column of the table, theoretical profiles with identical temperature value and different ratio values are stored. Figure 14 and 15 display some of the profiles stored in a row and a column of the reference table respectively. In each figure, the ratio increment $\Delta R$ and temperature increment $\Delta T$ between the profiles are largely expanded in order to display the

Table 6. Central frequency values determined from hyperfine structures (HFS) of individual copper isotope

| From Cu-63 HFS | From Cu-65 HFS | Combined result |
|---|---|---|
| $V_{0.1}$ =17289.726 | $V_{0,1}$ =17289.796 | $V_{0,1}$ =17289.726 |
| $V_{0,2}$ =17289.890 | $V_{0,2}$ =17289.960 | $V_{0,2}$ =17289.796 |
| $V_{0,3}$ =17289.918 | $V_{0,3}$ =17289.991 | $V_{0,3}$ =17289.890 |
| $V_{0,4}$ =17290.003 | $V_{0,4}$ =17290.091 | $V_{0,4}$ =17289.918 |
| $V_{0,5}$ =17290.031 | $V_{0,5}$ =17290.128 | $V_{0,5}$ =17289.960 |
| $V_{0,6}$ =17290.060 | $V_{0,6}$ =17290.148 | $V_{0,6}$ =17289.991 |
|  |  | $V_{0,7}$ =17290.003 |
|  |  | $V_{0,8}$ =17290.031 |
|  |  | $V_{0,9}$ =17290.060 |
|  |  | $V_{0,10}$ =17290.091 |
|  |  | $V_{0,11}$ =17290.128 |
|  |  | $V_{0,12}$ =17290.148 |

Figure 10. Doppler-broadened hyperfine structure of copper-63 isotope. Simulated for 1400 K (Top) and 20 K (Bottom)

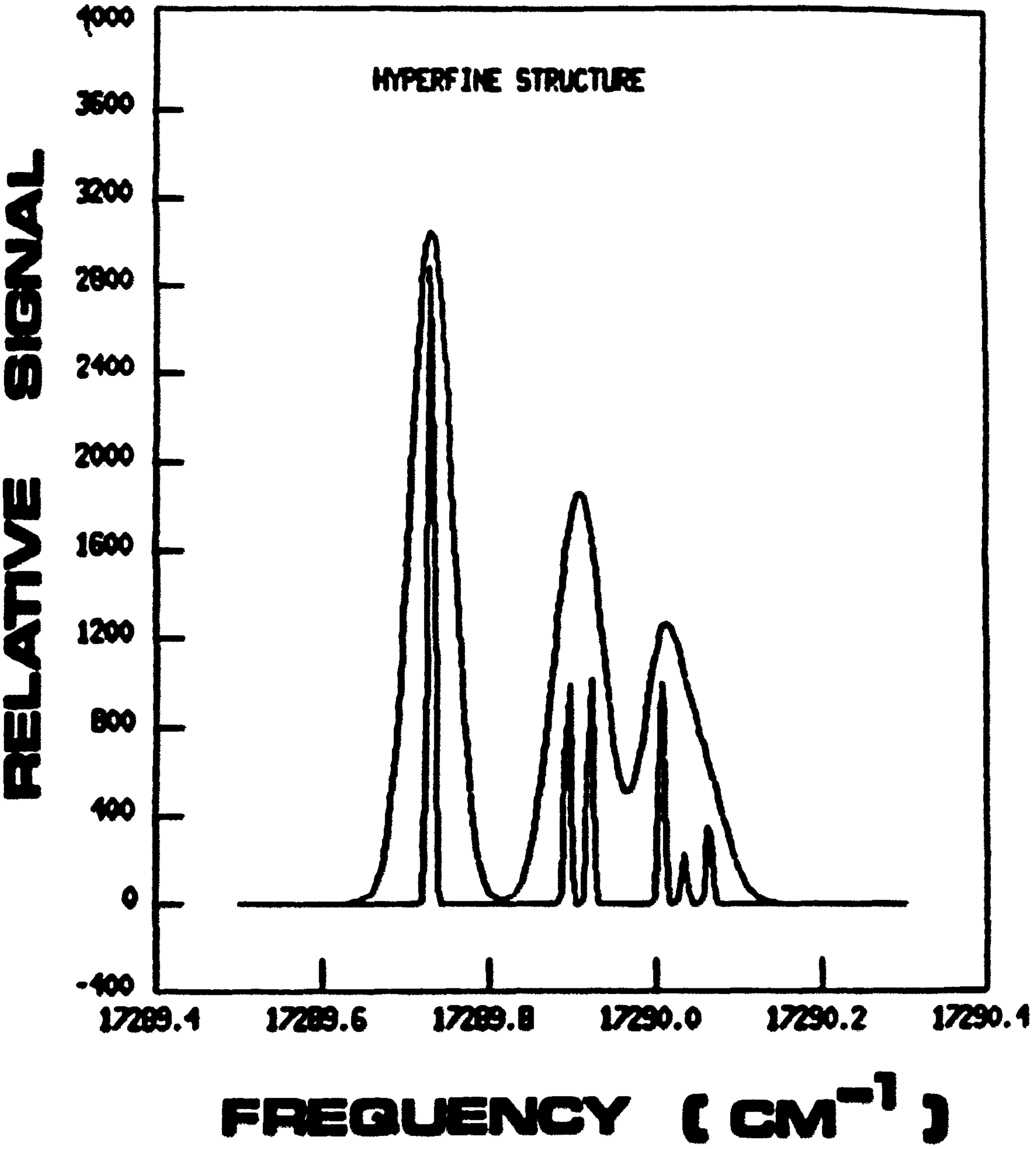
HYPERFINE STRUCTURE
RELATIVE SIGNAL
4000
3600
3200
2800
2400
2000
1600
1200
800
400
0
-400
17289.4
17289.6
17289.8
17290.0
17290.2
17290.4
FREQUENCY (CM$^{-1}$)

Figure 11. Doppler-broadened hyperfine structure of copper-65 isotope. Simulated for 1400 K (top) and 20 K (bottom)

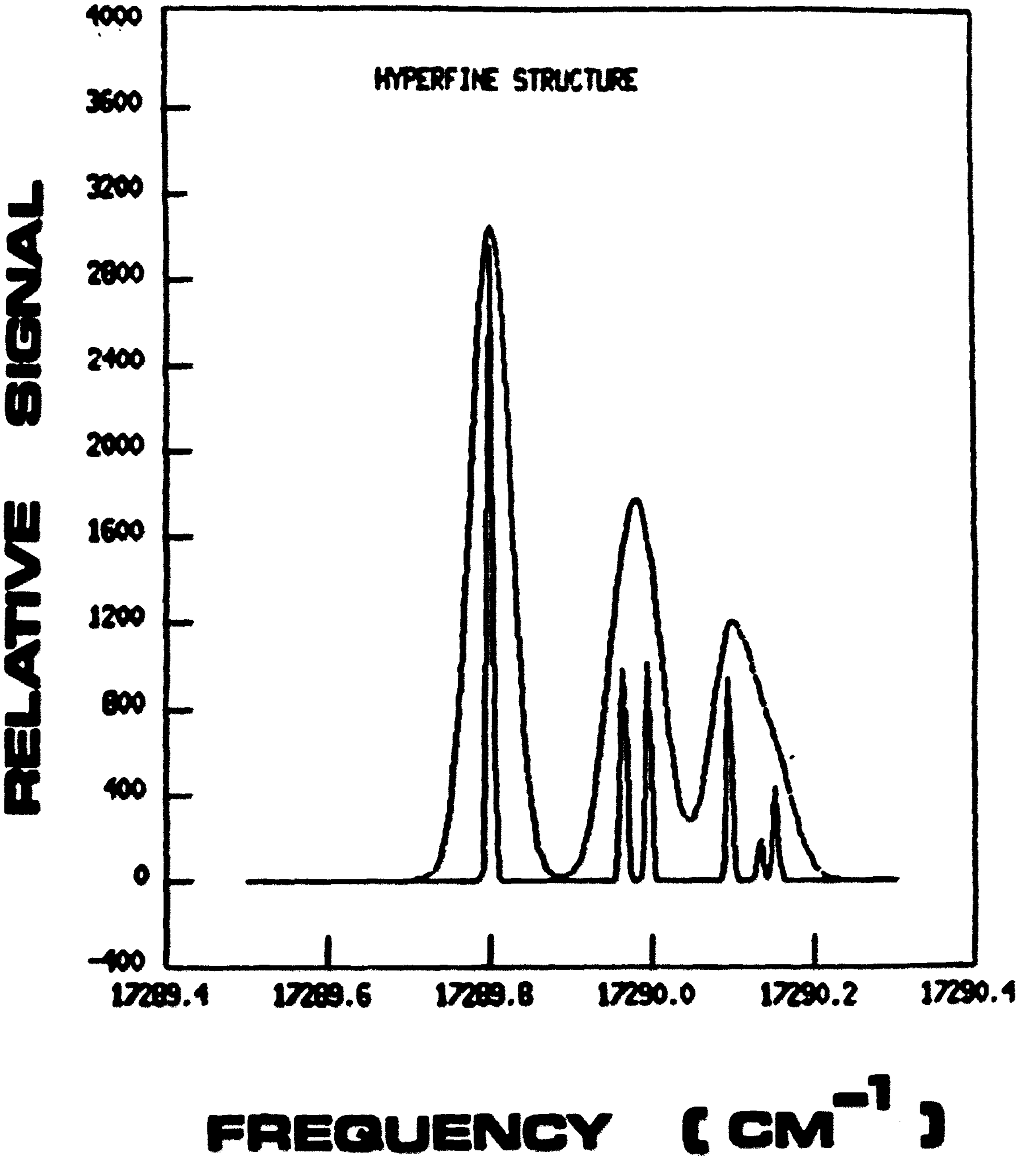
HYPERFINE STRUCTURE
RELATIVE SIGNAL
4000
3600
3200
2800
2400
2000
1600
1200
800
400
0
-400
17289.4
17289.6
17289.8
17290.0
17290.2
17290.4
FREQUENCY ( CM⁻¹ )

Figure 12. Hyperfine structure simulated by using central frequencies determined for individual copper isotopes

Solid line - convoluted total profile

Dashed line - copper-63 isotope profile

Dotted line - copper-65 isotope profile

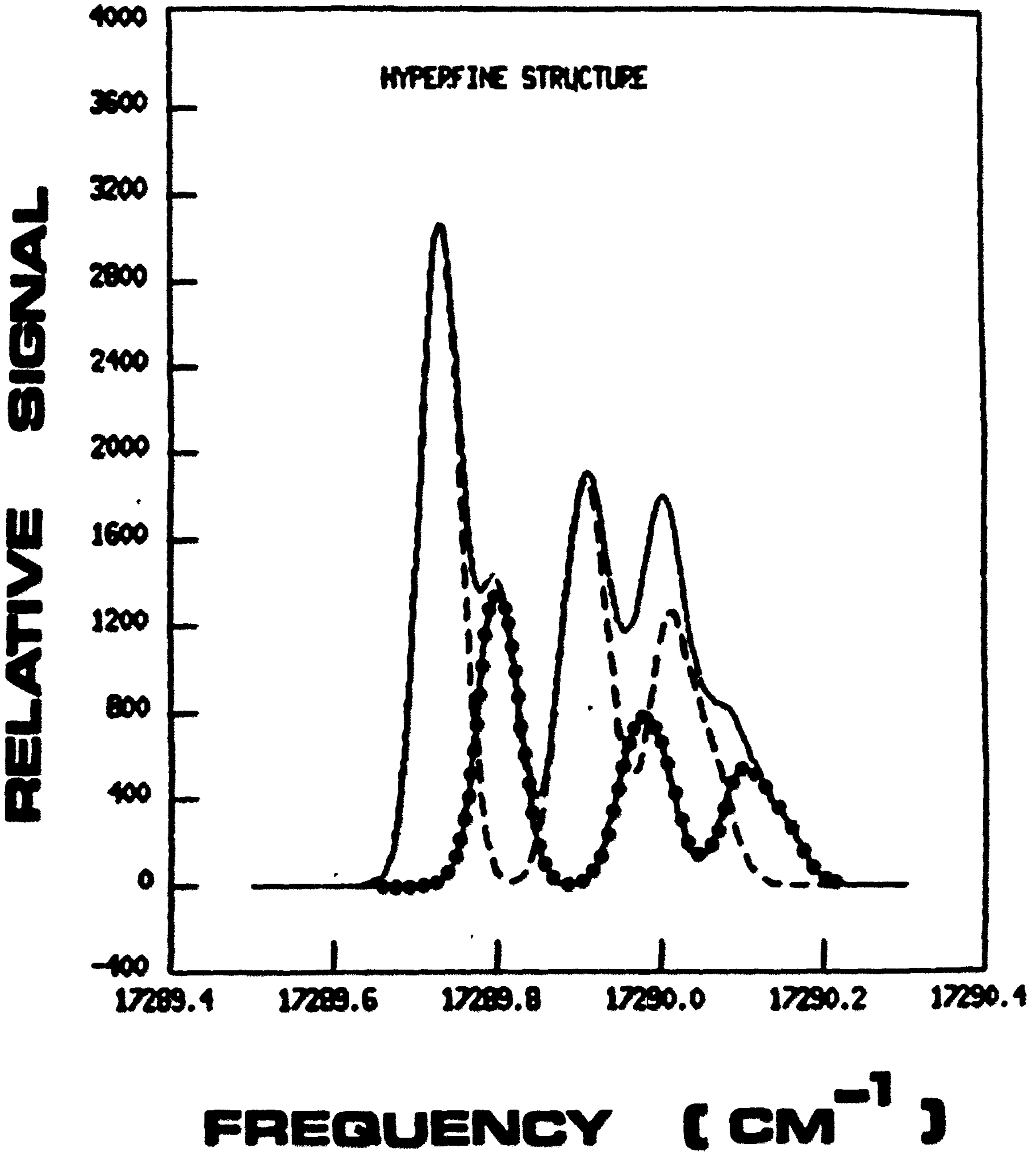
HYPERFINE STRUCTURE
RELATIVE SIGNAL
4000
3600
3200
2800
2400
2000
1600
1200
800
400
0
-400
17289.4
17289.6
17289.8
17290.0
17290.2
17290.4
FREQUENCY (CM$^{-1}$)

**Figure 13.** A reference table containing 20x10 theoretical profiles

$$
\begin{array}{ccccc}
R_1T_1 & R_1T_2 & R_1T_3 & \cdot & R_1T_{10} \\
R_2T_1 & R_2T_2 & & & \cdot \\
R_3T_1 & & R_3T_3 & & \cdot \\
\cdot & & & \cdot & \cdot \\
R_{20}T_1 & \cdot & \cdot & \cdot & R_{20}T_{10}
\end{array}
$$

Figure 14. Theoretical profiles stored in a row of the reference table
Cu-63/Cu-65 ratio = 2.235
Temperature = 10, 200, 400, 600, 800, 1000, 1200, 1400, 1600, 1800, 2000 K

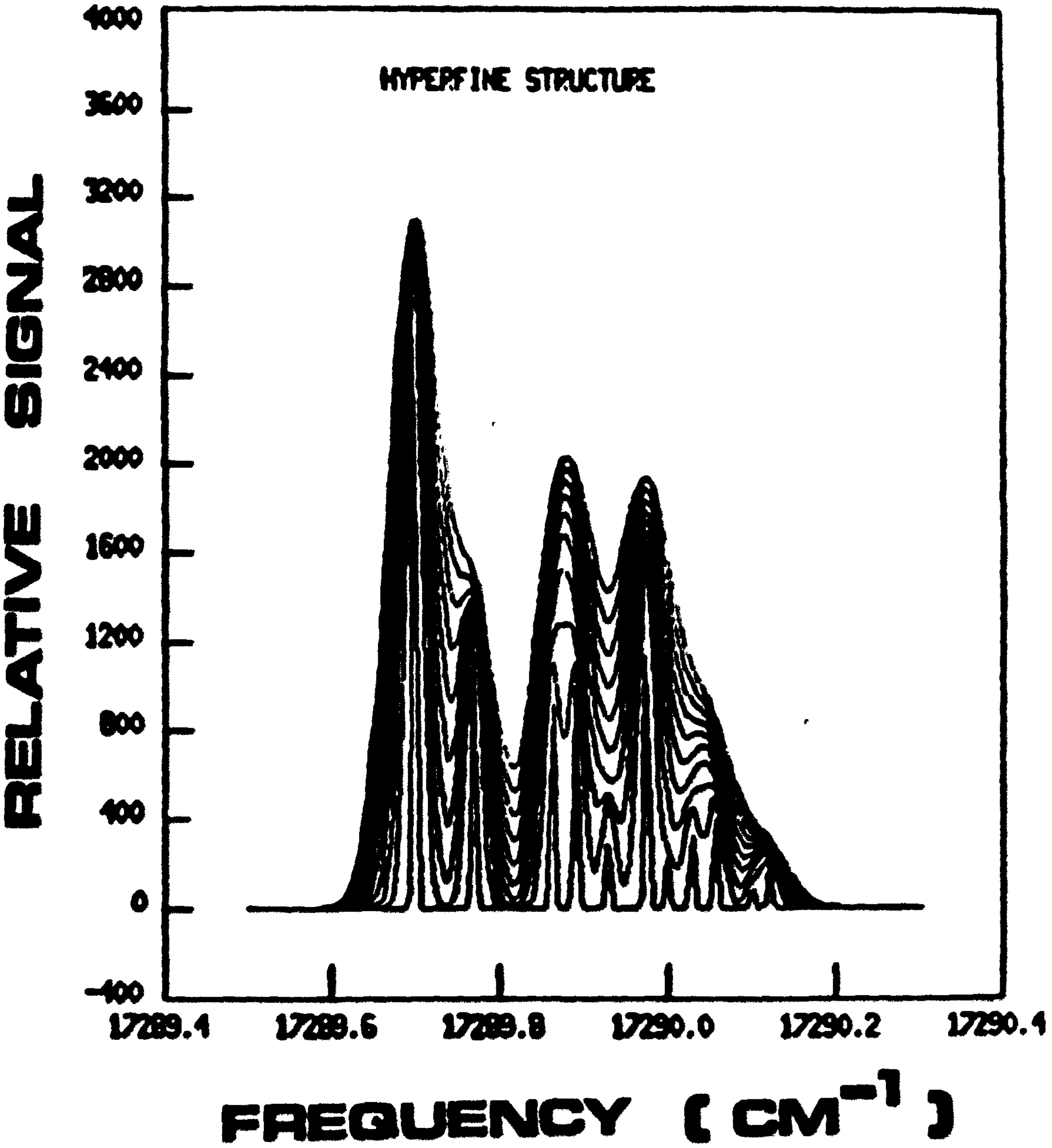
HYPERFINE STRUCTURE
RELATIVE SIGNAL
4000
3600
3200
2800
2400
2000
1600
1200
800
400
0
-400
17289.4
17289.6
17289.8
17290.0
17290.2
17290.4
FREQUENCY (CM$^{-1}$)

Figure 15. Theoretical profiles stored in a column of the reference table

Temperature = 1400 K

Cu-63/Cu-65 ratio = 5.4, 5.0, 4.6, 4.2, 3.8,
3.4, 3.0, 2.6, 2.2, 1.8,
1.4, 1.0

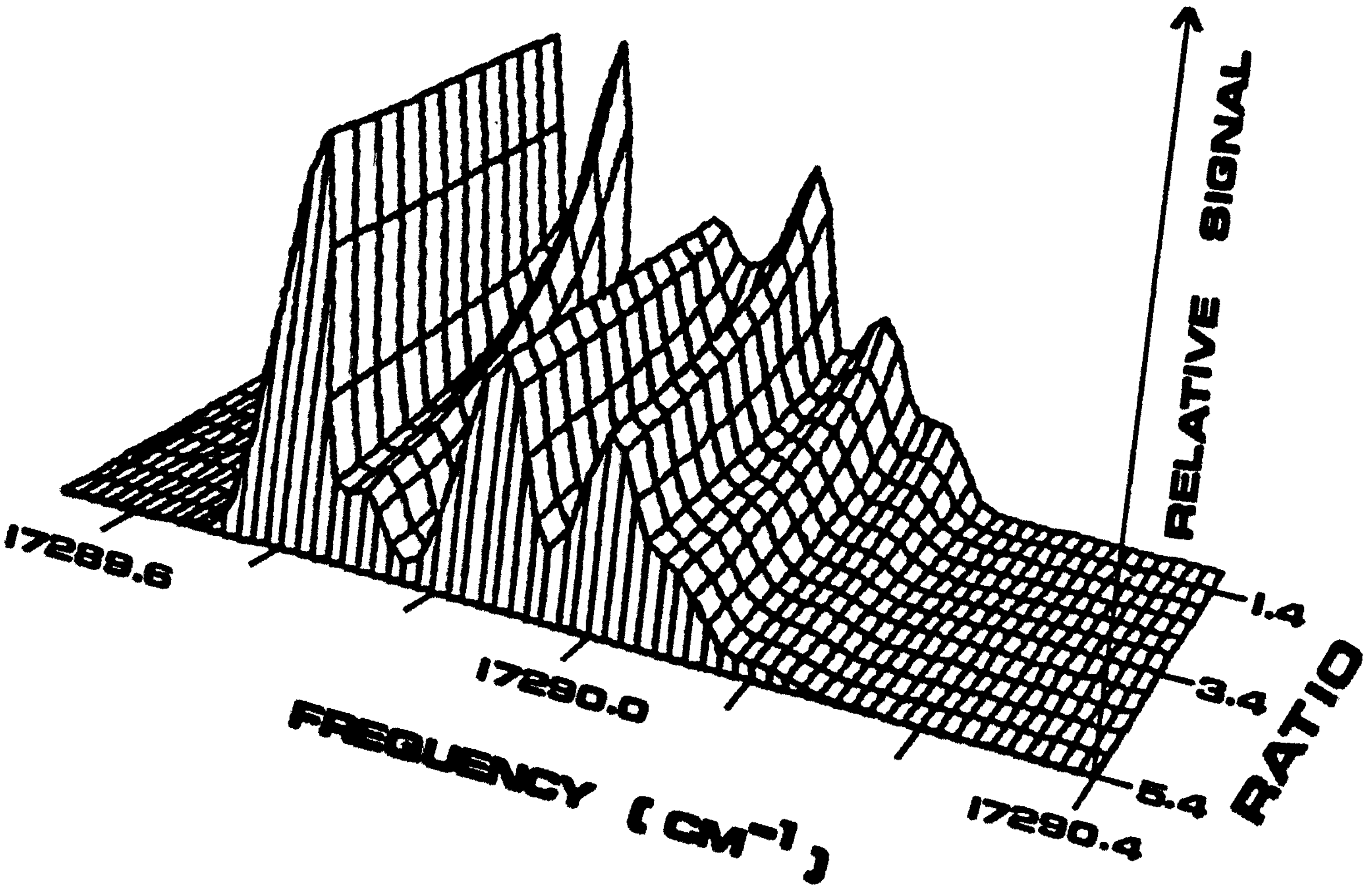
RELATIVE SIGNAL
17289.6
17290.0
17290.4
FREQUENCY ( CM⁻¹ )
1.4
3.4
5.4
RATIO

profiles clearly. Smaller $\Delta R$ (0.0625) and $\Delta T$ (100 K) values are used in most reference tables to achieve good accuracy and precision.

The program LARA2 takes baseline-substracted, area-normalized and frequency-aligned experimental profile and fit it with each theoretical profile in the reference tables. Figure 16 shows good spectral fitting of the experimental profile with the theoretical profile that yields the least sum of squares of the deviation (SSD). The reliability and accuracy of the ratio calculation depend on the ability of the computer to decide which theoretical profile yields the least SSD. To ensure the high level of confidence, the calculated surface of SSD in the entire range of R and T values should have only a single minimum point, forming a smooth "hole". Also the minimum point must always fall within the bounds of the table. Figure 17 illustrates a typical calculated surface of SSD over a 20x10 reference table, showing that such conditions are satisfied.

The percent abundances of Cu-63 and Cu-65 isotopes are determined using the demountable cathode lamp deposited with natural-abundance copper and enriched copper isotopes. A summary of these results is listed in Table 7. The reliability and accuracy of these ratio calculations are tested for some extreme cases, such as calculation for a

Figure 16. Fitting of the atomic hyperfine profile Solid line, theoretical profile; circles, experimental profile

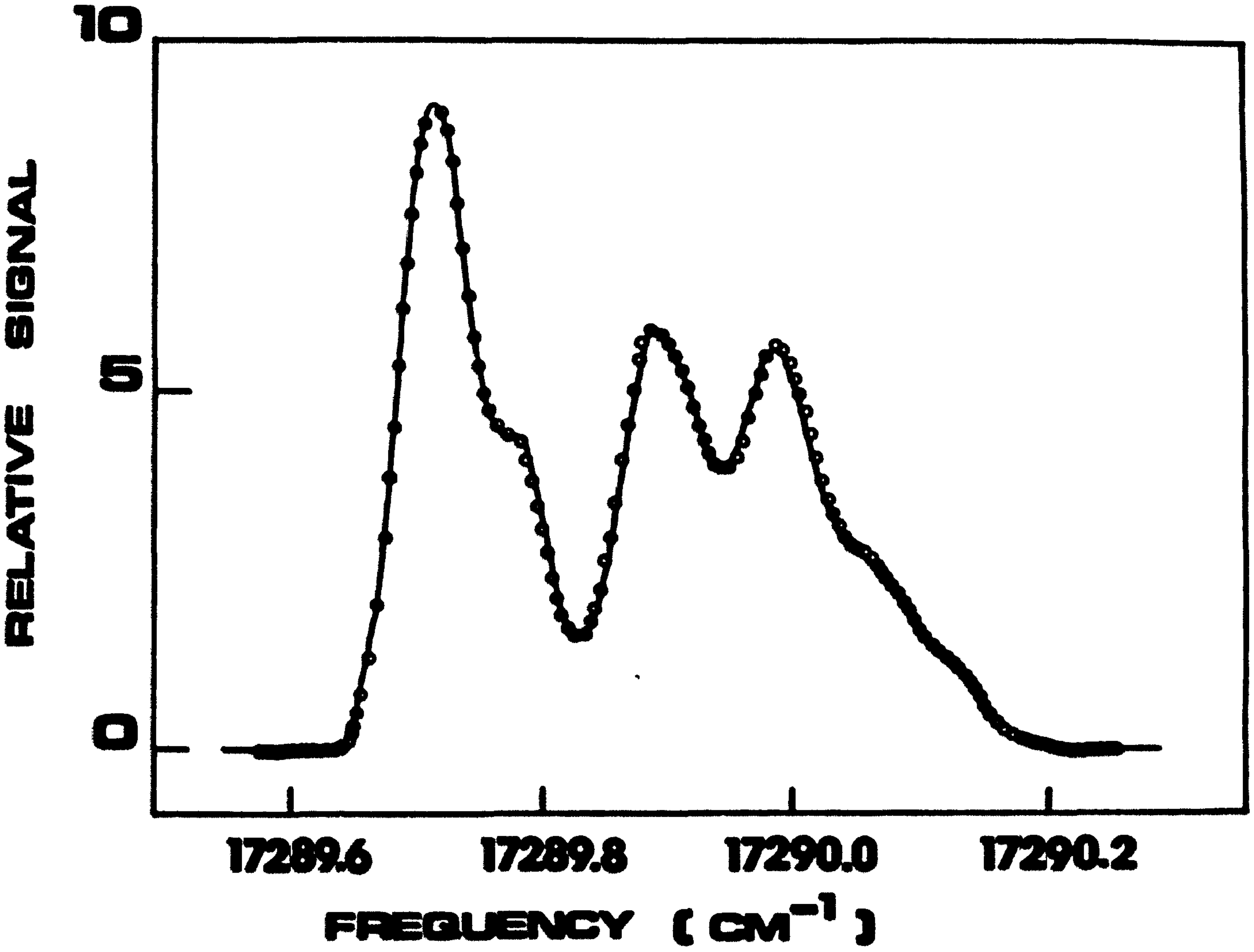
10
5
0
RELATIVE SIGNAL
17289.6
17289.8
17290.0
17290.2
FREQUENCY ( CM$^{-1}$ )

Figure 17. Calculated surface of the SSD of the fitting covering a typical reference table

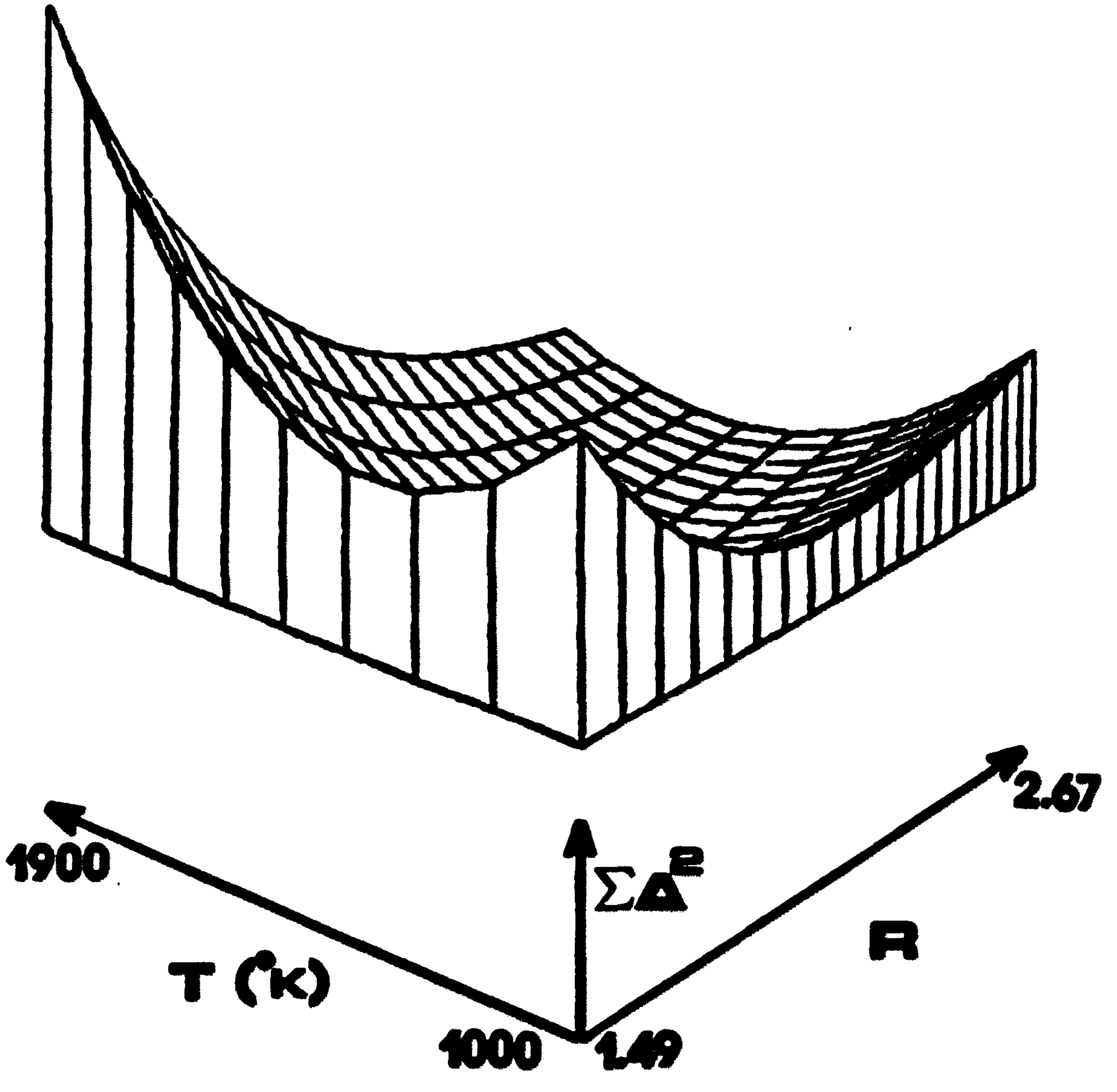
1900
T (°K)
1000
$\Sigma\Delta^2$
1.49
R
2.67

Table 7. Determination of isotope abundances

| Sample concentration[a] | Actual % | | Experimental % | |
|---|---|---|---|---|
| | $^{63}$Cu | $^{65}$Cu | $^{63}$Cu | $^{65}$Cu |
| 47 ppm | 69.09 | 30.91 | 67.3 ± 1.5 | 32.7 ± 1.5 |
| 9.3 ppm | 69.09 | 30.91 | 69.0 ± 2.2 | 31.0 ± 2.2 |
| 1.6 ppm | 69.09 | 30.91 | 70.1 ± 3.1 | 29.9 ± 3.1 |
| 50 ppm | 91.0 | 9.0 | 91.0 ± 0.3 | 9.0 ± 0.3 |
| 94 ppm | 95.3 | 4.7 | 96.0 ± 1.0 | 4.0 ± 1.0 |

[a] Concentrations refer to sample solution from which copper is deposited onto the nickel cathode rod.

minor isotope (5% abundance) in the presence of a major isotope (95% abundance). As shown in Table 7, ratio analysis can be performed successfully with good accuracy and precision even for these cases. The method is also tested for trace-concentration ratio analysis by using a cathode rod deposited with very small amount of copper (a few micrograms). Both the accuracy and the precision are in the ± 1% range for concentrations at the 50 ppm level, and about ± 2% at 9 ppm concentration level. Since concentrations mentioned above refer to sample solution from which copper is deposited onto the nickel cathode, the actual amount of deposited copper depends on how complete the electrodeposition process is. Although total copper quantitative detection can be done at much lower concentration than 1 ppm, the accuracy of ratio analysis decreases because of the distortion of hyperfine structure at very weak signal levels.

## Applications

Human whole blood contains 20 - 50 μg/ml copper and urine copper excretion of a person is 200 - 500 μg in a 4-hr period. These biological samples provide sufficient amounts of copper to be deposited on the cathode rod. A 3-ml portion of human blood sample was analyzed, and as expected, the isotope ratio determined was equal to the natural-abundance ratio of 2.235, since only natural-abundance copper is available in diet. Therefore, it is demonstrated that a resonably small amount of biological sample can be used for ratio calculations without tedious sample preparations, and that matrix effects are not important. This isotopic-ratio analysis scheme allows one to use stable copper isotope as tracer to study copper metabolism and to determine where and at what rate copper is distributed, absorbed and accumulated. This is useful in diagnosis of diseases such as Wilson's disease (120, 121), where abnormal regulation of copper in various human tissues and organs, including brain, cornea, kidney and liver, causes widespread brain damage and functional defects of the kidneys and eyes. Radioactive Cu-64 and Cu-67 isotopes have been most frequently used as tracer isotopes to monitor the copper excretion rate in the serum, urine and tissues of patients with Wilson's disease (120, 121, 148 - 150). Radioactive isotopes were required for the methods used by these workers in order to distinguish the tracer copper from the natural copper in diet. However, using our ratio analysis scheme, non-hazardous stable isotopes can be used for the same clinical studies, since copper from diet has the known natural-abundance ratio and can be easily distinguished.

Since most elements have at least one isotope possessing non-zero nuclear angular momentum I, each of these isotopes yields two or more hyperfine splittings depending on the optical transition. Therefore unique hyperfine structures for these elements are available for many optical transitions, and our isotopic-ratio analysis scheme can be applied to all these elements by using appropriate laser excitation sources. All information necessary to generate theoretical profiles for any element is readily available once the optical transition is known, and no prior knowledge or calculation of isotope shift effects is required. Cu I 578.2 nm transition is probably one of the most difficult cases because of the complexity and congestion of hyperfine lines. For elements with well-resolved hyperfine lines (e.g. Pb I 601.2 nm transition), deconvolution is not necessary, and even higher precision can be expected for ratio calculations.

Application of this scheme is useful not only in clinical studies as demonstrated, but also in environmental analysis such as the identification of pollution source, by use of tracer isotopes. For example, environmental lead poisoning is a serious medical problem which can result in severe sickness and detrimental effects on the intellectual development and behavior of children. The general population is exposed to elevated levels of lead in air, water and foods, because lead has been manufactured into such useful products as cooking utensils, tin cans, leaded gasoline, batteries, pigments, pottery and lead-laden paint and plumbing in older homes. Research efforts have been directed toward finding correlations of blood-lead levels with paint-lead levels, gasoline-lead levels and pottery-lead levels (151 - 154). However, it is still not clear which environmental lead source is the most dangerous. Our isotopic-ratio analysis scheme could be applied to help solve this controversy.

It should also be useful in geochronological studies, including the determination of the source and age of coastal waters and oceanic rock samples. The natural abundances of the stable isotopes of lead can be used to characterize and identify natural and industrial sources of lead in the coastal waters (155). The composition of Pb-204, Pb-206, Pb-207 and Pb-208 stable isotopes is related to the geological evolution or age of the ore body, because the latter three isotopes are radiogenically derived from U-238, U-235 and Th-232 respectively, whereas Pb-204 has remained constant with geologic time (156). The ratio Pb-206/Pb-207 is a good indicator for comparing lead sources, since the ratio is geographically different depending on whether the source is near an urban center (gasoline lead) or a mine tailing. The isotopic compositions of Pb, Sr and Nd are also useful as geochemical tracers to clarify the origins of oceanic rock samples (157 - 160). The Pb-210 isotope (half life = 22.26 ± 0.22 yr) is another useful geochronological tool for dating recent deposits of the past 150 years (161 - 163).

Our ratio analysis scheme is even applicable for detection of art forgeries by characterization and authentication of paintings, based on the isotopic ratios of an artist's lead pigment (164 - 165). Since lead ores from different mining regions throughout the world contain quite different abundances of lead 204, 206, 207 and 208 isotopes, the isotope ratios serve as a "fingerprint" of a lead-pigment source. Artists in various stages of the history were accessible to only certain lead ore deposits. Hence their paintings can be characterized and identified based on the isotope ratios of the lead pigment.

### Stark effect

As shown in Table 4, the hyperfine-component central frequencies $V_{0,n=1-12}$ for the commercial cathode discharge and the demountable cathode discharge were found to be slightly different. The major contributing factor is the electric-field shift, caused by the difference in electric field strengths available for the two lamps. Electric field strength between cathode and anode depends on the dimension and geometry of the electrodes, and the distance between them. The electric-field effect on hyperfine shift was tested using the demountable hollow-cathode lamp. By modifying the position of the anode tungsten rod inside the lamp, two different electric fields (volt / electrode distance) were achieved between the electrodes. Table 8 shows the calculated hyperfine-component frequencies at two different electric fields for the same cathode lamp operated under otherwise identical experimental conditions. As expected, the higher electric field (348 V/mm) shifted the hyperfine lines toward higher frequencies. It is interesting to note that with some modification of the demountable cathode lamp, this electric-field effect could be used for wavelength modulation of the optogalvanic signal in order to improve the signal-to-noise ratio and the sensitivity.

### Pressure effects

The pressure effect on hyperfine-component frequencies was also tested for the useful range of neon gas pressures in the demountable cathode discharge. The discharge can be

Table 8. Electric field effect in demountable discharge

| | Demountable discharge electric field | |
|---|---|---|
| | 14 V/mm | 348 V/mm |
| $V_{0,1}$ | 17289.720 $cm^{-1}$ | 17289.729 $cm^{-1}$ |
| $V_{0,2}$ | 17289.789 | 17289.798 |
| $V_{0,3}$ | 17289.885 | 17289.889 |
| $V_{0,4}$ | 17289.917 | 17289.921 |
| $V_{0,5}$ | 17289.960 | 17289.964 |
| $V_{0,6}$ | 17289.995 | 17289.999 |
| $V_{0,7}$ | 17289.997 | 17290.001 |
| $V_{0,8}$ | 17290.020 | 17290.029 |
| $V_{0,9}$ | 17290.057 | 17290.066 |
| $V_{0,10}$ | 17290.075 | 17290.079 |
| $V_{0,11}$ | 17290.121 | 17290.130 |
| $V_{0,12}$ | 17290.140 | 17290.149 |

operated from about 2 to 7 torr of neon gas pressure without sacrificing the stability or intensity of the optogalvanic signal. At pressure higher than 10 torr, electrical arcing between the electrodes becomes a noise source, and at pressure lower than 1 torr, desirable sputtering energy can not be maintained. Hyperfine structures measured at different neon pressures (2.6 and 7.1 torr) were compared. No significant difference was observed. Therefore, the discharge can be operated over a reasonably wide range of useful gas pressures, without affecting the hyperfine frequencies. Hence it is not necessary to set the pressure exactly the same each time, in order to achieve reproducible hyperfine structures.

### Noise considerations

The effect of an excessive baseline noise level on the ratio calculations was also tested. This was done by analyzing some noisy spectra and determining the limit of tolerable noise level at which the accuracy and precision would not be sacrificed significantly. Hyperfine profiles with various levels of baseline noise were generated by using Gaussian noise simulation. Magnitude of noise level (peak-to-peak) was determined by the random number generator of the computer using the Gaussian distribution equation,

$$(1/N) \int_{-x}^{x} \exp\,(-E^2/2s^2)\ dE = R1 \qquad (38)$$

where R1 ( $0 < R1 < 1$ ) is the probability that the data point will be in the range $-x$ to $x$ . R1 values between 0 and 1 were generated by the radom number generator and for each R1 value a $x$ value was calculated. $x$ is the magnitude of noise level to be simulated into a hyperfine profile. N is a normalization factor and s is used as an amplification factor to simulate various degree of noise level. First a hyperfine profile with 200 data points (y) is generated. For each data point, a random number R1 is used to determine noise level x. A second random number R2 is then used to decide whether the noise level x should be added to or substracted from the original hyperfine profile. If R2 is greater than 0.5, x is added to y to obtain the noisy profile z (i.e. $z=y+x$), and if R2 is less than 0.5, x is substracted from y (i.e. $z=y-x$). Figure 18 illustrates four hyperfine profiles with various levels of Gaussian noise amplification. The effect of spectral noise on ratio calculations was tested for each noise amplification level, and the result is shown in Table 9 . For s=2 (Figure 18 A), the noise level is too low to induce any error. For noise levels of s=6, 10 and 14, the

Figure 18. Hyperfine profiles with various level of Gaussian noise amplification. (A) s=2; (B) s=6; (C) s=10; (D) s=14

The noise levels of most experimental profiles are not higher than that of (B)

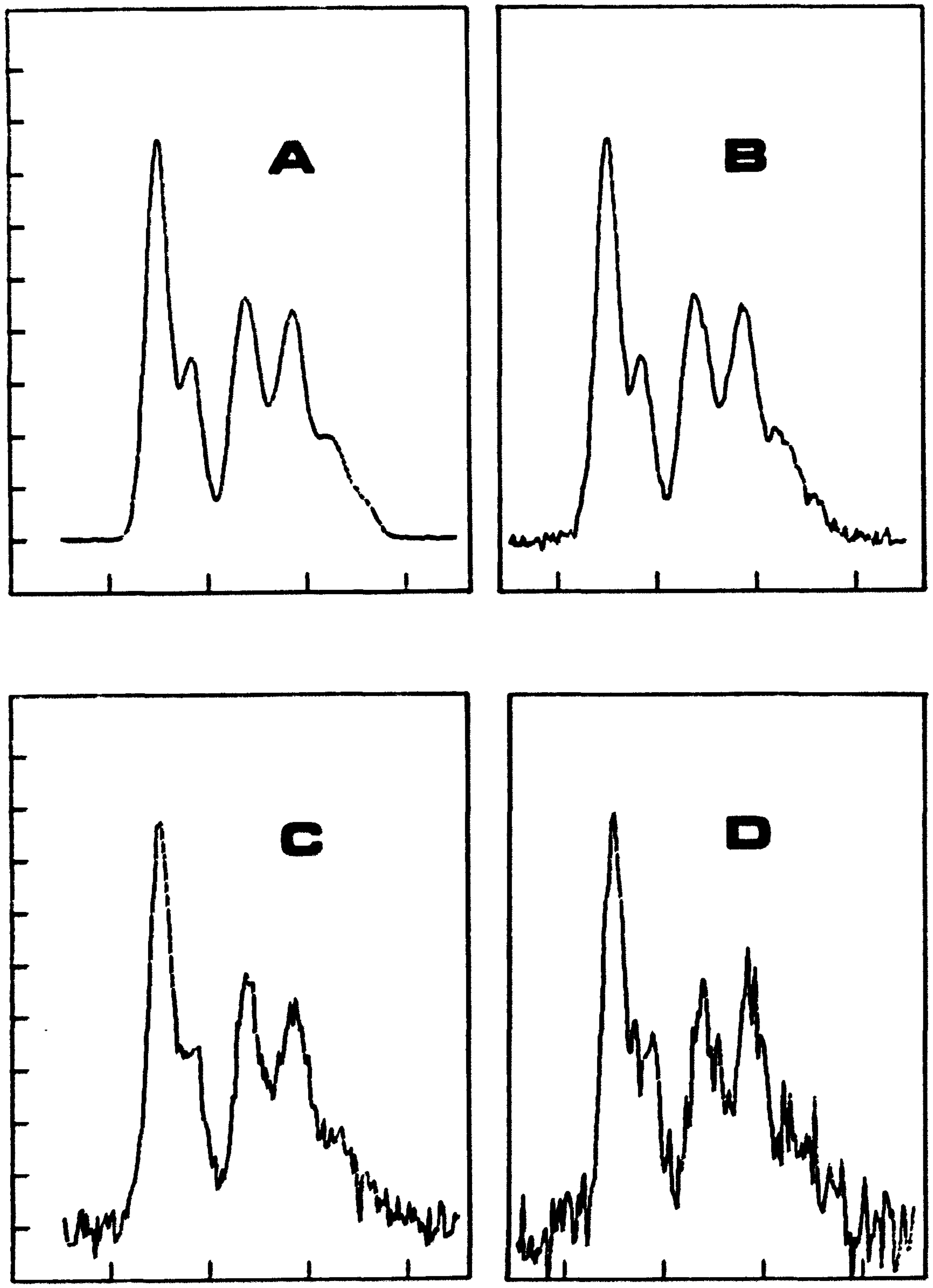
A
B
C
D

Table 9. Spectral noise effect on abundance calculation

| No. | Actual % Cu-63 | Calculated % Cu-63 | | | |
|---|---|---|---|---|---|
| | | s = 2 | s = 6 | s = 10 | s = 14 |
| 1 | 69.1 | 69.1 | 70.2 | 70.2 | 72.3 |
| 2 | 69.1 | 69.1 | 70.2 | 71.3 | 70.2 |
| 3 | 69.1 | 69.1 | 69.1 | 71.3 | 71.3 |
| 4 | 69.1 | 69.1 | 69.1 | 69.1 | 73.2 |
| 5 | 69.1 | 69.1 | 70.2 | 70.2 | 73.2 |
| 6 | 69.1 | 69.1 | 69.1 | 69.1 | 70.2 |
| 7 | 69.1 | 69.1 | 69.1 | 67.9 | 70.2 |
| 8 | 69.1 | 69.1 | 69.1 | 69.1 | 71.3 |
| 9 | 69.1 | 69.1 | 69.1 | 67.9 | 69.1 |
| 10 | 69.1 | 69.1 | 69.1 | 69.1 | 70.2 |
| Mean | | 69.1 | 69.4 | 69.5 | 71.1 |
| Standard Deviation | | 0.0 | 0.5 | 1.2 | 1.4 |

Figure 19. Spectral-noise effect on isotopic-abundance calculations
(Actual % Cu-63 is 69.1%)

Although excessive noise levels are simulated to test the effect on these calculations, the actual noise level of most experimental profiles are less than that of Figure 18B (s=6)

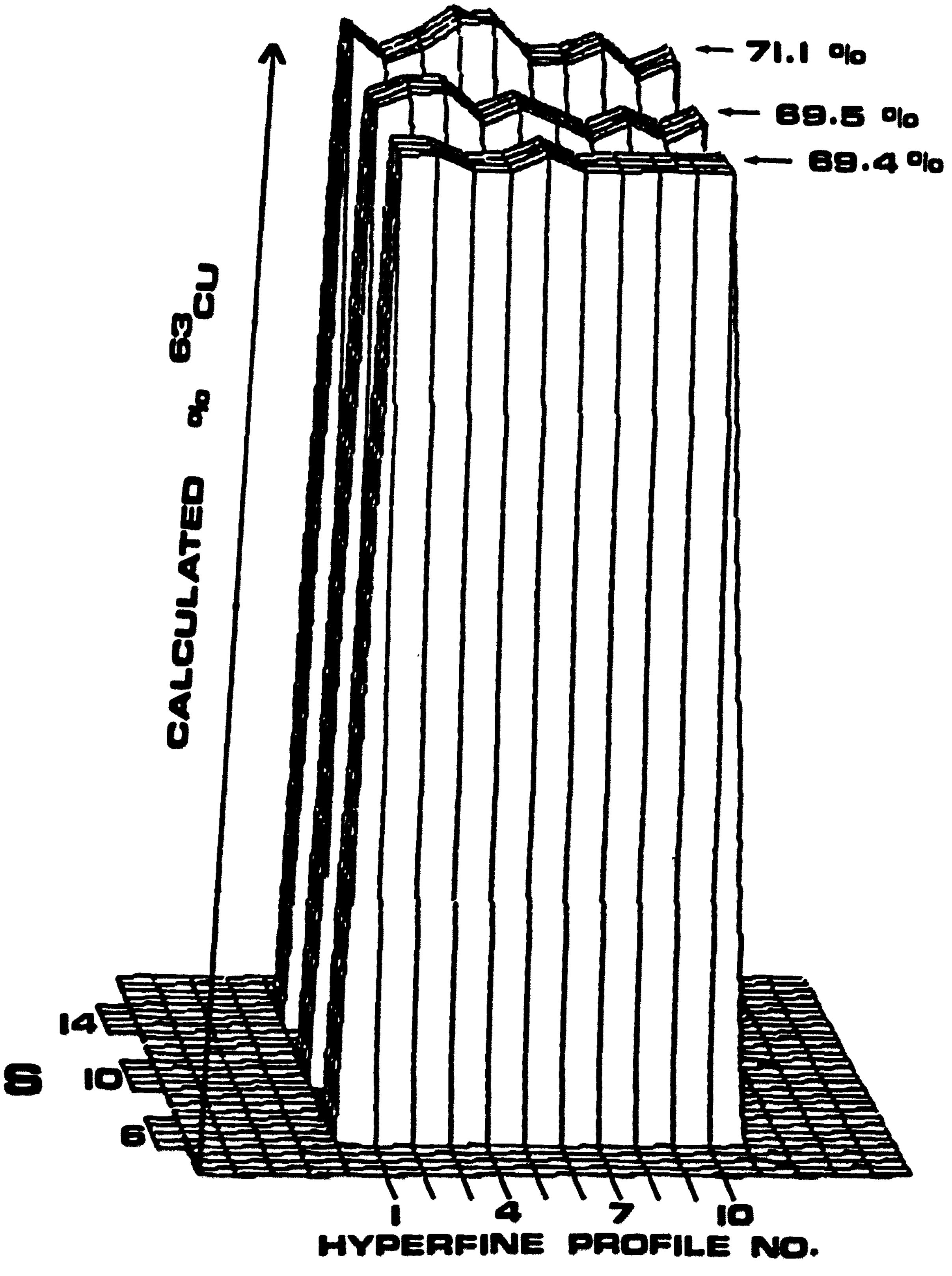
71.1 %
69.5 %
69.4 %
CALCULATED % $^{63}$CU
S
14
10
6
1
4
7
10
HYPERFINE PROFILE NO.

accuracy and precision are affected proportionally as shown in Table 9 and Figure 19.

Although excessive noise levels are simulated to test the noise effect on these calculations, the actual noise levels of all experimental profiles collected are less than that of Figure 18 B. It is interesting to note that even at noise level of s=14 (Figure 18 D), the accuracy and precision are not significantly affected. Furthermore, the ratio calculations of noisy profiles can be improved by using the third-degree polynomial smoothing routines of the program LARA2. Hence it is apparent that our isotopic-ratio calculation scheme has fairly good tolerance for spectral noise.

## Conclusions

We have demonstrated a novel method for determining isotopic abundances in complex samples. It benefits from many advantages of the optogalvanic spectroscopy including: (A) direct electrical signal generation from optical absorption and elimination of all optical signal measurement devices, such as collection optics, monochromators and PMTs, and the optical background noises, such as Raleigh and Raman scattering and room light; (B) the experimental resolution is limited by the analyte bandwidth itself rather than the spectrometer slit function as in conventional spectroscopic techniques; (C) useful contribution of the collisional processes; (D) higher limit of useful laser power; (E) linear dynamic range of 5 orders of magnitude and (F) high sensitivity.

The advantages of using a discharge as the atomizer include (G) narrower Doppler linewidth and (H) negligible Lorentzian broadening because of the lower temperature and pressure of the discharge plasma, compared to, for example, those of an analytical flame. Because of the high electron sputtering energy, the discharge also provides (I) higher collisional excitation energy. Although analytical flames provide more convenient way of analyte introduction, the simple electrodeposition step used for preparing the discharge tube is an effective procedure for concentration of the analyte from very dilute solution.

This scheme yields (J) abundances of all isotopes present, with a single sweep of the laser frequency and within a few seconds of calculation time. This is more efficient than some mass spectrometric methods where the peak-match unit has to be switched between the exact masses of the isotopes of interest. Also, the instrumentation is less expensive and easier to operate than mass spectrometers with a comparable resolving power.

Finally, the most attractive feature of this scheme is its excellent selectivity. It is virtually interference-free because each hyperfine structure has its own unique shape, within a narrow range of frequency. Since both resonance and non-resonance optogalvanic effects (OGE) can be readily observed, several transition lines are available from which to choose an excitation wavelength where spectral interference is minimal. Also it is important to note that optogalvanic signals resulting from resonance OGE are much stronger than those resulting from non-resonance OGE. Hence one can expect much better sensitivity for these transitions. We have demonstrated a fairly good sensitivity level for the Cu I 578.2 nm line, a non-resonance transition. Therefore, it is resonable to expect much better detection limits for elements with a resonance optical transition. In addition, selectivity and sensitivity can be further enhanced by using multiphoton optogalvanic detection schemes.

# CHAPTER IV. DOPPLER-FREE POLARIZATION SPECTROSCOPY FOR ELEMENTAL ANALYSIS AT TRACE CONCENTFATIONS

## Review

Trace-concentration elemental analysis has been performed most frequently by using one of the most sentitive analytical methods of absorption, emission or fluorescence spectrometry. The advent of lasers and their use as excitation light sources accelerated the progress for detection of extremely low concentrations of analyte samples. Laser-induced atomic fluorescence especially benefited from many advantages of lasers, such as high photon flux, narrow linewidth and monochromaticity. The sensitivity of this technique has been demonstrated for detection limit in the range 10 - 250 atoms/cm$^3$ (166-170), and even a single atom detection in the gas phase (171). The laser fluorescence method using atomic beam and photon-burst detection scheme yields not only high sensitivity (0.1 atom/cm$^3$) but also the Doppler-free linewidths (99). However, laser fluorescence analysis of elements in aqueous solutions, using continuous sample introduction scheme such as flame atomizer, yields detection limits much higher than those using free atoms in the gaseous phase (172 - 174). The main contributing factor for this is apparently the flame background noise resulting from the emission of flame molecular species such as OH, $C_2$, CH and CN. Other background noises include source light scattering by small unburnt particulates and atomic and molecular species, fluctuations of the flame optical density, and stray laser radiation. Various techniques, including gated detection (172,175,176), laser light amplitude modulation (177,178), background noise correction at nonresonant wavelength (179,180) and wavelength modulation (181) have been used to suppress background noise in fluorescence spectrometry.

In this chapter, we report the development of an unique analytical tool for trace-level elemental analysis based on polarization spectroscopy, where improved detectability of polarization rotation and excellent discrimination of flame emission background yield sensitivity level equal to or better than the fluorescence methods. In principle, scattered light and background emission should not contribute to the signal in polarization spectroscopy, and hence making it relatively interference free. Furthermore, the polarization spectroscopy provides Doppler-free information, and the resulting high spectral resolution offers enhanced selectivity and better suppression of spectral interference. Parts per trillion level detection of sodium and detection limit of 37 ppm for barium are demonstrated using this laser-induced polarization spectroscopic technique, while taking advantage of analytical flame as atomizer for convenient sample introduction.

Polarization spectroscopy (182) is related to saturation spectroscopy (183 - 185) but provides significantly higher sensitivity. The analyte sample in the atomizer is illuminated by circularly or linearly-polarized pump beam and a counter-propagating linearly-polarized probe beam of the same frequency (2 level system). An optical anisotropy, induced by the pump beam, is experienced by the weak probe beam when the two beams interact with the same atoms whose axial velocity is essentially zero. The polarization of the probe beam is affected by the anisotropic optical medium, and hence allowing the probe beam to pass through the initially cross-polarized analyzer. The Doppler-free polarization spectrum is conveniently collected by monitoring this probe signal with a photomultiplier tube while scanning the laser frequency across the center of the absorption line. Two different types of polarization spectra can be collected depending on whether the laser-induced dichroism or the birefringence is observed.

### Doppler-free laser-induced dichroism and birefringence

The phenomena of laser-induced dichroism and birefringence have been commonly observed in optical Kerr effect, Raman- induced Kerr effect (RIKE) (186 - 188) and polarization rotation experiments (189 - 191). Nonlinear susceptibility, induced by the interaction of two laser beams, results in Doppler-free absorption-coefficient anisotropy (dichroism) and refractive-index anisotropy (birefringence). These effects (182) are briefly reviewed here in order to assist the discussion of experimentally observed data later in this chapter.

For the polarization spectroscopy arrangement using a weak linearly-polarized probe beam and a circularly-polarized pump beam (essentially the RIKE setup), the pump beam induces different changes in absorption coefficient, $\Delta\alpha^+$ and $\Delta\alpha^-$ for the two circularly-polarized components of the probe beam (+ and - refer to the components of the probe beam rotating in the same and opposite directions, respectively, as the pump beam). Hence, the probe beam is elliptically polarized by the circular dichroism resulting from the difference $\Delta\alpha^+ - \Delta\alpha^-$ . Similarly, the difference in changes of refractive index $\Delta n^+ - \Delta n^-$ , induces the birefringence anisotropy and hence the rotation of polarization axis.

The Lorentzian-shaped dichroism curve $\Psi$ and the dispersion-shaped birefringence resonance curve $\Phi$ are related to each other by Kramers-Kronig relation (188, 192).

$$\Phi = -x\,\Psi \tag{39}$$

where

$$\Phi = (w/c)\ \Delta n^{\pm}\ L \tag{40}$$

$$\Psi = \Delta\alpha^{\pm}\ (L/2) \tag{41}$$

and L is the absorption path length, and x is the laser detuning from resonance frequency.

$$x = (w - w_0)/\ \Gamma \tag{42}$$

$$\text{where} \quad w_0 = 2\Pi\ \nu_0 \tag{43}$$

$\nu_0$ is the resonant frequency of a stationary atom and $\Gamma$ is the natural linewidth.

The Lorentzian-shaped absorption-change profile $\Delta\alpha^{\pm}$ is described as (182, 193),

$$\Delta\alpha^{+} = -(1/2)\ \alpha_0\ I\ /\ I_{sat}\ (1 + x^2) \qquad (44)$$

$$\Delta\alpha^{-} = d\ \Delta\alpha^{+} \qquad (45)$$

where $\alpha_0$ is the unsaturated background absorption, I is the pump beam intensity and $I_{sat}$ the saturation parameter. The parameter d is dependent on decay rates and angular momentum numbers, J' and J, of the lower and upper levels of the transition respectively. It measures the strength of dichroism and birefringence anisotropy.

From equations 39, 40 and 41, the refractive-index change $\Delta n^{\pm}$ is related to $\Delta\alpha^{\pm}$ as

$$\Delta n^{\pm} = -(1/2)\ x\ (c/v)\ \Delta\alpha^{\pm} \qquad (46)$$

By combining the contributions of both anisotropies, the light intensity passing through the analyzer is described by (182),

$$I = I_0[\theta^2 + \theta(s/2)x/(1+x^2) + (s/4)^2/(1+x^2)] \qquad (47)$$

where $$s = -(1/2)(1-d)\ \alpha_0\ L\ I/I_{sat} \qquad (48)$$

and $I_0$ is the incident probe beam intensity.

When $\theta$ approaches zero (i.e. virtually 100% cross-polarized analyzer), the last term in equation 47 yields a pure Lorentzian-shaped resonance curve. As $\theta$ is increased by rotating the analyzer in either direction, both dichroism and birefringence anisotropies contribute the shape of the curve. When the analyzer is rotated far enough so that s is insignificant compared to $\theta$, the last term in equation 47 becomes negligible, and hence a dispersion-shaped resonance curve resulting from the birefringent polarization rotation is observed. Experimental observation of these effects will be discussed later in the chapter.

The angular-momentum dependent d parameter measures the difference in relative anisotropic effects of the two counter-rotating components of the probe beam, and hence plays a major role in determining the laser-induced dichroism and birefringence in atomic lines. More detailed discussion of the J dependence and other calculations of third-order nonlinear susceptibilities based on the Zeeman laser perturbation theory are referred to some other reports (194 - 197).

## Experimental

### Analysis of Na D1 line

A schematic diagram of the experimental arrangement for Doppler-free polarization spectroscopy is shown in Figure 20. A Control Laser Model 554A argon ion laser (Orlando, FL) is used to pump a Specta-Physics Model 380A cw ring dye laser (Mountain View, CA). The ring dye laser is passively stabilized to provide single-frequency radiation (40 MHz jitter peak-to-peak) which can be electronically scanned over 30 GHz with selectable starting frequency and scanning rate. Rhodamine 590 dye (Exciton Chemical Co., Dayton, OH) is used in the ring dye laser to obtain the output frequency covering the Na *D* lines. A 1/4-in thick beam splitter is used to distribute the dye laser beam into three directions. One of the two weak beams (5% each) is sent to a Burleigh Instruments Model WA-20 wavemeter (Fishers, NY) for laser frequency calibration. The other weak beam is sent through a polarizer and used as the probe beam. The third beam is used as the pump beam and positioned to counter-propagate the probe beam. A pair of Glan-Thompson prisms (Karl Lambrecht Corp., Chicago, IL, Model MGT-25-E8-90, 8-mm aperture) serve as the polarizer and the analyzer. The

Figure 20. Experimental arrangement for Doppler-free polarization spectroscopy. Optical paths are shown as broken lines and electrical connections are shown as solid lines

A, analyzer; AL, argon ion laser; AM, nanoammeter; B, slot burner; BS, beam splitter; F, filter; HV, high voltage Op Amp; L, lens; LA, lock-in amplifier; LM, light modulator; LT, light trap; O, oscilloscope; P, polarizer; PDP 11, computer; PH, pin-hole aperture; PMT, photomultiplier tube; R, Fresnel rhomb; RE, chart recorder; V, voltmeter; W, wavemeter; WG, waveform generator

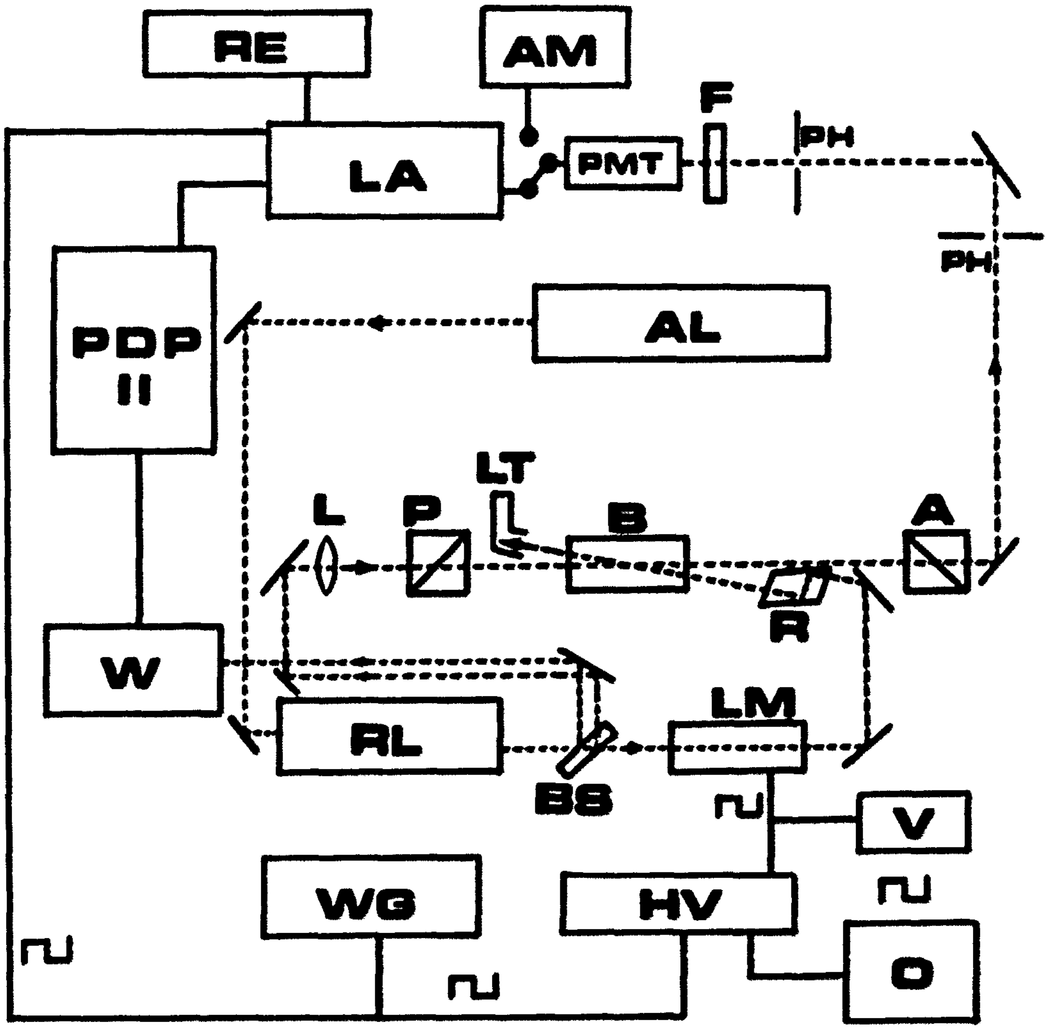
RE
AM
F
PH
LA
PMT
PH
PDP
II
AL
LT
L
P
B
A
R
W
RL
LM
BS
V
WG
HV
O

analyzer is mounted in an Aerotech Inc. Model ATS-301R rotational stage (Pittsburgh, PA) with a resolution of $10^{-3}$ degree, and the polarizer is mounted in a home-made aluminum mount. The prisms are positioned 60-cm apart on a Newport Research Corp. Model RS-410-8 optical table (Fountain Valley, CA). A 6-cm long Varian Techtron slot burner (Palo Alto, CA), mounted between the prisms, provides a laminar flame of acetylene and air. Rotameter type flow meters are used to measure the flow rates of both air and acetylene. A 25-mm aperture Fresnel rhomb (Karl Lambrecht Corp., Chicago, IL, Model FR4-25-580) is used to produce circularly-polarized pump beam from the linearly-polarized dye laser beam. A 1-m focal length lens is used to collimate the probe beam through the polarizer, the analytical flame and the analyzer. The probe beam and the counter-propagating pump beam are aligned to cross each other at a few milimeter above the center of the slot burner, with a cross angle as small as possible. The small collimated probe beam is completely engulfed within the pump beam volume, all along the length of the flame. A light trap catches the pump beam exiting the flame to prevent it from illuminating the polarizer mount and sending off undesirable scattered light. A few apertures are used along the optical path between the analyzer and the photomultiplier tube to reduce the background light. Probe light is detected, after passing through a line filter centered around 590.0 nm, by a Hamamatsu Corp. Model R928 photomultiplier tube (Middlesex, NJ) operating at 900V supplied by a Cosmic Radiation Labs Inc. Model 1001B Spectrastat high voltage power supply (Bellport, NY). The output of the photomultiplier tube is monitored by a Keithley Model 160B nanoammeter (Cleveland, OH) for the optimization of extinction ratio by manipulating the analyzer and the probe beam alignment between the two prisms. After disconnecting the nanoammeter, the photomultiplier tube signal is terminated in a 100 KΩ resistor, and the voltage is monitored by a Princeton Applied Research Model HR-8 lock-in amplifier (Princeton, NJ), where a 1-s time constant is used. The analog output of the lock-in amplifier is digitized via one of the ADC channels of the Laboratory Peripheral System (LPS-11) of a Digital Equipment Corp. PDP 11/10 minicomputer (Maynard, MA). The I/O port of the wavemeter is also interfaced to the minicomputer for digitization of the laser frequency values. The computer takes simultaneous readings of both polarization signal from the lock-in amplifier and the laser frequency value from the wavemeter every 0.5 sec, and the real-time spectrum is displayed on a Visual Technology Inc. Model 550 graphics terminal (Tewksbury, MA). The polarization spectrum is also recorded on a Houston

Instrument Model 5111-2 chart recorder (Bellaire, TX). All polarization spectra are collected using the scan range of 30 GHz and the scan time of 100 sec.

All sodium stock solutions are prepared by dissolving sodium hydroxide electrolytic pellets (Fisher Scientific Co., Fairlawn, NJ) in quadruply distilled deionized water, stored in polyethylene bottles and used the same day as prepared. Polarization spectra for Na D1 line are collected and stored by using the program PSNAD1.

## Polarization-modulated detection

The pump beam is polarization modulated by using a Lasermetrics Inc. Model 3030 electrooptic light modulator (Teaneck, NJ). The linearly-polarized ring dye laser beam is carefully directed through the 2.5-mm diameter aperture of the modulator so that at least 90% transmittance is obtained with minimum internal reflections and perfect output beam shape. By controlling the birefringence of the ADP crystal electronically, the plane of polarization can be rotated to any desired position. The voltage necessary to control the modulator is supplied by a Burleigh Instruments Inc. Model PZ-70 high voltage DC Op Amp (Fishers, NY), which is in turn driven by a Wavetek Model 162 waveform generator (San Diego, CA) using a 800 Hz square-wave function. The voltage amplitude of the square wave applied to the modulator is adjusted to produce half-wave retardation so that the plane of polarization of the linearly-polarized output beam is rotated through 90 degrees, back-and-forth repeatedly. This square-wave function from the wave generator is also sent to the lock-in amplifier as the reference signal. The output of the high voltage Op Amp is monitored by an oscilloscope to assure that the waveform is not distorted at the modulation frequency being used. The difference in modulation voltage, $\Delta V$, necessary to rotate the polarization through 90 degrees is determined to be 140V. The rotation of the polarization plane of pump beam is measured at a point just before it enters the flame using a dichroic Polaroid film. A voltmeter is used to monitor the modulator voltage. At normal operating modulation frequency only the average voltage of the square-wave function is displayed.

## Analysis of Ba 553.6-nm resonance line

The identical experimental arrangement as shown in Figure 20 is used for the analysis of barium. Rhodamine 560

Chloride dye (Exciton Chemical Co., Dayton, OH) is used instead in the ring dye laser to obtain about 250 mW of single-frequency 553.6-nm radiation, using 5 W of all-line pump power. An appropriate output mirror (M4), designed for this dye's output frequency range, is also installed in the ring dye laser. A line filter centered around 550.0 nm is used to filter the probe beam before entering the photomultiplier tube. All barium stock solutions are prepared by dissolving barium nitrate crystals (Mallinckrodt Chemical Works, NY, Analytical Reagent) in triply distilled deionized water and stored in polyethylene bottles.

## Results and Discussion

### Extinction ratio

The sensitivity of polarization spectroscopy depends significantly on the extinction ratio achieved between the polarizer and the analyzer prisms. Glan-Thompson prisms are amoung the best polarizers available commercially and offer extinction ratio of only $10^{6}$ . Moeller and Grieser reported that because of the imperfections in the volume of the calcite crystals, extinction ratios could vary from prism-to-prism and even from surface-to-surface of the same prism (198). Major contribution from crystal defects arise from the half of the analyzer facing toward the source and the half of the polarizer facing away from the source. Extinction ratio depends on the beam size and the beam positions through the prisms, because of the size and non-uniform distribution of these crystal imperfections. By confining the laser beam to certain selected, more uniform region of the crystals, an improved extinction ratio of $3x10^7$ was achieved (198). Yeung et al. obtained an improved extinction ratio of $10^{10}$ by selecting specific combinations of Glan-Thompson prisms as polarizer and analyzer, and specific combinations of entrance and exit surfaces for each prism (199). A pair of prisms selected by this procedure are used as polarizer and analyzer in this work. High extinction ratio is routinely reproducible by confining the lateral position of the beam at the selected region of each prism. Significant decrease in polarization signal could result by moving the lateral position of the laser beam only 1 mm away from the optimum spot of the crystal. To achieve optimum sensitivity, the polarizers are mounted rigidly and yet without any strain or distortion.

## Observation of dichroism and birefringence resonance curves

As described in equation 47, Lorentzian-shaped dichroism or dispersion-shaped birefringence resonance curves can be observed by rotating the analyzer and hence changing the $\theta$ value. When $\theta$ approaches zero (i.e. perfectly cross-polarized arrangement) the combined anisotropic effects yield a Lorentzian resonance curve. Figure 21 illustrates the experimental observation of equation 47 for a circularly-polarized pump beam and a lineraly-polarized probe beam. Twelve experimental polarization spectra with different $\theta$ values are collected while scanning the laser frequency across the Na D1 resonance line. Program PS3D displays all these Doppler-free dichroism ( $\theta = 0$) and birefringence ( $\theta \neq 0$) resonance curves with their corresponding laser frequency values. As the analyzer is rotated away from the perfectly cross-polarized arrangement to either direction (i.e. $\theta$ = + or - value), the first two terms in equation 47 become more significant. Hence, the dispersion-shaped resonance curves, produced by the birefringence polarization rotation, become more prominent. The observations are similar for a linearly-polarized pump

Figure 21. Experimental Doppler-free dichroism ( $\theta = 0$ ) and birefringence ($\theta \neq 0$) resonance curves for Na D1 line

12 polarization spectra with different $\theta$ values are displayed with their corresponding laser frequency values

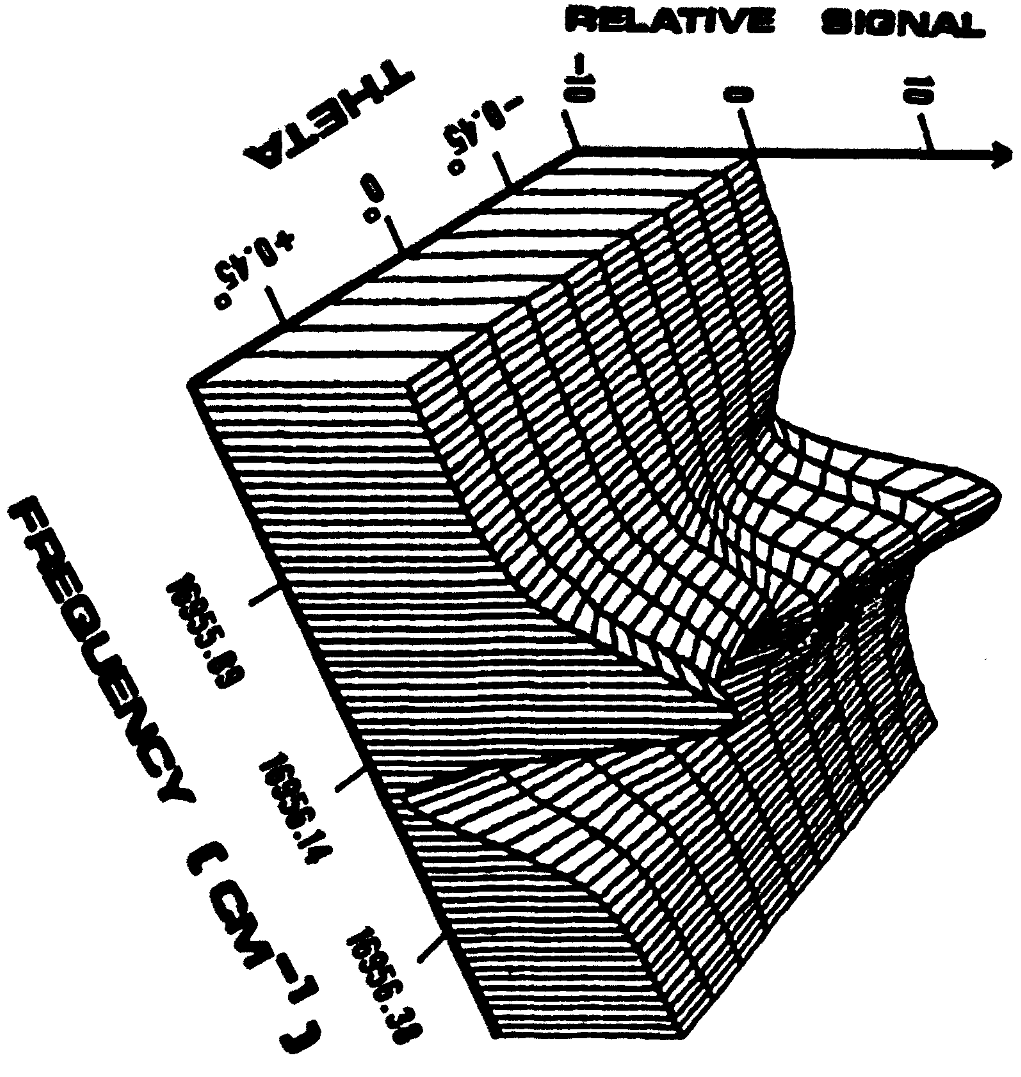
RELATIVE SIGNAL
-10
0
10
THETA
-0.45°
0°
+0.45°
FREQUENCY ( CM-1 )
16955.09
16956.14
16956.31

beam and a linearly-polarized probe beam. Although the dispersion-shaped signal is larger, the signal-to-noise ratio is actually poorer than the Lorentzian-shaped signal. Therefore, for the analysis of trace Na and Ba, and for the determination and optimization of sensitivity, the Lorentzian-shaped curve is used. The dispersion-shaped signal however is useful for the locking of the laser frequency to some resonance line, and for identifying some closely-spaced line components of a fine structure.

### Electrooptic light-modulator voltage

The magnitude of the polarization signal is also dependent on the angle between the probe and pump polarizations. The peak intensity of Lorentzian-shaped resonance curve varies with the position of pump polarization plane with respect to the probe plane. The on-resonance signal can be optimized by supplying an appropriate light-modulator voltage so that the pump polarization is rotated to its optimum position. Figure 22 illustrates this characteristic of the polarization signal by using a linearly-polarized pump beam and a counter-propagating linearly-polarized probe beam. In Figure 22 (a), the pump polarization is electronically controlled by the modulator voltage so that it makes an angle of 45 degree with respect to the probe field $E_{probe}$. The laser-induced anisotropy attenuates and phase shifts the component of $E_{probe}$ that is parallel to $E_{pump}$ and the one that is perpendicular to $E_{pump}$ differently. Consequently, the probe wave exiting the anisotropic medium has the direction $E_{signal}$ (188). Since the analyzer is polarized perpendicular to the initial probe field, the intensity reaching the detector, $E_{PMT}$, corresponds to the component of $E_{signal}$ perpendicular to $E_{probe}$. As shown in Figure 22 (a), (b) and (c) the magnitude and polarity of detected signal, $E_{PMT}$, can be altered by rotating the plane of pump polarization. The dependence of detected signal $E_{PMT}$ on pump polarization plane is experimentally observed as shown in Figure 23. Nine resonance profiles for Na D1 line are displayed with their corresponding modulator voltages used for rotating the plane of pump polarization to various positions. The high and low voltages refer to the two voltage levels of the square wave used for modulating the electrooptic crystal. A constant voltage gap $\Delta V$ of 140 V is used in each case. As described in Figure 22, the magnitude and polarity of experimental

Figure 22. Detected-signal dependence on pump polarization plane
Both linearly-polarized probe and pump beams are considered

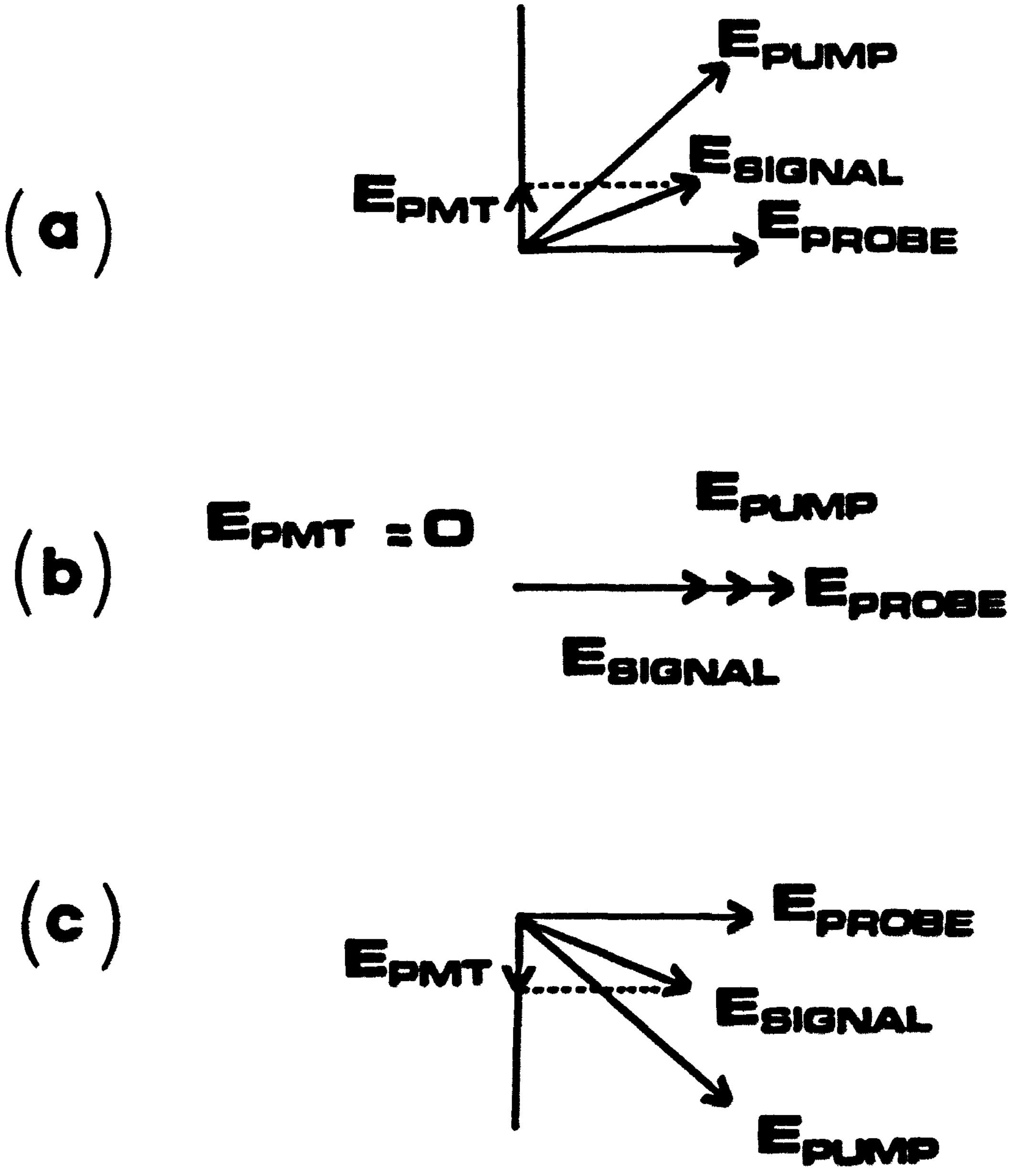
(a)
$E_{PUMP}$
$E_{SIGNAL}$
$E_{PMT}$
$E_{PROBE}$
(b)
$E_{PMT} = 0$
$E_{PUMP}$
$E_{PROBE}$
$E_{SIGNAL}$
(c)
$E_{PROBE}$
$E_{PMT}$
$E_{SIGNAL}$
$E_{PUMP}$

Figure 23. Experimental observation of signal dependence on pump polarization plane

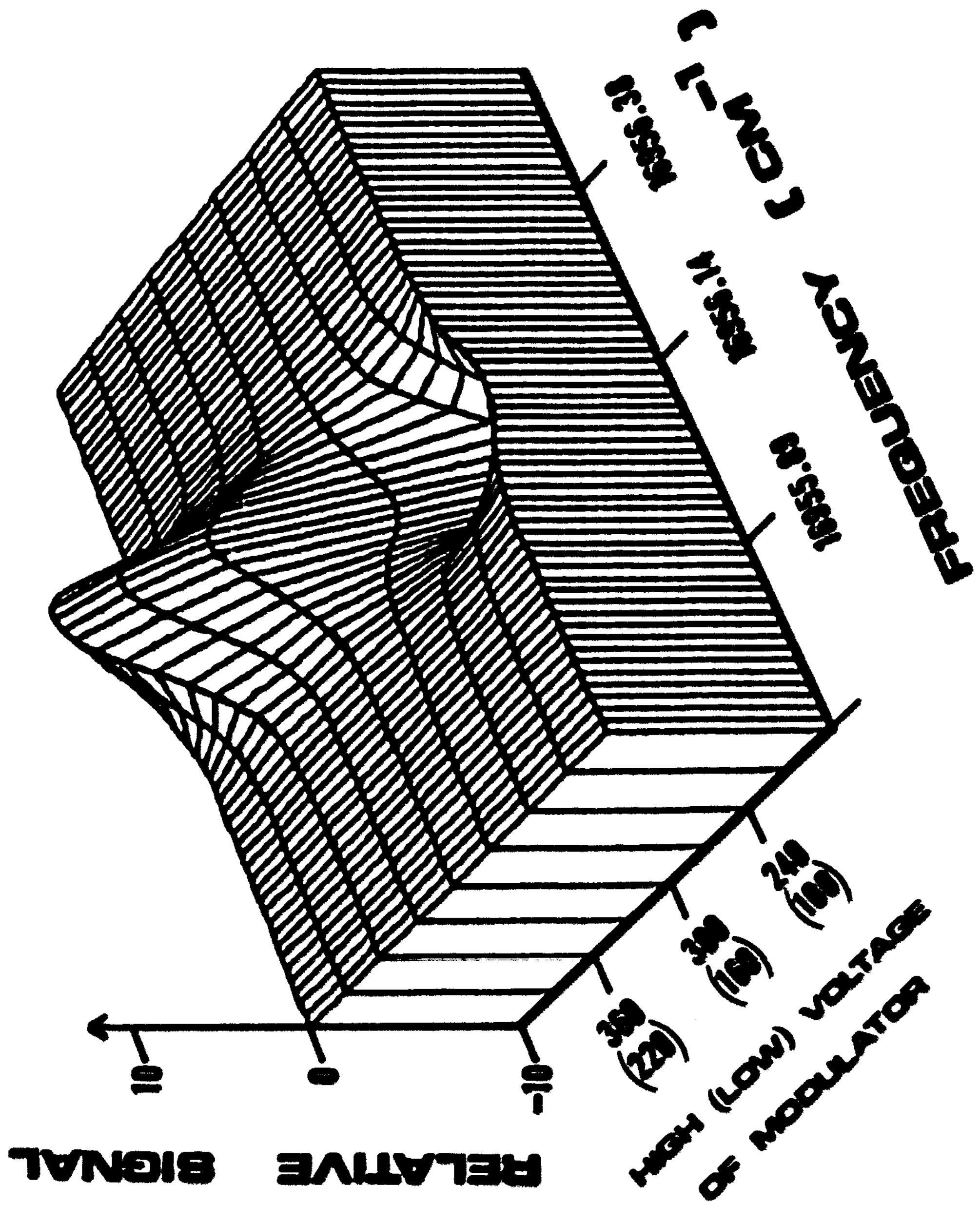
FREQUENCY ( CM-1 )
1955.31
1955.14
1955.00
RELATIVE SIGNAL
10
0
-10
HIGH (LOW) VOLTAGE OF MODULATOR
360 (220)
300 (180)
240 (180)

profiles vary with the position of pump polarization plane. A 90-degree rotation of pump polarization (an increase or decrease of 140 V in modulator voltage) results in the reversal of peak direction. Similar results are also observed by using a circularly-polarized pump beam. In this case, the laser-induced anisotropy affects the two circular components of $E_{probe}$ differently. $E_{sample}$ is elliptically polarized on-resonance, and the detected signal $E_{PMT}$ corresponds to the linear component of $E_{sample}$ which is perpendicular to $E_{probe}$ (188). Hence it is apparent that in polarization spectroscopy, the positions of probe and pump polarization, and the magnitude of the angle between them, are important parameters for the optimization of signal strength and sensitivity.

In addition to aligning the pump polarization at the optimum position, it is also important to modulate it a full 90 degree swing (i.e. square wave $\Delta V = 140$ V) at a selected frequency (800 Hz). Figure 24 shows the peak height dependence on the voltage gap $\Delta V$ between the high and low voltage levels of the square wave supplied to the modulator. As expected, the optimum signal strength is observed for $\Delta V = 140$ V which corresponds to 90 degree swing of pump polarization.

Figure 24. Signal dependence on voltage gap $\Delta V$ between the high and low voltage levels of the square wave supplied to the light modulator $\Delta V$ of 140 V corresponds to 90 degree rotation of pump polarization

(a) Constant low voltage of 220 V

(b) Constant high voltage of 360 V

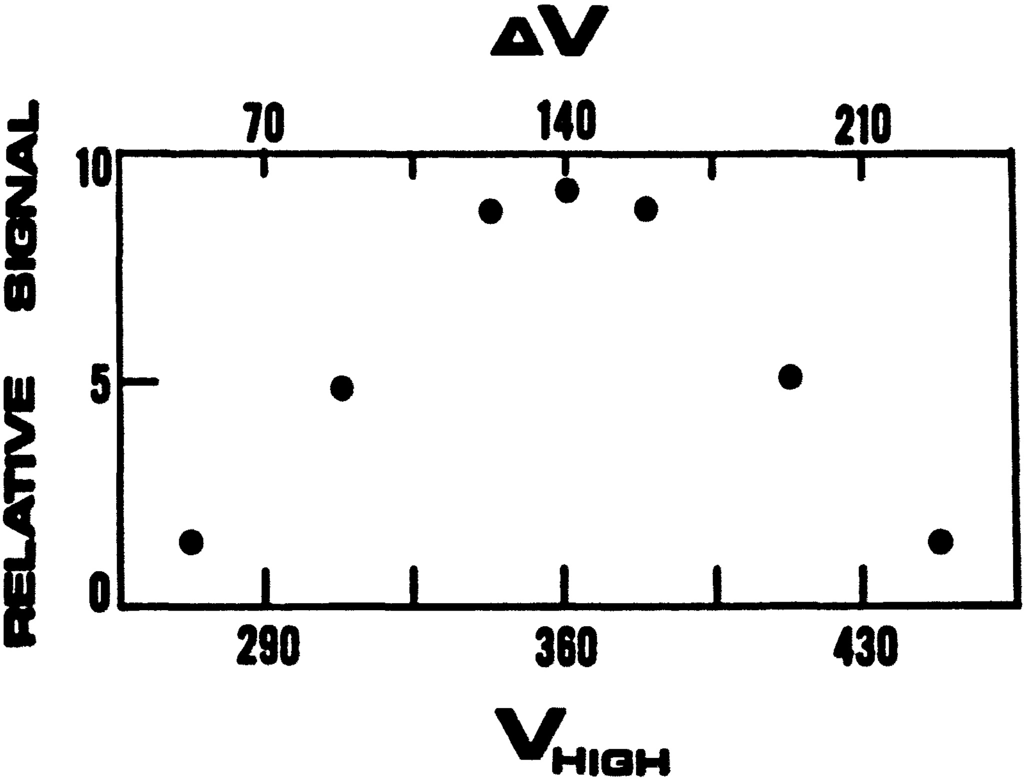
ΔV
70
140
210
RELATIVE SIGNAL
10
5
0
290
360
430
$V_{HIGH}$

(a)

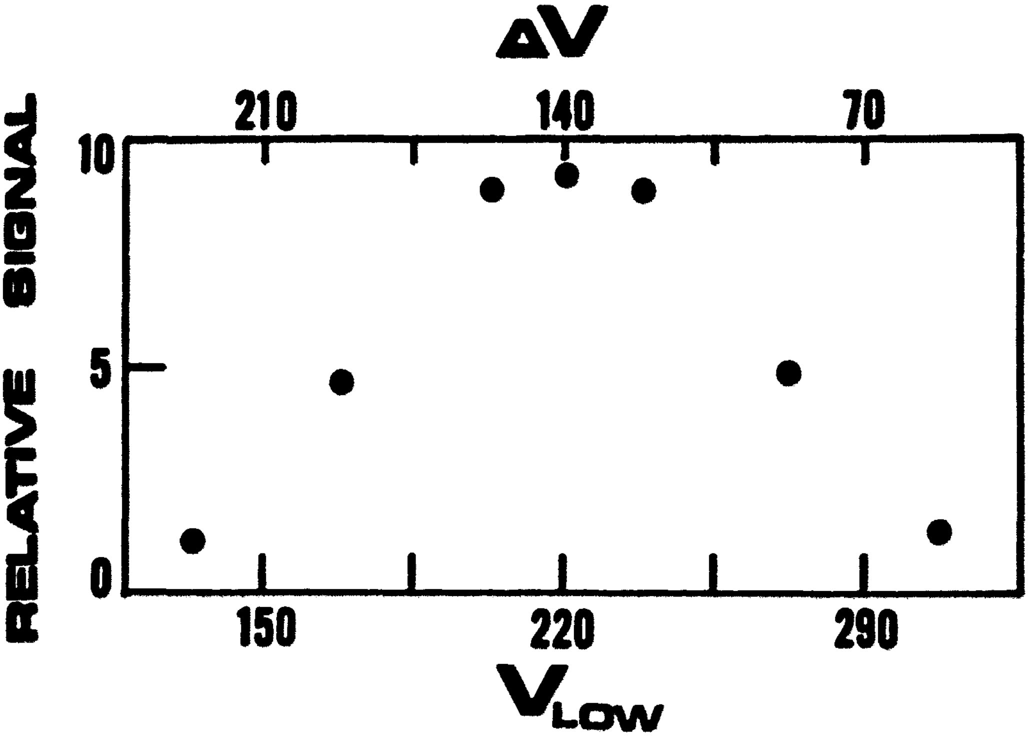
ΔV
210
140
70
RELATIVE SIGNAL
10
5
0
150
220
290
$V_{LOW}$

(b)

## Optimization of signal-to-noise ratio (S/N)

To achieve the highest S/N it is essential to obtain the optimum extinction ratio, pump-probe beam alignment inside the flame atomizer, and pump-probe polarization plane alignment as described above. Furthermore, the photomultiplier tube must be shielded from background light from all directions, including the intense scattered resonance light of the dye jet.

The S/N improvement of polarization-modulated detection (PMD) over amplitude-modulated detection (AMD) is determined to be a factor of at least 5. The amplitude modulation is done by using a mechanical chopper while maintaining the same modulation frequency and positions of pump-probe polarization planes as those of the PMD scheme. The S/N advantage of the PMD scheme apparently results from the fact that when polarization is modulated, the background light intensity is not modulated. For the AMD scheme, however, the lock-in amplifier "sees" the background light only during the half-cycle when the beam is unblocked. Also for the PMD scheme, the average pump power is increased by a factor of 2 because of the lack of an "off" half-cycle. The gain through PMD should be even more in highly luminous atom sources or those with significant particulate scattering. The signal-to-noise ratios of PMD scheme are also compared using various modulation frequency values ranging from 300 to 2 KHz. Though it seems to show a slight trend of S/N improvement as the frequency is gradually increased from 300 Hz, no significant difference is observed for the frequency range of 1 - 2 KHz. The major contributing factor for this is the distortion of square-wave voltage function supplied to the light modulator at high frequency, since the Burleigh HV Op Amp does not have the adequate speed required. Thus, 800 Hz is selected as the best compromising modulator frequency for the HV power supply used. The Model 481B scanning electronics unit of the ring dye laser uses a 2 KHz oscillator to drive a high voltage amplifier for generating 2 KHz waveforms, which are used in the etalon lock loop operation. Thus, it is also important not to use any harmonic frequencies of 2 KHz as the modulating frequency for the lock-in amplifier. Comparisons of polarization signals at various experimental conditions are done by using the peak intensities of Lorentzian resonance curves or by simply monitoring the on-resonance signals while locking the laser frequency at the center of the Doppler-broadened absorption line. The line center frequencies measured by the wavemeter in vacuum wavenumbers are 16973.330 $cm^{-1}$ for Na D1 line, 16956.120 $cm^{-1}$ for Na D2 line and 18060.100 $cm^{-1}$ for Ba resonance line. No significant difference in sensitivity or other characteristics of polarization spectroscopy is observed for the Na D1 and D2 lines.

The sensitivity also depends on the region of the analytical flame being used. The pump and probe beam positions are optimized by monitoring the on-resonance signal while moving the analytical flame vertically. The optimum region of the flame is found to be at about 2 mm above the burner slot, which corresponds to the inner cone (or preheating zone) of the flame. In this region, the temperature is generally lower compared to the interconal zone just above it (200), however, the concentration of free radicals are extraordinarily high (201). Various flow rates of acetylene and air were also tested for the flame, and the ratio 1:6 (acetylene : air) was determined to yield the highest on-resonance signal. The analyte solution flow rate of 5 ml/min is also used.

The polarization signal should depend on the square of the laser power in this experimental arrangement. For the same induced polarization rotation, a higher laser power will produce a higher transmitted intensity, as predicted by equation 47. But, a higher laser power induces a larger rotation, according to equation 44. The net effect is a quadratic power dependence. Figures 25 and 26 show this effect for sodium and barium respectively. The laser power values in Figures 25 and 26 refer to the power of the total dye beam

Figure 25. Squared laser power dependence of Doppler-free polarization signal for sodium

(Circularly-polarized pump beam and linearly-polarized probe beam are used)

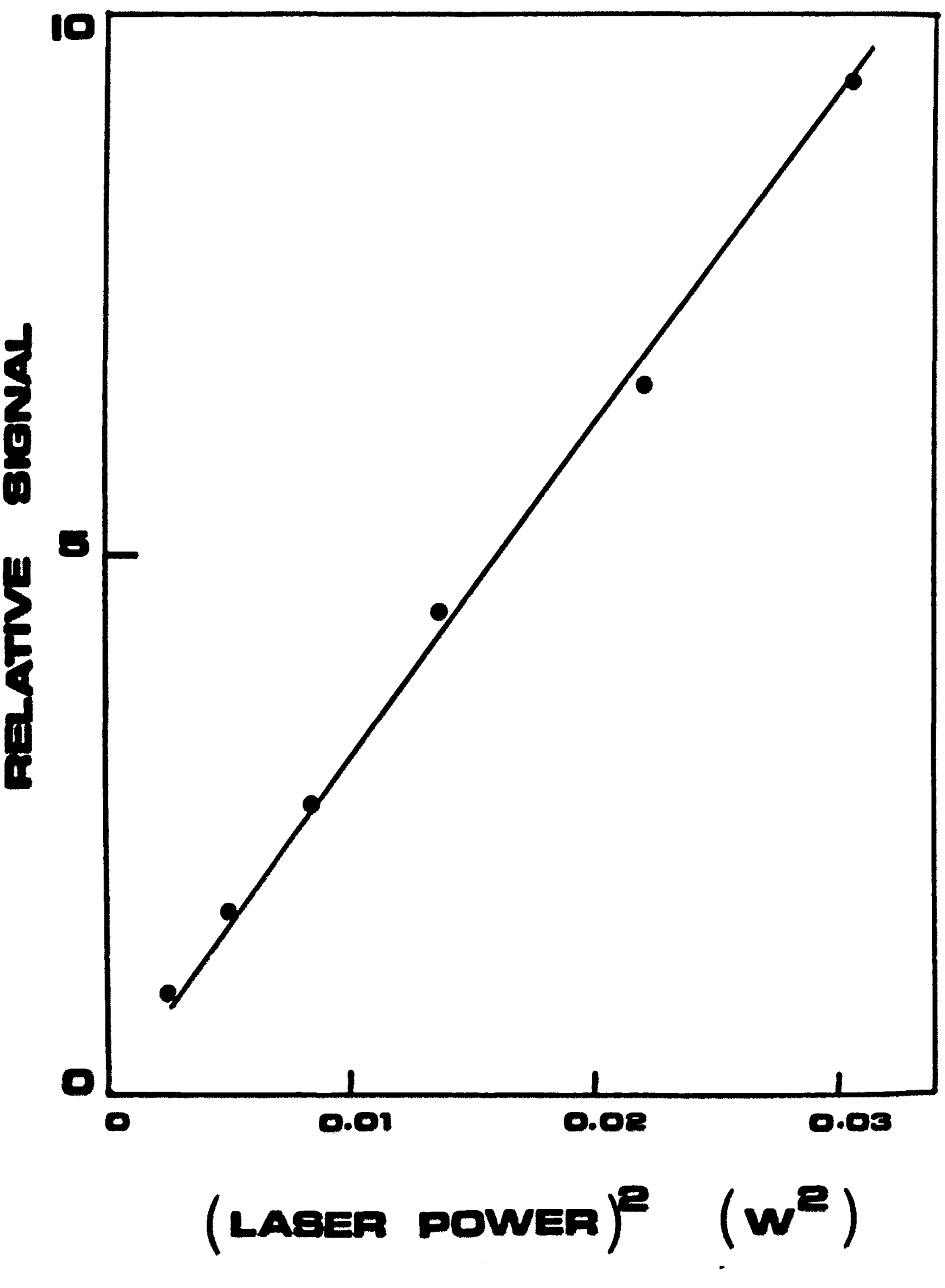
RELATIVE SIGNAL
10
5
0
0
0.01
0.02
0.03
(LASER POWER)$^2$ (W$^2$)

Figure 26. Squared laser power dependence of Doppler-free polarization signal for barium

(Circularly-polarized pump beam and linearly-polarized probe beam are used)

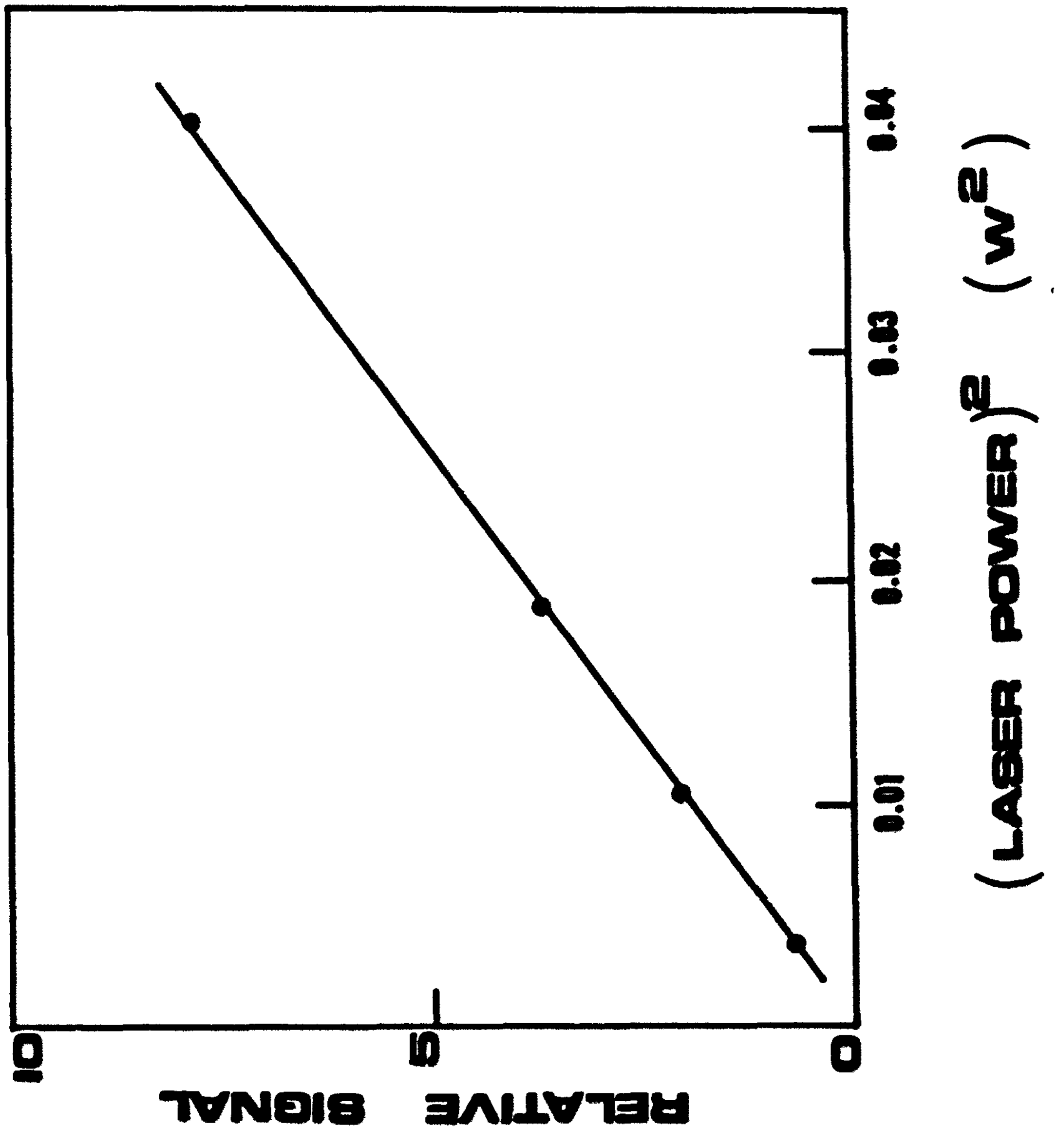
RELATIVE SIGNAL
0
5
10
(LASER POWER)$^2$ (W$^2$)
0.01
0.02
0.03
0.04

measured before it is divided into the weak beams (5% each) and the strong beam by the beam splitter. Laser power dependence is studied by using relatively higher concentrations of analyte solutions (10 ppb for Na and 1 ppm for Ba). Polarization signal is observed even at the lowest dye laser power that could be maintained with lasing stability (i.e. less than 10 mW). Quadratic response is observed for the lowest to the highest obtainable power of the dye laser.

Linear response of polarization signal to concentration is achieved for the three orders of magnitude in the barium concentration tested. This is illustrated in Figure 27 where peak heights normalized by laser power are plotted with their corresponding concentrations. Similar quadratic dependence on laser power and linear dependence on concentrations are observed for both linearly and circularly-polarized pump beams.

The improved detectability of polarization rotation (better polarizers) and the excellent suppression of flame emission background (polarization modulation) enable this technique to achieve detection limits of 30 ppt (trillion) of sodium and 37 ppb of barium. (The detection limit is defined as the concentration yielding a signal equal to twice the peak-to-peak noise of the baseline or background signal.) The potential sensitivity for sodium exceeds the ability of the researcher to avoid contamination during the analysis or

Figure 27. Linear response of polarization signal to barium concentration

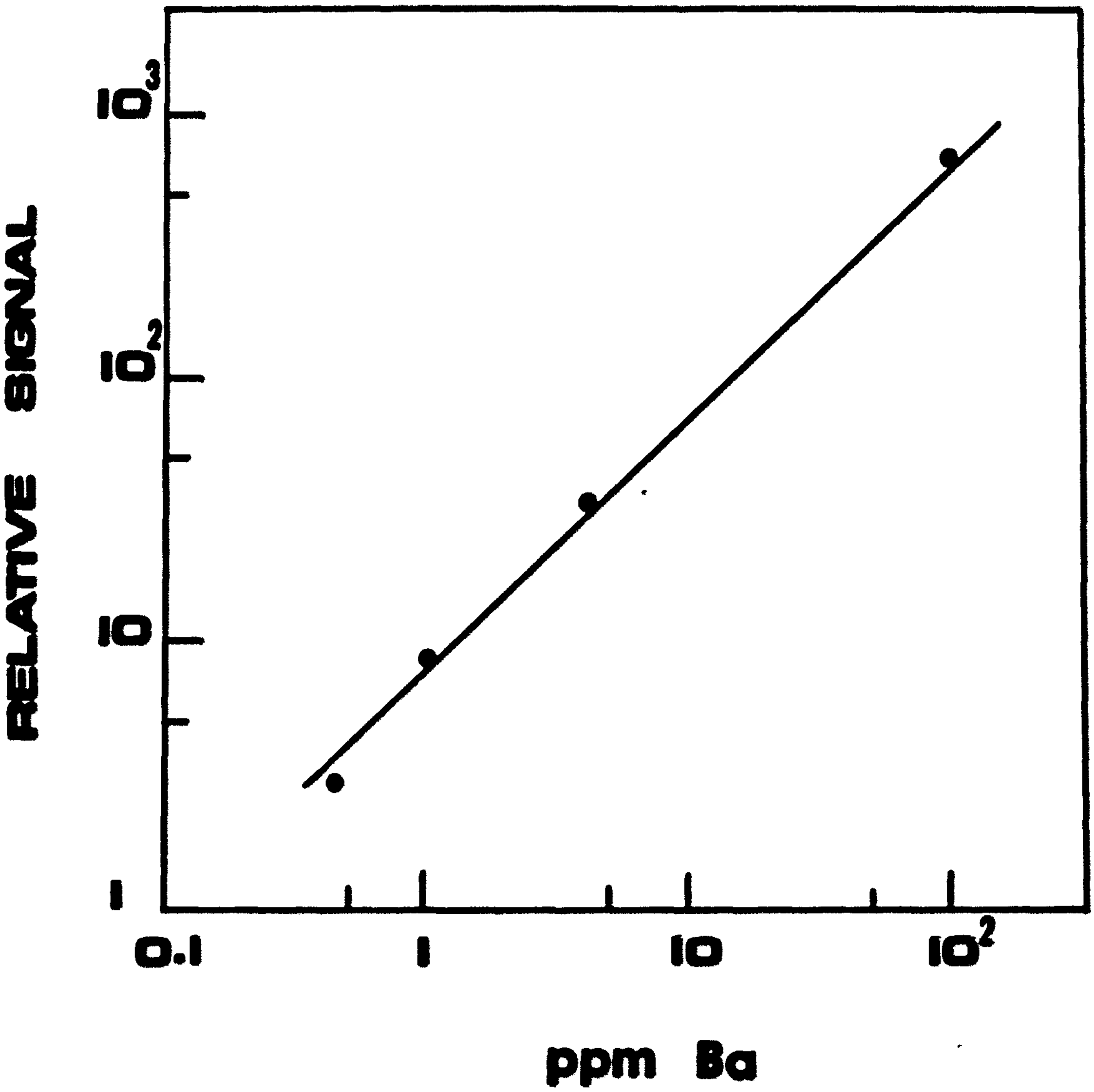
RELATIVE SIGNAL
10³
10²
10
1
0.1
1
10
10²
ppm Ba

to simply find the water pure enough to prepare the trace sodium solutions. The quadruply distilled deionized water used in this work is determined to contain 5 ppb of sodium. A strong polarization signal can be observed just by aspirating this "blank" water into the flame while scanning the laser frequency across the Na D1 line. Preparation of trace barium solutions is easier since barium is relatively less abundant in the environment. All quantitative measurements are done by first aspirating the less concentrated solutions to avoid contamination of the slot burner. The sensitivity of this polarization spectroscopic method is actually competitive with other highly sensitive laser spectroscopic techniques, such as the atomic fluorescence spectrometry (AFS). As shown in Table 10, the detection limit of this method is competitive with those of the wavelength-modulated laser AFS using flame atomizer (202) and also the AFS using the more efficient graphite atomizer (174). Relative detection limits obtained by different techniques can only be compared roughly because of the many differences in experimental variables and instruments used. In any case, we have developed and demonstrated the Doppler-free polarization spectroscopy to be one of the most sensitive analytical methods. It is expected that lower limits of detection can be achieved by improving many experimental variables such as using more

Table 10. Relative detection limits obtained by polarization spectroscopic method and by atomic fluorescence spectrometry (AFS)[a]

| | Detection limit ( ng/ml ) | Ref. |
|---|---|---|
| (1) For Na | | |
| This work | 0.03 | |
| Laser AFS (Graphite Atomizer) | 0.02 | 174 |
| Laser AFS | 0.1 | 173 |
| Continuum lamp-source AFS | 8 | 203 |
| Line-source AFS | 100,000 | 203 |
| (2) For Ba | | |
| This work | 37 | |
| Wavelength-modulated laser AFS | 20 | 202 |
| Laser AFS | 100 | 203 |
| Pulsed hollow-cathode lamp AFS | 200 | 203 |
| Amplitude-modulated laser AFS | 300 | 202 |

[a] All methods used flame atomizers unless otherwise indicated.

efficient optical filters and photodetectors, higher laser power, and higher modulation frequencies where flame fluctuations and electronic noises of the laser system can be further minimized. Ultimately, detectability in polarization spectroscopy will be limited by the signal level when compared to AFS. But, for highly luminous atom sources or those with substantial particulate scattering, the lower noise level in polarization spectroscopy is advantageous.

In addition to its excellent sensitivity, the polarization spectroscopic method offers another advantage: the Doppler-free information. It is especially useful when using atomizers which have relatively higher temperatures. The analytical flame here provides a Lorentzian linewidth (FWHM) of 0.14 $cm^{-1}$ (for Ba 553.6 nm line). It is still narrow enough that this technique can be used for isotope ratio analysis (as described in Chapter III) for some hyperfine structures (204). The high spectral resolution also provides excellent selectivity and minimum spectral interference.

## Conclusions

We have demonstrated that the Doppler-free polarization spectroscopy can be used for trace-concentration elemental analysis, and the sensitivity is competitive with other sensitive laser techniques including the atomic fluorescence methods. Improved detectability of polarization rotation and excellent suppression of flame background noise enable this method to achieve the detection limits of parts per trillion levels of sodium and concentration of 37 ppb of barium, while taking advantage of the convenient and fast analyte introduction of analytical flame. Furthermore, since it provides Doppler-free information, the spectral resolution is suitable for isotope ratio analysis. Its narrow experimental linewidth also offers excellent selectivity and minimum spectral interference.

# REFERENCES

1. Green, R. B.; Keller, R. A.; Luther, G. G.; Schenck, P. K.; Travis, J. C. Appl. Phys. Lett. 1976, 29, 727.

2. Goldsmith, J. E. M.; Lawler, J. E. Contemp. Phys. 1981, 22, 235.

3. Penning, F. M. Physica 1928, 8, 137.

4. Green, R. B.; Keller, R. A.; Luther, G. G.; Schenck, P. K.; Travis, J. C. J. Am. Chem. Soc. 1976, 98, 8517.

5. Turk, G. C.; Travis, J. C.; DeVoe, J. R.; O'Haver, T. C. Anal. Chem. 1978, 50, 817.

6. King, D. S.; Schenck, P. K. Laser Focus 1978 March, 50.

7. Nippoldt, M. A.; Green, R. B. Appl. Opt. 1981, 20, 3206.

8. King, D. S.; Schenck, P. K.; Smyth, K. C.; Travis, J. C. Appl. Opt. 1977, 16, 2617.

9. Dovichi, N. J.; Moore, D. S.; Keller, R. A. Appl. Opt. 1982, 21, 1468.

10. Beenen, G. J.; Piepmeier, E. H. Anal. Chem. 1981, 53, 239.

11. Green, R. B.; Keller, R. A.; Luther, G. G.; Schenck, P. K.; Travis, J. C. IEEE J. Quantum Elect. QE-13 1977, 63.

12. Schenck, P. K.; Smyth, K. C. J. Opt. Soc. Am. 1978, 68, 626.

13. Keller, R. A.; Engleman, R. Jr.; Zalewski, E. F. J. Opt. Soc. Am. 1979, 69, 738.

14. Beenen, G. J.; Lessard, B. P.; Piepmeier, E. H. Anal. Chem. 1979, 51, 1721.

15. Dreze, C.; Demers, Y.; Gagne, J. M. J. Opt. Soc. Am. 1982, 72, 912.

16. Shuker, R.; Ben-Amar, A.; Erez, G. Optics Commun. 1982, 42, 29.

17. Smyth, K. C.; Schenck, P. K. Chem. Phys. Lett. 1978, 55, 466.

18. Smyth, K. C.; Keller, R. A.; Crim, F. F. Chem. Phys. Lett. 1978, 55, 473.

19. Zelewski, E. F.; Keller, R. A.; Englemam, R. Jr. J. Chem. Phys. 1979, 70, 1015.

20. Begemann, M. H.; Saykally, R. J. Optics Commun. 1982, 40, 277.

21. Bridges, W. B. J. Opt. Soc. Am. 1978, 68, 352.

22. Kushner, M. J. Appl. Opt. 1983, 22, 1970.

23. Webster, C. R.; Menzies, R. T. J. Chem. Phys. 1983, 78, 2121.

24. Webster, C. R. Appl. Opt. 1982, 21, 2298.

25. Webster, C. R.; Rettner, C. T. Laser Focus 1983, 19, 41.

26. Walkup, R.; Dreyfus, R. W.; Avouris, P. Phys. Rev. Lett. 1983, 50, 1846.

27. Feldmann, D. Optics Commun. 1979, 29, 67.

28. Ausschnitt, C. P.; Bjorklund, G. C.; Freeman, R. R. Appl. Phys. Lett. 1978, 33, 851.

29. Shuker, R.; Ben-Amar, A.; Erez, G. Optics Commun. 1981, 38, 51.

30. Wakata, H.; Saikan, S.; Kimura, M. Optics Commun. 1981, 38, 271.

31. Cornelissen, H. J.; Burgmans, A. L. J. Optics Commun. 1982, 41, 187.

32. Lawler, J. E.; Ferguson, A. I.; Goldsmith, J. E. M.; Jackson, D. J.; Schawlow, A. L. Phys. Rev. Lett. 1979 42, 1046.

33. Lyons, D. R.; Schawlow, A. L.; Yan G-Y. Optics Commun. 1981, 38, 35.

34. Siegel, A.; Lawler, J. E.; Couillaud, B.; Hansch, T. W. Phys. Rev. A 1981, 23, 2457.

35. Suzuki, T. Optics Commun. 1981, 38, 364.

36. Apel, C. T.; Keller, R. A.; Zalewski, E. F.; Engleman, R. Jr. Appl. Opt. 1982, 21, 1465.

37. Winefordner, J. D.; Svoboda, V.; Cline, L. J. Crit. Rev. Anal. Chem. 1970, 1, 233.

38. Liddell, P.R.; Anal. Chem. 1976, 48, 1931.

39. Bower, n. W.; Ingle, J. D. Jr. Anal. Chem. 1977, 49, 574.

40. Green, R. B.; Keller, R. A.; Schenck, P. K.; Travis, J. C.; Luther, G. G. J. Am. Chem. Soc. 1976, 98, 8517.

41. Travis, J. C.; Schenck, P. K.; Turk, G. C.; Mallard, W. G. Anal. Chem. 1979, 51, 1516.

42. Turk, G. C.; Travis, J. C.; DeVoe, J. R.; O'Haver, T. C. Anal. Chem. 1979, 51, 1890.

43. Turk, G. C. Anal. Chem. 1981, 53, 1187.

44. Havrilla, G. J.; Weeks, S. J.; Travis, J. C. Anal. Chem. 1982, 54, 2566.

45. Nippoldt, M. A.; Green, R. B. Anal. Chem. 1983, 55, 554.

46. Schenck, P. K.; Mallard, W. G.; Travis, J. C.; Smyth, K. C. J. Chem. Phys. 1978, 69, 5147.

47. Turk, G. C.; Mallard, W. G.; Schenck, P. K.; Smyth, K. C. Anal. Chem. 1979, 51, 2408.

48. Turk, G. C.; DeVoe, J. R.; Travis, J. C. Anal. Chem. 1982, 54, 643.

49. Zalewski, E. F.; Keller, R. A.; Apel, C. T. Appl. Opt. 1981, 20, 1584.

50. Travis, J. C.; Turk, G. C.; Green, R. B. Anal. Chem. 1982, 54, 1006 A.

51. Foote, P. D.; Mohler, F. L. Phys. Rev. 1925, 26, 195.

52. Mohler, F. L.; Beockner, C. J. Res. Natl. Bur. Stds. 1930, 5, 51.

53. Smyth, K. C.; Bentz, B. L.; Bruhn, C. G.; Harrison,

W. W. J. Am. Chem. Soc. 1979, 101, 798.

54. Demtroder, W. "Laser Spectroscopy" Springer-Verlag, Berlin, 1981.

55. Shimoda, K. "High-Resolution Laser Spectroscopy" Springer-Verlag, Berlin, 1976.

56. Boutilier, G. P.; Blackburn, M. B.; Mermet, J. M.; Weeks, S. J.; Haraguchi, H.; Winefordner, J. D.; Omenetto, N. Appl. Opt. 1978, 17, 2291.

57. Smits, R. M. M.; Prins, M. Physica 1975, 80C, 571.

58. Hieftje, G. M.; Travis, J. C.; Lytle, F. E.; Eds. "Lasers in Chemical Analysis" Humana Press, Clifton, NJ, 1981.

59. Lawton, J.; Weinberd, F. J. "Electrical Aspects of Combustion" Oxford University Press, London, 1969.

60. Merton, T. R. Nature 1919, 104, 406.

61. Bohr, N. Nature 1922, 109, 746.

62. Schuler, H. Z. Physik 1930, 59, 150.

63. Murakawa, K.; Suwa, S. J. Phys. Soc. Jap. 1950, 5, 382.

64. Brix, P.; Buttlar, H.; Houtermans, F. G.; Kopfermann, H. Z. Physik 1952, 133, 192.

65. Steudel, A. Z. Physik 1952, 132, 429.

66. Murakawa, K. J. Phys. Soc. Jap. 1953, 8, 382.

67. Murakawa, K. J. Phys. Soc. Jap. 1954, 9, 876.

68. Kuhn, H. G.; Turner, R. Proc. Roy. Soc. A 1961, 265, 39.

69. Stacey, D. N. Proc. Roy. Soc. A 1964, 280, 439.

70. Fisher, R. A. Reviews of Modern Physics 1942, 14, 79.

71. Crawford, M. F.; Kelly, F. M.; Schawlow, A. L.; Gray, W. M. Phys. Rev. 1949, 76, 1527.

72. Kelly, F. M. Can. J. Phys. 1957, 35, 1220.

73. Gustafsson, M; Lindgren, I.; Lindgren, J.; Rosen, A.; Rubinsztein, H. *Phys. Lett.* 1977, 72B, 166.

74. Hindmarsh, W. R.; Kuhn, H. *Proc. Phys. Soc. A* London, 1955, 68, 433.

75. Geiger, F. E. Jr. *J. Opt. Soc. Am.* 1958, 48, 302.

76. Arroe, H.; Cornwall, J. M. *Phys. Rev.* 1960, 117, 748.

77. Hughes, R. H. *Phys. Rev.* 1961, 121, 499.

78. Finckh, E.; Steudel, A. *Z. Physik* 1955, 141, 19.

79. Schroeder, D. J.; Mack, J. E. *Phys. Rev.* 1961, 121, 1726.

80. Edwin, R. P.; King, W. H. *J. Phys. B* 1969, 2, 260.

81. Bruch, R.; Heilig, K.; Kaletta, D.; Steudel, A.; Wendlandt, D. *J. Phys. Paris* 1969, Suppl. No. 1, 30, C1.

82. Epstein, G. L.; Davis, S. P. *Phys. Rev. A* 1971, 4, 464.

83. Heilig, K. *Z. Physik* 1961, 161, 252.

84. Heilig, K.; Schmitz, K.; Steudel, A. *Z. Physik* 1963, 176, 120.

85. Hansen, J. E.; Steudel, A.; Walther, H. *Z. Physik* 1967, 203, 296.

86. King, W. H.; Steudel, A.; Wilson, M. *Z. Physik* 1973, 265, 207.

87. Fischer, W.; Hartmann, M.; Huhnermann, H.; Vogg, H. *Z. Physik* 1974, 267, 209.

88. Brimicombe, M. S. W. M.; Stacey, D. N.; Stacey, V.; Huhnermann, H.; Menzel, N. *Proc. Roy. Soc. London A* 1976, 352, 141.

89. Lewis, E. L. *Am. J. Phys.* 1977, 45, 38.

90. Ahmad, S. A.; Saksena, G. D. *Spectrochim. Acta* 1981, 36B, 943.

91. Manning, T. E.; Anderson, C. E.; Watson, W. W. *Phys. Rev.* 1950, 78, 417.

92. Hately, G. F.; Littlefield, T. A. *J. Opt. Soc. Am.* 1958, 48, 851.

93. Bishop, D. C.; King, W. H. *J. Phys. B* 1971, 4, 1798.

94. Moscatelli, F. A.; Redi, O.; Schonberger, P.; Stroke, H. H.; Wiggins, R. L. *J. Opt. Soc. Am.* 1982, 72, 918.

95. Cabezas, A. Y.; Lindgren, I.; Marrus, R. *Phys. Rev.* 1961, 122, 1796.

96. Moskowitz, P. A.; Liu, C. H.; Fulhop, G. F.; Stroke, H. H. *Phys. Rev.* 1971, C4, 620.

97. Covey, R. L.; Davis, S. P. *Phys. Rev.* 1972, C5, 1397.

98. Griffith, J. A. R.; Isaak, G. R.; New, R.; Ralls, M. P.; Zyl, C. P. V. *J. Phys. B* 1977, 10, L91.

99. Lewis, D. A.; Tonn, J. F.; Kaufman, S. L.; Greenlees, G. W. *Phys. Rev. A* 1979, 19, 1580.

100. Clark, D. L.; Cage, M. E.: Lewis, D. A.; Greenlees, G. W. *Phys. Rev. A* 1979, 20, 239.

101. Gerstenberger, D. C.; Latush, E. L.; Collins, G. J. *Opt. Commun.* 1979, 31, 28.

102. Timmermann, A. *Z. Physik A* 1980, 296, 93.

103. Palmer, C. W. P.; Baird, P. E. G.; Nicol, J. L.; Stacey, D. N.; Woodgate, G. K. *J. Phys. B* 1982, 15, 993.

104. Thompson, R. C.; Hanser, A.; Bekk, K.: Meisel, G.; Frolich, D. *Z. Physik A* 1982, 305, 89.

105. Lorenzen, C. J.; Niemax, K. *J. Phys. B* 1982, 15, L139.

106. Pendrill, L. R.; Niemax, K. *J. Phys. B* 1982, 15, L147.

107. Michelson, A. *Phil. Mag.* 1891, 31, 338.

108. Fabry, C.; Perot, A. *Ann. Chim. et Phys.* 1897, 12, 459.

109. Pauli, W. *Naturwissenschaften* 1924, 12, 74.

110. Seltzer, E. C. *Phys. Rev.* 1969, 188, 1916.

111. Hughes, D. J.; Eckart, C. *Phys. Rev.* 1930, 36, 694.

112. Heilig, K.; Steudel, A. *At. Data Nucl. Data Tables* 1974, 14, 613.

113. Barret, R. C. *Rep. Prog. Phys.* 1974, 37, 1.

114. Armstrong, L. Jr. "Theory of the Hyperfine Structure of Free Atoms" John Wiley & Sons, New York, 1971, Chapter 2.

115. Ritschl, R. *Z. fur Phys.* 1932, 79, 1.

116. Schuler, H.; Schmidt, T. *Z. Phys.* 1936, 100, 113.

117. Murakawa, K. *J. Phys. Soc. Jap.* 1956, 11, 774.

118. Fischer, W. *Z. Phys.* 1961, 161, 89.

119. Prasad, A. S.; Oberleas, D. "Trace Elements in Human Health and Disease" Academic Press, New York, 1976, Volume 2, Chapter 26 - 46.

120. Scheinberg, I. H.; Sternlieb, I. *Med. Clin. N. Am.* 1963a, 47, 815.

121. Neumann, P. Z.; Silverberg, M. *Nature* 1967, 25, 775.

122. Wrenn, M. E.; Singh, N. P.; Ibrahim, S. A.; Cohen, N. *Anal. Chem.* 1978, 50, 12, 1712.

123. Hirao, Y.; Fukumoto, K.; Sugisaki, H.; Kimura, K. *Anal. Chem.* 1979, 51, 6, 651.

124. Schery, S. D. *Anal. Chem.* 1980, 52, 12, 1957.

125. Lowman, J. T.; Krivit, W. *J. Lab. & Clin. Med.* 1963, 61, 6, 1042.

126. Schmidt, P. F.; Riley, J. E., Jr. *Anal. Chem.* 1979, 51, 2, 306.

127. Carni, J. J.; James, W. D.; Koirtyohann, S. R.; Morris, E. R. *Anal. Chem.* 1980, 52, 1, 216.

128. Hachey, D. L.; Blais, J. C.; Klein, P. D. *Anal. Chem.* 1980, 52, 1131.

129. Kowantzki, R.; Peters, F.; Reil, G. H.; Haas, G. *Biomed. Mass Spectrom.* 1980, 7, 540.

130. Yergey, A. L.; Vieira, N. E.; Hansen, J. W. Anal. Chem. 1980, 52, 1811.

131. Lehmann, W. D.; Kessler, H. "Stable Isotopes" Elsevier, Amsterdam, 1982.

132. Houk, R. S.; Thompson, J. J. Biomed. Mass Spectrom. 1983, 10, 107.

133. Douglas, D. J.; Quan, E. S. K.; Smith, R. G. Spectrochim. Acta B 1983, 38B, 39.

134. Smith, D. L. Anal. Chem. 1983, 55, 2391.

135. Buckley, W. T.; Huckin, S. N.; Budac, J. J.; Elgendorf, G. K. Anal. Chem. 1982, 54, 504.

136. Harvey, B. R. Anal. Chem. 1978, 50, 1866.

137. Koppenaal, D. W.; Lett, R. G.; Brown, F. R.; Manahan, S. E. Anal. Chem. 1980, 52, 44.

138. Goodfellow, G. I. Appl. Spec. 1967, 21, 39.

139. Rossi, G.; Omenetto, N. Appl. Spec. 1967, 21, 329.

140. Koirtyohann, S. R.; Feldman, C. "Developments in Applied Spectroscopy" J. E. Forrette and E. Lanterman Eds., Plenum Press Inc., New York, 1964, Volume 3, page 180 - 189.

141. Popham, R. E.; Schrenk, W. G. Appl. Spec. 1968, 22, 192.

142. Sebens, C.; Vollmer, J.; Slavin, W. Perkin-Elmer Atomic Absorption Newsletter 1964, 3, 165.

143. Kirkbright, G. F.; Wilson, P. J. Anal. Chem. 1974, 46, 1414.

144. Robinson, J. W. "Atomic Absorption Spectroscopy" 2nd ed., Marcel Dekker Inc., New York, 1975.

145. Lomdahl, G. S.; Norris, T.; Sullivan, J. V. Am. Lab. 1983 March, 66.

146. Bethge, P. O. Anal. Chem. Acta 1954, 10, 317.

147. Weissbluth, M. "Atoms and Molecules" Academic Press, New York, 1978.

148. Bearn, A. G.; Kunkel, H. G. Proc. Soc. Exp. Biol. N. Y., 1954, 85, 44.

149. Matthews, W. B. J. Neurol. Neurosurg. Psychiat. 1954, 17, 242.

150. Osborn, S. B.; Walshe, J. M. Clin. Sci. 1905, 29, 575.

151. Ember, L. R. Chem. & Eng. News 1980, 58, 25, 28.

152. Sciquest 1980, 53, 5, 26.

153. Spielholtz, G. I.; Kaplan, F. S. Talanta 1980, 27, 997.

154. Chem. & Eng. News 1981, 59, 20, 30.

155. Stukas, V. J.; Wong, C. S. Science 1981, 211, 1424.

156. York, D.; Farquhar, R. "The Earth's Age and Geochronology" Pergamon, Toronto, 1972.

157. Spooner, E. T. C.; Gale, N. H. Nature 1982, 296, 239.

158. White, W. M.; Hofmann, A. W. Nature 1982, 296, 821.

159. Bell, K.; Blenkinsop, J.; Cole, T. J. S.; Menagh, D. P. Nature 1982, 298, 251.

160. Smith, C. B. Nature 1983, 304, 51.

161. El-Daoushy, F.; Tolenen, K.; Rosenberg, R. Nature 1982, 296, 429.

162. Koide, M.; Bruland, K. W.; Goldberg, E. D. Geochim. Cosmochim. Acta 1973, 37, 1171.

163. Robbins, J. A.; Edgington, D. N. Geochim. Cosmochim. Acta 1975, 39, 285.

164. Keisch, B.; Callahan, R C. Archaeometry 1976, 18, 181.

165. Fleming, S. Physics Today 1980, 33, 4, 34.

166. Fairbank, W. M. Jr.; Hansch, T. W.; Schawlow, A. L. J. Opt. Soc. Am. 1975, 65, 199.

167. Gelbwachs, J. A.; Klein, C. F.; Wessel, J. E. J. Quantum Elect. 1978, 14, 121.

168. Hurst, G. S.; Nayfeh, M. H.; Young, J. P. Appl. Phys. Lett. 1977, 30, 229.

169. Hurst, G. S.; Nayfeh, M. H.; Young, J. P. Phys. Rev. A 1977, 15, 2281.

170. Bolshov, M. A.; Zybin, A. V.; Koloshnikov, V. G.; Vasnetsov, M. V. Spectrochim. Acta 1981, 36B, 4, 345.

171. Pan, C. L.; Prodon, J. V.; Fairbank, W. M. Jr.; She, C. Y. Opt. Lett. 1980, 5, 459.

172. Fraser, L. M.; Winefordner, J. D. Anal Chem. 1972, 44, 1444.

173. Winefordner, J. D. J. Chem. Ed. 1978, 55, 2, 72.

174. Bolshov, M. A.; Zybin, A. V.; Smirenkina, I. I. Spectrochim. Acta 1981, 36B, 12, 1143.

175. Fraser, L. M.; Winefordner, J. D. Anal. Chem. 1971, 43, 1693.

176. Kuhl, J.; Spitschan, H. Opt. Commun. 1973, 7, 256.

177. Smith, B.; Winefordner, J. D.; Omenetto, N. J. Appl. Phys. 1977, 48, 2676.

178. Green, R. B.; Travis, J. C.; Keller, R. A. Anal. Chem. 1976, 48, 1955.

179. Chester, T. L.; Winefordner, J. D. Spectrochim. Acta 1976, 31B, 21.

180. Koizumi, H.; Yasuda, K. Spectrochim. Acta 1976, 31B, 237.

181. Goff, D. A.; Yeung, E. S. Anal. Chem. 1978, 50, 625.

182. Wieman, C.; Hansch, T. W. Phys. Rev. Lett. 1976, 36, 1170.

183. Smith, P. W.; Hansch, T. W. Phys. Rev. Lett. 1971, 26, 740.

184. Murnick, D. E.; Feld, M. S.; Burns, M. M.; Kuhl, T. U.; Pappas, P. G. "Laser Spectroscopy IV" Walther, H.; Rothe, K. W. Eds., 1979, Springer-Verlag, Berlin, p 195-202.

185. Vasconcellos, J. I. C.; Villaverde, A. B.; Roversi, J. A. J. Phys. B: At. Mol. Phys. 1984, 17, 1189.

186. Heiman, D.; Hellwarth, R. W.; Levenson, M. D.; Martin, G. Phys. Rev. Lett. 1976, 36, 189.

187. Levenson, M. D.; Song, J. J. J. Opt. Soc. Am. 1976, 66, 641.

188. Levenson, M. "Introduction to Nonlinear Spectroscopy" 1982, Academic Press, New York, Chap. 1, 3, 4.

189. Maker, P. D.; Terhune, R. W. Phys. Rev. A 1965, 137, 801.

190. Wang, C. C. Phys. Rev. 1966, 152, 149.

191. Liao, P. F; Bjorklund, G. C. Phys. Rev. Lett. 1976, 36, 584.

192. Delsart, C.; Keller, J.-C. "Laser Spectroscopy III" Hall, J. L.; Carlsten, J. L. Eds., Springer-Verlag, Berlin, 1977.

193. Smith, P. W.; Hansch, T. Phys. Rev. Lett. 1971, 26, 740.

194. Saikan, S. J. Opt. Soc. Am. 1978, 68, 1184.

195. Radloff, W.; Ritze, H.-H. "Laser Spectroscopy IV" Walther, H.; Rothe, K. W. Eds., Springer-Verlag, Berlin, 1979.

196. Sargent, M. III; Scully, M. O.; Lamb, W. E., Jr. "Laser Physics" Addison-Wesley, London, 1974.

197. Dienes, A. Phys. Rev. 1968, 174, 400.

198. Moeller, C. E.; Grieser, D. R. Appl. Opt. 1969, 8, 206.

199. Yeung, E. S.; Steenhoek, L. E.; Woodruff, S. D.; Kuo, J. C. Anal. Chem. 1980, 52, 1399.

200. Yeung, E. S.; Steenhoek, L. E; Tong, W. G.; Bobbitt, D. R. Anal. Chem. 1981, 53, 1936.

201. Olsen, E. D. "Modern Optical Methods of Analysis" McGraw-Hill, New York, 1975, Chap. 5.

202. Goff, D. A.; Yeung, E. S. Anal. Chem. 1978, 50, 625.

203. Winefordner, J. D. Chemtech 1975, 123.

204. Tong, W. G.; Yeung, E. S. Talanta 1984 September issue, in press.

# ACKNOWLEDGMENTS

I am very grateful to my major professor, Dr. Ed Yeung, for providing me with his expert and enthusiastic guidance throughout my graduate education, and for granting me the opportunity to be a part of his challenging and innovative research program.

I wish to thank Dr. David Lewis for valuable discussions in some of the calculations in Chapter II, and Dr. Dennis Johnson for the use of the miniaturized Bethge apparatus.

My thanks also to Dave, Scott, Gretchen, Larry, J.C., Bernie, Julianna, Barb and many former and current members of Dr. Ed Yeung's research group for making a very rewarding part of my life in Ames more enjoyable. I would also like to thank the Iowa State University Computation Center for the use of its facilities in editing and printing this dissertation.

My special thanks to my mother, my brother Richard, my sisters Rinnie, Penny, Susan, Laura and Joanne for their constant understanding, encouragement and love. Finally, to my late father, whose encouragement has always been and will always be a guiding light for me to attain my goals, this dissertation is dedicated.

# APPENDIX: COMPUTER PROGRAMS

This appendix contains brief descriptions and source file listings of computer programs used to collect and treat data from the optogalvanic spectroscopy and the Doppler-free polarization spectrsocopy experiments. The programs are summarized in Table 11.

Table 11. Summary of computer programs

| Program | Function |
|---|---|
| OGE2M | Collect optogalvanic data from the lock-in amplifier and laser frequency values from the wavemeter, and display the hyperfine profile on the graphics monitor |
| RTCU | Generate a table of Doppler-broadened hyperfine profiles with various isotope ratio and temperature values |
| GRAPH3 | Display user selected versions of theoretical and experimental hyperfine structures |
| LARA2 | Calculate isotope ratio by matching experimantal and theoretical profiles using a least-squares criterion |
| 6J | Calculate 6j symbols |
| RATIO | Plot the 3D graphics of Figure 15 |

Table 11. ( Continued )

| Program | Function |
|---|---|
| 3DRT | Display the sum of squares of the deviations in ratio-temperature surface<br>(See Figure 17) |
| GAUSN | Simulate Gaussian noise on hyperfine structures to check the noise effect on ratio calculations |
| GSN3D | Plot the 3D graphics of Figure 19 |
| PSNAD1 | Collect Doppler-free polarization spectrum from the lock-in amplifier and laser frequency values from the wavemeter for Na D1 line |
| PS3D | Display 3D graphics of dichroism and birefringence resonance curves<br>(See Figure 21) |
| GRAPH4 | Display user selected versions of experimental Doppler-free polarization spectra |
| PS3D2 | Display 3D graphics of signal dependence on pump polarization plane<br>(See Figure 23) |

```
C       ***** PROGRAM OGE2M *****
C
C       PROGRAM FOR COLLECTING OPTOGALVANIC
C       DATA FROM THE LOCK-IN AMPLIFIER
C       AND THE LASER FREQUENCY VALUES FROM THE
C       WAVEMETER.  IT ALSO DISPLAYS THE HYPERFINE
C       STRUCTURE ON THE GRAPHICS MONITOR USING
C       2DLIB GRAPHICS LIBRABRY..
C       2 DATA POINTS PER SECOND.
C
C       COMPILE AND LINK WITH @OGE2M
C       OCT 1983.  W.G.TONG
C
        PROGRAM OGE2M
        DIMENSION SIG(650),FQ(650)
        WRITE(5,5)
5       FORMAT(' ENTER FILE #, # PTS.')
        READ (5,10)IFILE,NPTS
10      FORMAT(3I6)
C       HIT RETURN KEY TO START
        READ(5,10)ISTART
15      DO 50 I=1,NPTS
        ICMF=0
        CALL SETR (4,0,500.,ICMF)
        CALL WAVE3(FQ(I))
        SIG(I)=FLOAT(IADC(0))
        CALL LED(SIG(I),'F6.1')
        IF(FQ(I).GT.0.50) GO TO 20
        FQ(I)=FQ(I)+1.00
20      IF (ICMF.EQ.0)GO TO 20
50      CONTINUE
        IF(IFILE.EQ.0)GO TO 15
        WRITE(IFILE)((SIG(I),I=1,NPTS),(FQ(I),I=1,NPTS))
C
C       FREQUENCY COORDINATE
```

```
      FQI=0.05
      FQ(1)=.55
      DO 54 NW=2,NPTS
      FQD=FQ(NW)-FQ(NW-1)
      IF(FQD.GT.(FQI)) GO TO 53
      IF(FQD.LT.(-FQI))GO TO 53
      GO TO 54
53    FQ(NW)=FQ(NW-1)
54    CONTINUE
C
C     DISPLAY THE HYPERFINE STRUCTURE
      CALL INIPLT(5,9.5,8.5)
      CALL WINDOW(1.5,7.5,1.,7.5)
      CALL VUPORT(17289.4,17290.4,-400.,4000.)
      CALL AXIS(.2,400.,'FREQUENCY',9,2,1,'OGE',3,2,0)
      DO 100 NOR=1,NPTS
100   FQ(NOR)=FQ(NOR)+17289.0
      CALL LINE(FQ,SIG,180,0,0,0,0)
      CALL ENDPLT
      CALL EXIT
      END
    OGE2M.COM

!       INDERECT COMMAND FILE
!       FOR OGE2M
!
!       M.G.TONG
!
!
R FORTRA
OGE2M,TT:=OGE2M/L:0/N/U
^C
SO/NOQ DK:
!
!       USING 2DLIB GRAPHICS LIBRARY.
LINK OGE2M,WAVE3,2DLIB,SY:LPSLIB
```

```
C          ----- SUBROUTINE WAVE3 -----
C
C          PROGRAM TO READ INCOMING FREQUENCY VALUES
C          IN BCD CODE FROM THE WAVEMETER.
C          DATA PULSE WIDTH 70 MICROSEC, 10/ 850 MICROSEC.
C          FUNCTION OR SUBROUTINE NOT USED FOR DIGITAL
C          INPUT LINES TO AVOID INCONSISTENT TIMING.
C
C          JAN 1983.    W.G.TONG.
C
           SUBROUTINE WAVE3(FREQ)
           EXTERNAL IDIR
           DIMENSION IB1(101),IB2(101),IB4(101),IB8(101)
           DIMENSION IDIO(10)
1          IMASK="1000
           DO 200 N=7,9
150        IDA=IDIR(0,0,IMASK,1)
           IDB=IDIR(0,0,IMASK,1)
           ID=IDA-IDB
           IF(ID.LT.500) GO TO 150
           IDUM=IDIR(0,0,"1,1)
           IB1(N)=IDIR(0,0,"2,1)
155        IDA=IDIR(0,0,IMASK,1)
           IDB=IDIR(0,0,IMASK,1)
           ID=IDA-IDB
           IF(ID.LT.500) GO TO 155
           IDUM=IDIR(0,0,"1,1)
           IB2(N)=IDIR(0,0,"4,1)
160        IDA=IDIR(0,0,IMASK,1)
           IDB=IDIR(0,0,IMASK,1)
           ID=IDA-IDB
           IF(ID.LT.500) GO TO 160
           IDUM=IDIR(0,0,"1,1)
           IB4(N)=IDIR(0,0,"10,1)
165        IDA=IDIR(0,0,IMASK,1)
           IDB=IDIR(0,0,IMASK,1)
```

```
      ID=IDA-IDB
      IF(ID.LT.500) GO TO 165
      IDUM=IDIR(0,0,"1,1)
      IB8(N)=IDIR(0,0,"20,1)
200   CONTINUE
C
      IMASK="400
      DO 300 N=10,12
250   IDA=IDIR(0,0,IMASK,1)
      IDB=IDIR(0,0,IMASK,1)
      ID=IDA-IDB
      IF(ID.LT.250) GO TO 250
      IDUM=IDIR(0,0,"1,1)
      IB1(N)=IDIR(0,0,"2,1)
255   IDA=IDIR(0,0,IMASK,1)
      IDB=IDIR(0,0,IMASK,1)
      ID=IDA-IDB
      IF(ID.LT.250) GO TO 255
      IDUM=IDIR(0,0,"1,1)
      IB2(N)=IDIR(0,0,"4,1)
260   IDA=IDIR(0,0,IMASK,1)
      IDB=IDIR(0,0,IMASK,1)
      ID=IDA-IDB
      IF(ID.LT.250) GO TO 260
      IDUM=IDIR(0,0,"1,1)
      IB4(N)=IDIR(0,0,"10,1)
265   IDA=IDIR(0,0,IMASK,1)
      IDB=IDIR(0,0,IMASK,1)
      ID=IDA-IDB
      IF(ID.LT.250) GO TO 265
      IDUM=IDIR(0,0,"1,1)
      IB8(N)=IDIR(0,0,"20,1)
300   CONTINUE
```

```
C
          L=3
          K=7
          DO 850 II=1,2
          ISUM1=0
          ISUM2=ISUM1
          ISUM4=ISUM2
          ISUM8=ISUM4
          KK=K+2
          DO 750 N=K,KK
          ISUM1=ISUM1+IB1(N)
          ISUM2=ISUM2+IB2(N)
          ISUM4=ISUM4+IB4(N)
750       ISUM8=ISUM8+IB8(N)
          IF(ISUM1-5)760,760,770
760       IBCD1=1
          GO TO 775
770       IBCD1=0
775       IF(ISUM2-6)780,780,790
780       IBCD2=1
          GO TO 795
790       IBCD2=0
795       IF(ISUM4-12)800,800,810
800       IBCD4=1
          GO TO 815
810       IBCD4=0
815       IF(ISUM8-24)820,820,830
820       IBCD8=1
          GO TO 835
830       IBCD8=0
835       IDIG(L)=(IBCD1*1)+(IBCD2*2)+(IBCD4*4)+(IBCD8*8)
```

```
      K=K+3
      L=L+1
850   CONTINUE
      FREQ=(IDIG(3)*0.1)+(IDIG(4)*0.01)
      IDUM=0
      CALL LED(IDUM,'I6')
      CALL LED(FREQ,'F6.2')
      RETURN
      STOP
      END
```

```
C        ***** PROGRAM RTCU *****
C
C        PROGRAM FOR GENERATING A TABLE OF
C        DOPPLER-BROADENED HYPERFINE PROFILES WITH
C        VARIOUS ISOTOPE RATIO AND TEMPERATURE VALUES.
C
C        COMPILE AND LINK WITH @RTCU
C        1982.    W.G.TONG.
C
         PROGRAM RTCU
         DIMENSION XX(5,201)
         DIMENSION X(201),VO(20)
         DIMENSION R(20),T(20),FQ(201)
         DIMENSION XFQ(5,201),XAREA(20)
         NPTS=200
         P=3.
         CALL PRINT('----- RTCU MENU -----')
         CALL PRINT('1. SIMULATE ONE PROFILE')
         CALL PRINT('2. SIMULATE ONE PROFILE, TT: VO(N)')
         CALL PRINT('3. SIMULATE A TABLE OF PROFILES')
         CALL PRINT('--- ENTER YOUR CHOICE ---')
         READ (5,*)RTIF
         IF(RTIF-2)10,10,50
C
10       CALL PRINT('ENTER RATIO, TEMP, VO(1)')
         READ(5,15)R(1),T(1),VO(1)
15       FORMAT(2F10.3,F12.4)
         CALL DOPCU(R(1),T(1),P,X,FQ,NPTS,VO(1),RTIF)
         AREA=0.
         DO 20 J=1,NPTS
         XFQ(1,J)=FQ(J)
         XX(1,J)=X(J)
         AREA=AREA+X(J)
20       CONTINUE
         XAREA(1)=AREA
```

```
          WRITE(71)((XX(1,NPTS),NPTS=1,200),
        1 (XFQ(1,NPTS),NPTS=1,200),XAREA(1))
          GO TO 2000
C
50        CALL PRINT('ENTER 1ST PEAK POSITION VO(1)')
          CALL PRINT('(17289.710)')
          READ(5,70)VO(1)
          CALL PRINT(' ENTER # OF ROW & COLUMN IN TABLE')
          READ(5,*)JROW,JCOL
          CALL PRINT(' ENTER 1ST RATIO & INCR OF TABLE')
          READ(5,70)R(1),RINCR
70        FORMAT(2F12.5)
          CALL PRINT(' ENTER 1ST TEMP & INCR OF TABLE')
          READ(5,70)T(1),TINCR
          DO 100 IR=2,JROW
          R(IR)=R(IR-1)+RINCR
100       CONTINUE
          DO 200 IT=2,JCOL
          T(IT)=T(IT-1)+TINCR
200       CONTINUE
C
C         GENERATE TABLE OF DOPPLER PROFILES.
C         EACH ROW STORED IN SEPARATE FILE.
          CALL PRINT('ENTER 1 FOR FTN71')
300       READ(5,*)MM
          DO 1800 NT=1,JROW
450       IFILE=MM+70
          DO 1000 NN=1,JCOL
          CALL DOPCU(R(MM),T(NN),P,X,FO,NPTS,VO(1),RTIF)
          AREA=0.
          DO 500 J=1,NPTS
          XFQ(NN,J)=FO(J)
          XX(NN,J)=X(J)
          AREA=AREA+X(J)
500       CONTINUE
          XAREA(NN)=AREA
```

```
1000     CONTINUE
         WRITE(5,1500)MM,XAREA(I),XAREA(JCOL)
1500     FORMAT(I3,2X,2(F10.0,1X))
         WRITE(IFILE)(((XX(MM,NPTS),MM=1,5),NPTS=1,200),
     1 (XFO(5,NPTS),NPTS=1,200),(XAREA(MM),MM=1,5))
         MM=MM+1
         IF(MM.EQ.(JROW+1))GO TO 2000
1800     CONTINUE
2000     CONTINUE
         STOP
         END
C
C
C        ~~~~~ SUBROUTINE DOPCU ~~~~~
C
C        PROGRAM FOR GENERATING DOPPLER-BROADENED
C        THEORETICAL HYPERFINE PROFILE FOR
C        CU I 5782 A TRANSITION.
C
         SUBROUTINE DOPCU(R,T,P,X,FO,NPTS,V01,RTIF)
         DIMENSION AM(12),AK(12),VS(11),VO(12)
         DOUBLE PRECISION V
         DOUBLE PRECISION Z(12)
         DIMENSION X(201),FO(201)
C
C        11 HYPERFINE SHIFT VALUES FOR 12 COMPONENTS.
         IF(RTIF.EQ.2)GO TO 10
         DATA VS /.070,.164,.192,.234,.265,.277,
     1 .305,.334,.365,.402,.422/
         GO TO 20
10       CALL PRINT('ENTER HYPERFINE SHIFT VS(1) TO VS(11)')
         READ(5,15)VS(1),VS(2),VS(3),VS(4),VS(5),
     1 VS(6),VS(7),VS(8),VS(9),VS(10),VS(11)
15       FORMAT(F12.4,11F7.4)
20       CONTINUE
```

```
C
C     HYPERFINE-COMPONENT STRENGTHS.
C     FOR COPPER 63
      DATA AK(1),AK(3),AK(4)/1000.,357.,357./
      DATA AK(7),AK(8),AK(9)/357.,72.,143./
C     FOR COPPER 65
      AK(2)=AK(1)/R
      AK(5)=AK(3)/R
      AK(6)=AK(4)/R
      AK(10)=AK(7)/R
      AK(11)=AK(8)/R
      AK(12)=AK(9)/R
C
C     ISOTOPE MASS FOR CORRESPONDING PEAKS.
      DATA AM /63.,65.,63.,63.,65.,65.,
     1 63.,63.,63.,65.,65.,65./
C
      VO(1)=VO1
      DO 100 N=2,12
100   VO(N)=VO(1)+VS(N-1)
      V=17289.5
      NPTS=200
      VINC=.0045
      S=-5.4217E12
      DO 300 J=1,NPTS
      SUMZ=0.
      DO 200 L=1,12
      E=S*((AM(L))/T)*(((V-(VO(L)))/(VO(L)))**2)
      Z(L)=P*(AK(L))*(EXP(E))
      SUMZ=SUMZ+Z(L)
200   CONTINUE
      X(J)=SUMZ
      FQ(J)=V-17289.00
D     CALL LED (X(J),'F6.1')
300   V=V+VINC
      RETURN
      END
```

```
      RTCU.COM
!       INDIRECT COMMAND FILE
!       RTCU
!
!       W.G.TONG.
!
SET ERROR NONE
DEL/NOQ RTCU.(LST,SAV,OBJ)
SET ERROR ERROR
!
R FORTRA
RTCU,TT:=RTCU/L:0/W/U/N:17
^C
SQ/NOQ DK:
!
!       USING FLOATING POINT PROCESSOR.
!LINK RTCU,FPLIB,SY:LPSLIB
!
!       NOT USING FLOATING POINT PROCESSOR.
LINK RTCU,SY:LPSLIB
!
DEL/NOQ RTCU.OBJ
DIR/ALP/FULL


.
```

```
C        ***** PROGRAM GRAPH3 *****
C
C        PROGRAM FOR DISPLAYING OPTOGALVANIC SIGNAL
C        VS LASER FREQUENCY USING USER SELECTED
C        VERSIONS OF HYPERFINE STRUCTURES.
C        UPDATED VERSION OF GRAPH2.
C
C        COMPILE AND LINK WITH @GRAPH3.
C        OCT 1983. W.G.TONG
C
         PROGRAM GRAPH3
         DIMENSION XX(1,201),SSIG(220)
         DIMENSION SIG(200),XAREA(1)
         DIMENSION BLINE(200),SIGN(201)
         DIMENSION FQ(201),X(200),ASG(220)
         DIMENSION FQA(200),XFQ(1,200)
         DIMENSION AFQ(200),ASIG(200)
         DIMENSION XPLT(200),YPLT(200)
         INTEGER*2 C(10,21)
         EQUIVALENCE (BLINE(1),FQA(1))
         EQUIVALENCE (ASIG(1),SSIG(1))
C
C        INITIALIZE THE GRAPHICS FRAME
         CALL INIPLT(5,10.5,8.5)
         CALL WINDOW(1.5,8.5,.7,7.7)
         CALL VUPORT(17289.4,17290.4,-400.,4000.)
         CALL ENDPLT
C
601      CALL PRINT('ENTER FILE #, # PTS')
         READ(5,*)IFILE,NPTS
22       NPTSS=NPTS-15
         NSS=NPTSS-5
         READ(IFILE)((X(J),J=1,NPTS),(FQ(I),I=1,NPTS))
C
C        FREQUENCY COORDINATE
         CALL PRINT('--- FREQUENCY COORDINATE ---')
```

```
          CALL PRINT('1. AUTO')
          CALL PRINT('2. MANUAL')
          CALL PRINT('--- ENTER YOUR CHOICE ---')
          READ(5,*)IFREQC
          IF(IFREQC.EQ.1)GO TO 605
          CALL PRINT('ENTER FQ(1),FQI     (.55,.05)')
          READ(5,*)FQ(1),FQI
          GO TO 610
605       FQ(1)=.55
          FQI=.05
610       DO 24 NN=2,NPTS
          FQD=FQ(NN)-FQ(NN-1)
          IF(FQD.GT.(FQI)) GO TO 23
          IF(FQD.LT.(-FQI)) GO TO 23
          GO TO 24
23        FQ(NN)=FQ(NN-1)
24        CONTINUE
C
C         DETERMINE BASELINE
          CALL PRINT('----BASELINE DETERMINATION----')
          CALL PRINT('1. AUTO')
          CALL PRINT('2. MANUAL')
          CALL PRINT('------ENTER YOUR CHOICE-------')
          READ(5,*,ERR=24)IBASE
          IF(IBASE.EQ.2)GO TO 41
C         AUTO BASELINE DETERMINATION
28        BSTART=0.
          NS=NPTS/20
          DO 30 JJ=1,NS
          BSTART=BSTART+X(JJ)
30        CONTINUE
          BNS=NS
          BSTART=BSTART/BNS
          BEND=0.
          NEN=NPTS-NS+1
```

```
      DO 40 JJ=NEN,NPTS
      BEND=BEND+X(JJ)
40    CONTINUE
      BNS=NPTS-NEN+1
      BEND=BEND/BNS
      BPTS=NEN-1
      BINCR=(BEND-BSTART)/BPTS
      DO 44 J=1,NPTS
      BJ=J
      BLINE(J)=BSTART+(BINCR*BJ)
44    SIG(J)=X(J)-BLINE(J)
      GO TO 55
C     MANUAL BASELINE DETERMINATION
41    CALL PRINT('ENTER STARTPT,ENDPT,#AVE PT')
      READ(5,*,ERR=41)NSTA,NEND,NAVE
      BSTART=0.
      DO 42 JJ=NSTA,NSTA+NAVE
42    BSTART=BSTART+X(JJ)
      BNAVE=NAVE+1
      BSTART=BSTART/BNAVE
      BEND=0.
      DO 43 JJ=NEND,NEND+NAVE
43    BEND=BEND+X(JJ)
      BNAVE=NAVE+1
      BEND=BEND/BNAVE
      BPTS=NEND-NSTA
45    BINCR=(BEND-BSTART)/BPTS
      DO 47 J=1,NSTA
      BJ=J
      BLINE(J)=BSTART-(BINCR*BJ)
47    SIG(J)=X(J)-BLINE(J)
```

```
      DO 50 J=NSTA,NPTS
      BJ=J
      BLINE(J)=BSTART+(BINCR*BJ)
      SIG(J)=X(J)-BLINE(J)
50    CONTINUE
      KK=1
      NW=NPTS/20
55    CONTINUE
C
C     DETERMINE THE 1ST PEAK HEIGHT OF THE COLLECTED
C     SPECTRUM AND ITS POSITION ALONG THE
C     FREQUENCY COORDINATE.
      DIFF(I)=SIG(I)-SIG(I-1)
      DO 80 I=2,NPTS
      IF(DIFF(I).GT.50.) GO TO 70
      GO TO 80
70    IF(DIFF(I).LT.1.)GO TO 75
      I=I+1
      GO TO 70
75    CONTINUE
      JVV=(I-1)
      SMAX=SIG(I-1)
      I=NPTS
80    CONTINUE
      WRITE(5,90)JVV
90    FORMAT(' 1ST PEAK LOCATED AT PT #',I6,/)
C     FIND AREA
      AREA=0.
      DO 100 J=1,NPTS
      AREA=AREA+SIG(J)
100   CONTINUE
      SAREA=AREA
C
C     FREQUENCY AVERAGING, 5 PTS.
C     OVERLAP 5 PTS.
```

```
        DO 618 I=6,NPTSS
        FQS=0
        DO 612 II=(I-5),(I+5)
612     FQS=FQ(II)+FQS
        FQ(I)=FQS/11
        IE=I+5
        FQS=0
        DO 614 II=(IE-5),(IE+5)
614     FQS=FQ(II)+FQS
        FQ(IE)=FQS/11
        FQDIFF=FQ(IE)-FQ(I)
        FQI=FQDIFF/(IE-I)
        FQA(I)=FQ(I)
        DO 616 K=(I+1),IE
616     FQA(K)=FQA(K-1)+FQI
        I=I+5
618     CONTINUE
C
C       PLOT GRAPHICS FRAME.
110     CALL AXIS(.2,400.,'FREQUENCY',9,2,1,'OGE',3,2,0)
        CALL PLTSTR(250,530,'HYPERFINE STRUCTURE',19,1,2)
        CALL PLTSTR(350,510,'CU 5782 A',9,1,1)
        CALL PLTSTR(350,500,'NON-RESONANT LINE',17,1,1)
        CALL PLTSTR(350,490,'RING DYE LASER',14,1,1)
        CALL PLTSTR(350,480,'27 GHZ SCAN',11,1,1)
        CALL PLTSTR(350,470,'100 SEC SCAN TIME',17,1,1)
        CALL PLTSTR(350,460,'1 KHZ MODULATION',16,1,1)
        CALL PLTSTR(350,450,'200 PT/ DATA FILE',17,1,1)
        CALL ENDPLT
C
        CALL PRINT(' -------------GRAPH3 MENU ---------------')
        CALL PRINT('1. PLOT THEORECTICAL PROFILE')
        CALL PRINT('2. PLOT NORMALIZED, B.SUBSTRACTED EXPTL')
        CALL PRINT('3. PLOT BASELINE SUBSTRACTED EXPTL')
        CALL PRINT('4. PLOT ALIGNED, N., B. SUBSTRACTED EXPTL')
```

```
      CALL PRINT('5. PLOT ORIGINAL, UNTREATED EXPTL')
      CALL PRINT('6. READ THEORECTICAL PROFILE')
      CALL PRINT('7. READ ANOTHER FTN DATA FILE')
      CALL PRINT('8. EXIT')
      CALL PRINT('----- ENTER ROUTINE # OF YOUR CHOICE ----')
      READ(5,*,ERR=110)LL
      IF(LL.EQ.8)GO TO 603
      IF(LL-6)480,500,601
480   IF(LL-4)490,240,250
490   IF(LL-2)500,580,170
500   CALL PRINT(' ENTER ROW #, COLUMN # OF PT.')
      READ(5,*,ERR=500)MM,MMM
      IF(MM.GT.0)GO TO 535
      GO TO 600
535   IFILE=MM+70
      READ(IFILE)((XX(1,N1),N1=1,200),(XFQ(1,N2),N2=1,200),XAREA(1))
      IF(LL.EQ.6) GO TO 110
C
C     THEORETICAL DOPPLER PROFILE.
      CALL PRINT('ENTER AMP. FACTOR (DEFAULT 1)')
      READ(5,*)AMP
      IF(AMP.EQ.0.0) GO TO 538
      DO 537 NTH=1,200
537   XX(1,NTH)=XX(1,NTH)*AMP
538   DO 536 NTH=1,200
536   XFQ(1,NTH)=XFQ(1,NTH)+17289.00
      CALL LINE(XFQ,XX,180,0,0,0,0)
      CALL PLTSTR(350,420,'THEORECTICAL',12,1,1)
      CALL ENDPLT
      GO TO 110
C
C     AREA-NORMALIZED, BASELINE-SUBSTRACTED,
C     EXPERIMENTAL PROFILE.
580   DO 150 J=6,NPTSS
      SIGN(J)=(SIG(J)/SAREA)*XAREA(MMM)
```

```
      XPLT(J)=FOA(J)+17289.0
150   YPLT(J)=SIGN(J)
      CALL LINE(XPLT,YPLT,NSS,0,0,0,0)
      CALL ENDPLT
      GO TO 110
C
C     BASELINE-SUBSTRACTED EXPERIMENTAL PROFILE.
170   DO 172 J=6,NPTSS
      XPLT(J)=FOA(J)+17289.0
172   YPLT(J)=SIG(J)
      CALL LINE(XPLT,YPLT,NSS,0,0,0,0)
      CALL ENDPLT
      GO TO 110
C
C     FREQUENCY-ALIGNED,AREA-NORMALIZED,
C     BASELINE-SUBSTRACTED EXPERIMENTAL PROFILE.
C     ASSIGN PTS ALONG FO COORD WITH .0045 INCR
C     AND FIND CORRESPONDING INTENSITIES.
240   CALL PRINT('-----PLEASE WAIT-----')
      AFO(1)=.575
      DO 310 I=2,150
310   AFO(I)=AFO(I-1)+.0045
      DO 315 I=5,NPTSS
315   SIGN(I)=(SIG(I)/SAREA)*XAREA(NNN)
      DO 390 JA=1,150
      DO 380 I=6,NPTSS
      IF(FOA(I).LT.AFO(JA)) GO TO 380
      IF(FOA(I).GT.AFO(JA)) GO TO 320
      ASIG(JA)=SIGN(I)
      GO TO 390
320   FOG=FOA(I)-FOA(I-1)
      FOGG=AFO(JA)-FOA(I-1)
      ASIG(JA)=SIGN(I-1)+((SIGN(I)-SIGN(I-1))*(FOGG/FOG))
      GO TO 390
380   CONTINUE
390   CONTINUE
```

```
      CALL PRINT('-----DATA SMOOTHING----')
      CALL PRINT('1. YES')
      CALL PRINT('2. NO')
      CALL PRINT('---ENTER YOUR CHOICE---')
      READ(5,*,ERR=390)ISM
      IF(ISM.EQ.1) GO TO 248
      DO 402 J=1,150
      XPLT(J)=AFQ(J)+17289.0
402   YPLT(J)=ASIG(J)
      CALL MENU
      READ(5,*)ISD
      IF(ISD.EQ.2)GO TO 423
      LINTYP=0
      GO TO 425
423   LINTYP=4
425   CALL DASHLN(XPLT,YPLT,150,0,0,0,0,LINTYP)
      CALL PLTSTR(350,410,'ALIGNED EXPTL',13,1,1)
      CALL ENDPLT
      GO TO 110
C
C     SMOOTHER, FREQUENCY-ALIGNED, AREA-NORMALIZED,
C     BASELINE-SUBSTRACTED EXPERIMENTAL PROFILE.
248   CALL PRINT(' ENTER # OF SMOOTHING PTS')
      CALL PRINT(' 5,7,9,11,13,15,17,19 OR 21')
      READ(5,*)NSMO
      CALL SMOOTH(150,NSMO,ASIG,SSIG)
      DO 702 J=1,150
      XPLT(J)=AFQ(J)+17289.0
702   YPLT(J)=SSIG(J)
      CALL MENU
      READ(5,*)ISD
      IF(ISD.EQ.2)GO TO 708
      LINTYP=0
      GO TO 710
708   LINTYP=4
```

```
710     CALL DASHLN(XPLT,YPLT,150,0,0,0,0,LINTYP)
        CALL PLTSTR(350,410,'SMOOTHED, AL. EXPTL',19,1,1)
        CALL ENDPLT
        GO TO 110
C
C       ORIGINAL, UNTREATED EXPERIMENTAL PROFILE.
250     DO 251 NOR=1,200
251     FQ(NOR)=FQ(NOR)+17289.0
        CALL MENU
        READ(5,*)ISD
        IF(ISD.EQ.2) GO TO 255
        LINTYP=0
        GO TO 257
255     LINTYP=4
257     CALL DASHLN(FQ,X,180,0,0,0,0,LINTYP)
        CALL PLTSTR(350,400,'ORIGINAL DATA',13,1,1)
        CALL ENDPLT
        GO TO 110
600     CONTINUE
603     CALL EXIT
        END
C
        SUBROUTINE MENU
        CALL PRINT('----- GRAPH3 MENU -----')
        CALL PRINT('1. SOLID LINE PLOT')
        CALL PRINT('2. DASHED LINE PLOT')
        CALL PRINT('-- ENTER YOUR CHOICE --')
        RETURN
        STOP
        END
```

```
      GRAPH3.COM
!       INDIRECT COMMAND FILE
!       FOR GRAPH3
!
!       OCT 1983.   M.G.TONG.
!
SET ERROR NONE
DEL/NOQ GRAPH3.(LST,SAV)
SET ERROR ERROR
SQ/NOQ DK:
!
FORT/NOLINENUMBERS/UNITS:14 GRAPH3
SQ/NOQ DK:
!
LINK GRAPH3,SMOOTH,2DLIB
DEL/NOQ GRAPH3.OBJ
!
SET USR SWAP
UNLOAD LS
```

```
C        ***** PROGRAM LARA2 *****
C
C        PROGRAM FOR CALCULATING ISOTOPE RATIO BY MATCHING THE
C        EXPERIMENTAL PROFILE WITH THEORETICAL DOPPLER PROFILES
C        STORED IN A REFERENCE TABLE. PEAK AREA NORMALIZATION
C        AND LEAST-SQUARES FITTING METHOD ARE USED.
C        200-POINT PROFILES.
C
C        COMPILE AND LINK WITH @LARA2
C        1982.   W.G.TONG
C
         PROGRAM LARA2
         DIMENSION XFQ(1,200),SSIG(221),ZFQ(3)
         DIMENSION XX(5,201),X(201),XAREA(5)
         DIMENSION FQ(200),FQA(200),SMAREA(5)
         DIMENSION R(11),T(5),AFQ(200),ASIG(221)
         DIMENSION D(201),SIG(201),SUMD2(10,5)
         DIMENSION BLINE(201),SIGN(201),ASG(221)
         EQUIVALENCE (BLINE(1),FQA(1))
         EQUIVALENCE (X(1),ASIG(1),SSIG(1))
         EQUIVALENCE (FQ(1),AFQ(1))
         INTEGER*2 C(10,21)
C
         CALL PRINT(' ENTER # OF ROW & COLUMN IN TABLE')
         READ(5,*)JROW,JCOL
         CALL PRINT(' ENTER 1ST RATIO & INCR OF TABLE')
         READ(5,730)R(1),RINCR
730      FORMAT(2F10.4)
         CALL PRINT(' ENTER 1ST TEMP & INCR OF TABLE')
         READ(5,730)T(1),TINCR
         DO 1 IR=2,JROW
         R(IR)=R(IR-1)+RINCR
1        CONTINUE
         DO 2 IT=2,JCOL
         T(IT)=T(IT-1)+TINCR
2        CONTINUE
```

```
      CALL PRINT(' ENTER FILE #, # PTS')
      READ(5,*)IFILE,NPTS
      NPTSS=NPTS-15
      READ(IFILE)((X(J),J=1,NPTS),(FQ(I),I=1,NPTS))
C
C     FREQUENCY COORDINATE
      FQI=0.05
      FQ(1)=.55
      DO 24 NW=2,NPTS
      FQD=FQ(NW)-FQ(NW-1)
      IF(FQD.GT.(FQI)) GO TO 23
      IF(FQD.LT.(-FQI)) GO TO 23
      GO TO 24
23    FQ(NW)=FQ(NW-1)
24    CONTINUE
C
C     DETERMINE BASELINE
      CALL PRINT('----BASELINE DETERMINATION----')
      CALL PRINT('1. AUTO.')
      CALL PRINT('2. MANUAL.')
      CALL PRINT('------ENTER YOUR CHOICE-------')
      READ(5,*,ERR=24)IBASE
      IF(IBASE.EQ.2)GO TO 41
C     AUTO BASELINE DETERMINATION.
      BSTART=0.
      NS=NPTS/20
      DO 30 JJ=1,NS
      BSTART=BSTART+X(JJ)
30    CONTINUE
      BNS=NS
      BSTART=BSTART/BNS
      BEND=0.
      NEN=NPTS-NS+1
      DO 40 JJ=NEN,NPTS
      BEND=BEND+X(JJ)
40    CONTINUE
```

```
      BNS=NPTS-NEN+1
      BEND=BEND/BNS
      BPTS=NEN-1
      BINCR=(BEND-BSTART)/BPTS
      DO 44 J=1,NPTS
      BJ=J
      BLINE(J)=BSTART+(BINCR*BJ)
44    SIG(J)=X(J)-BLINE(J)
      GO TO 55
C     MANUAL BASELINE DETERMINATION.
41    CALL PRINT('ENTER STARTPT,ENDPT,#AVE PT')
      READ(5,*,ERR=41)NSTA,NEND,NAVE
      BSTART=0.
      DO 42 JJ=NSTA,NSTA+NAVE
42    BSTART=BSTART+X(JJ)
      BNAVE=NAVE+1
      BSTART=BSTART/BNAVE
      BEND=0.
      DO 43 JJ=NEND,NEND+NAVE
43    BEND=BEND+X(JJ)
      BNAVE=NAVE+1
      BEND=BEND/BNAVE
      BPTS=NEND-NSTA
45    BINCR=(BEND-BSTART)/BPTS
      DO 47 J=1,NSTA
      BJ=J
      BLINE(J)=BSTART-(BINCR*BJ)
47    SIG(J)=X(J)-BLINE(J)
      DO 50 J=NSTA,NPTS
      BJ=J
      BLINE(J)=BSTART+(BINCR*BJ)
      SIG(J)=X(J)-BLINE(J)
50    CONTINUE
      KK=1
      NN=NPTS/20
```

```
D       DO 55 K=1,NW
        KKK=KK+19
D       WRITE(5,60)(SIG(I),I=KK,KKK)
60      FORMAT(1X,20(F6.0))
        KK=KKK+1
55      CONTINUE
C
C       FIND AREA
        AREA=0.
        DO 100 J=1,NPTS
        AREA=AREA+SIG(J)
100     CONTINUE
        SAREA=AREA
        WRITE(5,110)SAREA
110     FORMAT(' SAREA = ',F10.0//)
C
C       FREQUENCY AVERAGING, 5 PTS.
C       OVERLAP 5 PTS.
        DO 618 I=6,NPTSS
        FQS=0
        DO 612 II=(I-5),(I+5)
612     FQS=FQ(II)+FQS
        FQ(I)=FQS/11
        IE=I+5
        FQS=0
        DO 614 II=(IE-5),(IE+5)
614     FQS=FQ(II)+FQS
        FQ(IE)=FQS/11
        FQDIFF=FQ(IE)-FQ(I)
        FQI=FQDIFF/(IE-I)
        FQA(I)=FQ(I)
        DO 616 K=(I+1),IE
616     FQA(K)=FQA(K-1)+FQI
        I=I+5
618     CONTINUE
C
```

```
C       START LEAST-SQUARE FITTING.
        CALL PRINT('-----DATA SMOOTHING----')
        CALL PRINT('1. YES')
        CALL PRINT('2. NO')
        CALL PRINT('---ENTER YOUR CHOICE---')
        READ(5,*)ISM
        IF(ISM.EQ.2)GO TO 399
        CALL PRINT(' ENTER # OF SMOOTHING PTS')
        CALL PRINT(' 5,7,9,11,13,15,17,19 OR 21')
        READ(5,*)NSMO
399     CONTINUE
        DO 300 MM=1,JROW
        IFILE=MM+70
        READ(IFILE)(((XX(NN,NPTS),NN=1,5),NPTS=1,200),
     1 (XFO(5,NPTS),NPTS=1,200),(XAREA(NN),NN=1,5))
        DO 800 IZ=1,3
800     ZFQ(IZ)=XFO(5,IZ)
        DO 200 NN=1,JCOL
C       ASSIGN PTS ALONG FQ COORD WITH .0045 INCR
C       AND FIND CORRESPONDING INTENSITIES.
240     AFQ(1)=.572
        DO 310 I=2,150
310     AFQ(I)=AFQ(I-1)+.0045
        DO 315 I=1,NPTS
315     SIGN(I)=(SIG(I)/SAREA)*XAREA(NN)
        DO 390 JA=1,150
        DO 380 I=6,NPTSS
        IF(FQA(I).LT.AFQ(JA)) GO TO 380
        IF(FQA(I).GT.AFQ(JA)) GO TO 320
        ASIG(JA)=SIGN(I)
        GO TO 390
320     FQG=FQA(I)-FQA(I-1)
        FQGG=AFQ(JA)-FQA(I-1)
        ASIG(JA)=SIGN(I-1)+((SIGN(I)-SIGN(I-1))*(FQGG/FQG))
        GO TO 390
```

```
380     CONTINUE
390     CONTINUE
        AAREA=0.0
        DO 500 I=1,150
        AAREA=AAREA+ASIG(I)
500     CONTINUE
        SAAREA=AAREA
        AAAREA=0.0
        DO 510 I=1,150
        ASIGN=(ASIG(I)/SAAREA)*XAREA(MM)
        AAAREA=AAAREA+ASIGN
510     CONTINUE
        SMAREA(MM)=AAAREA
        SUMDS=0.
        IF(ISM.EQ.1) GO TO 750
        DO 150 J=1,150
C       MSHIFT=(AFQ(1)-XFQ(MM,1))/VINC
C       MSHIFT=(.572-.500)/.0045=  16
        MSHIFT=16
        JJ=J+MSHIFT
        D(J)=XX(MM,JJ)-ASIG(J)
        IF(D(J)-(1.0E17))130,150,150
130     D(J)=(D(J)**2)
        IF(D(J)-(1.0E35))135,150,150
135     SUMDS=SUMDS+D(J)
D       WRITE(5,140)J,SIG(J),SIGM(J),XX(MM,JJ),SUMDS
140     FORMAT(1X,I3,2X,3(F6.1,2X),E9.2)
150     CONTINUE
        GO TO 190
C
C       THIRD-DEGREE POLYNOMIAL SMOOTINNG.
750     CALL SMOOTH(150,MSMO,ASIG,SSIG)
        DO 770 J=1,150
        MSHIFT=16
        JJ=J+MSHIFT
        D(J)=XX(MM,JJ)-SSIG(J)
```

```
      IF(D(J)-(1.0E17))760,770,770
760   D(J)=(D(J)**2)
      IF(D(J)-(1.0E35))765,770,770
765   SUMDS=SUMDS+D(J)
770   CONTINUE
190   SUMD2(MM,NN)=SUMDS
D     CALL LED (NN,'I6')
200   CONTINUE
      WRITE(5,250)MM,(SUMD2(MM,NN),NN=1,5)
250   FORMAT(I4,3X,11(F10.0,1X))
      WRITE(5,255)(SNAREA(N),N=1,5)
      WRITE(5,255)(XAREA(N),N=1,5)
255   FORMAT(7X,11(F10.0,1X))
      DO 210 I=1,3
      XXFQ=ZFQ(I)+NSHIFT*0.0045
      WRITE(5,205)XXFQ,AFQ(I)
205   FORMAT(10X,2(F6.4,2X))
210   CONTINUE
300   CONTINUE
C
C     FIND THE MINIMUM SUM OF SQUARES OF
C     THE DEVIATIONS AND IDENTIFY ROW # AND COLUMN #.
      SUMDMI=SUMD2(1,1)
      DO 450 MM=1,JROW
      DO 400 NN=1,JCOL
      IF(SUMD2(MM,NN)-SUMDMI)360,360,400
360   SUMDMI=SUMD2(MM,NN)
      IROW=MM
      ICOL=NN
400   CONTINUE
450   CONTINUE
      WRITE(5,460)IROW,ICOL
460   FORMAT(//' MINIMUM SUMD2 LOCATED AT ROW',1X,I3,' , COLUMN',1X,I3)
      WRITE(5,470)R(IROW),T(ICOL)
470   FORMAT(' CORRESPONDING RATIO',6X,F9.3/' TEMPERATURE',14X,F9.3//)
```

```
C
C
10    CALL PRINT('ENTER TOTAL PERCENTAGE OF THE PAIR')
      READ(5,*)TOTAL
      PCENT1=(R(IROW)*TOTAL)/(1+R(IROW))
      PCENT2=TOTAL-PCENT1
      CALL PRINT('CALCULATED % OF THE PAIR: ')
      WRITE(5,*)PCENT1,PCENT2
      CALL EXIT
      END
C
C
C
C
C
C     ~~~~~ SUBROUTINE SMOOTH ~~~~~
C
C     PROGRAM TO PERFORM DATA SMOOTHING
C     USING 3RD-DEGREE POLYNOMIAL APPROXIMATION.
C     SMOOTHING PTS: 5, 7, 9, 11, 13, 15, 17, 19 OR 21.
C
C     MARCH 1983.   W.G.TONG.
C
      SUBROUTINE SMOOTH(ND,NSMO,ASIG,SSIG)
      INTEGER*2 C(10,21)
      DIMENSION ASIG(620),SSIG(620),ASG(620)
      DATA C/
     1-3,-2,-21,-36,-11,-78,-21,-136,-171,35,
     212,3,14,9,0,-13,-6,-51,-76,21,
     317,6,39,44,9,42,7,24,9,231,
     412,7,54,69,16,87,18,89,84,429,
     5-3,6,59,84,21,122,27,144,149,143,
     60,3,54,89,24,147,34,189,204,1105,
     70,-2,39,84,25,162,39,224,249,323,
     80,0,14,69,24,167,42,249,284,2261,
     90,0,-21,44,21,162,43,264,309,3059,
     10,0,0,9,16,147,42,269,324,0,
```

```
         10,0,0,-36,9,122,39,264,329,0,
         20,0,0,0,0,87,34,249,324,0,
         30,0,0,0,-11,42,27,224,309,0,
         40,0,0,0,0,-13,18,189,284,0,
         50,0,0,0,0,-78,7,144,249,0,
         60,0,0,0,0,0,-6,89,204,0,
         70,0,0,0,0,0,-21,24,149,0,
         80,0,0,0,0,0,0,-51,84,0,
         90,0,0,0,0,0,0,-136,9,0,
         10,0,0,0,0,0,0,0,-76,0,
         10,0,0,0,0,0,0,0,-171,0/
      NS=(NSMO-3)/2
      NN=(NSMO-1)/2
      DO 20 I=1,ND
20    ASG(I+NN)=ASIG(I)
      DO 10 I=1,NN
      ASG(I)=0.
10    ASG(I+ND+NN)=0.
      DO 50 I=1,ND
      IA=I
      III=1
      SSG=0.
      DO 40 II=1,NSMO
      SSG=SSG+(ASG(IA)*C(NS,III))
      IA=IA+1
40    III=III+1
50    SSIG(I)=SSG/C(10,NS)
      RETURN
      END
```

```
!        INDIRECT COMMAND FILE
!        FOR LARA2
!
!
!        W.G.TONG.
!
SET ERROR NONE
DEL/NOQ LARA2.(LST,SAV)
SQ/NOQ DK:
!
FORT/NOLINENUMBERS/UNITS:15 LARA2
SQ/NOQ DK:
!
!        USING FLOATING POINT PROCESSOR
!        RUN ON PDP 11/45
LINK LARA2,FPLIB
SET ERROR ERROR
DIR LARA2


.
```

```
C      ~~~~~ PROGRAM 6J ~~~~~
C
C      PROGRAM FOR CALCULATING 6J SYMBOLS.
C
C
C      COMPILE AND LINK WITH @6J.
C      1981.   W.G.TONG
C
      PROGRAM 6J
      DIMENSION F(30),SUM(30)
      CALL PRINT('               (                   )')
      CALL PRINT('               (   J1   J2   J3    )')
      CALL PRINT(' 6J SYMBOL =   (                   )')
      CALL PRINT('               (   L1   L2   L3    )')
      CALL PRINT('               (                   )')
      CALL PRINT(' ENTER J1,J2,J3,L1,L2,L3')
      READ(5,*)MJ1,MJ2,MJ3,ML1,ML2,ML3
C
      P=MJ1+MJ2+ML1+ML2
      MP=P
      A=(-1)**MP
C
      CALL DELTA(MJ1,MJ2,MJ3,D)
      D1=D
      CALL DELTA(ML1,ML2,MJ3,D)
      D2=D
      CALL DELTA(ML1,MJ2,ML3,D)
      D3=D
      CALL DELTA(MJ1,ML2,ML3,D)
      D4=D
      D=D1*D2*D3*D4
C
      K=0
30    F1=(-1)**K
C
      I=1
```

```
      F(I)=(NJ1+NJ2+NL1+NL2+1-K)
      IF(F(I).EQ.0.)GO TO 70
40    I=I+1
      F(I)=F(I-1)-1.
      IF(F(I).EQ.0.)GO TO 50
      GO TO 40
50    II=I
      F2=1
      III=II-1
      DO 60 N=1,III
      F2=F2*F(N)
60    CONTINUE
      GO TO 80
70    F2=1.
C
80    I=1
      F(I)=K
      IF(F(I).EQ.0.)GO TO 120
90    I=I+1
      F(I)=F(I-1)-1.
      IF(F(I).EQ.0)GO TO 100
      GO TO 90
100   II=I
      F3=1
      III=II-1
      DO 110 N=1,III
      F3=F3*F(N)
110   CONTINUE
      GO TO 130
120   F3=1.
C
130   I=1
      F(I)=(NJ1+NJ2-NJ3-K)
      IF(F(I)-0)1000,170,140
140   I=I+1
      F(I)=F(I-1)-1
```

```
      IF(F(I).EQ.0.)GO TO 150
      GO TO 140
150   II=I
      F4=1
      III=II-1
      DO 160 N=1,III
      F4=F4*F(N)
160   CONTINUE
      GO TO 180
170   F4=1.
C
180   I=1
      F(I)=(NL1+NL2-NJ3-K)
      IF(F(I)-0)1000,220,190
190   I=I+1
      F(I)=F(I-1)-1.
      IF(F(I).EQ.0)GO TO 200
      GO TO 190
200   II=I
      F5=1
      III=II-1
      DO 210 N=1,III
      F5=F5*F(N)
210   CONTINUE
      GO TO 230
220   F5=1
C
230   I=1
      F(I)=NJ1+NL2-NL3-K
      IF(F(I)-0)1000,270,240
240   I=I+1
      F(I)=F(I-1)-1
      IF(F(I).EQ.0)GO TO 250
      GO TO 240
250   II=I
      F6=1
      III=II-1
      DO 260 N=1,III
```

```
          F6=F6*F(N)
260       CONTINUE
          GO TO 280
270       F6=1.
C
280       I=1
          F(I)=NL1+NJ2-NL3-K
          IF(F(I)-0)1000,320,290
290       I=I+1
          F(I)=F(I-1)-1.
          IF(F(I).EQ.0)GO TO 300
          GO TO 290
300       II=I
          F7=1
          III=II-1
          DO 310 N=1,III
          F7=F7*F(N)
310       CONTINUE
          GO TO 330
320       F7=1.
C
330       I=1
          F(I)=-NJ1-NL1+NJ3+NL3+K
          IF(F(I)-0)900,370,340
340       I=I+1
          F(I)=F(I-1)-1.
          IF(F(I).EQ.0)GO TO 350
          GO TO 340
350       II=I
          F8=1
          III=II-1
          DO 360 N=1,III
          F8=F8*F(N)
360       CONTINUE
          GO TO 380
370       F8=1
```

```
C
380     I=1
        F(I)=-WJ2-WL2+WJ3+WL3+K
        IF(F(I)-0)900,420,390
390     I=I+1
        F(I)=F(I-1)-1.
        IF(F(I).EQ.0)GO TO 400
        GO TO 390
400     II=I
        F9=1
        III=II-1
        DO 410 N=1,III
        F9=F9*F(N)
410     CONTINUE
        GO TO 430
420     F9=1.
C
430     FUP=F1*F2
        FDOWN=F3*F4*F5*F6*F7*F8*F9
        S=FUP/FDOWN
        K=K+1
        SUM(K)=S
        GO TO 990
900     S=0
        K=K+1
        SUM(K)=S
990     CONTINUE
        GO TO 30
1000    KK=K
        S=0
        DO 500 MM=1,KK
        S=S+SUM(MM)
500     CONTINUE
        X=A*D*S
```

```
      XSQ=X**2
      WRITE(5,520)XSQ
520   FORMAT(//,' 6J SYMBOL VALUE =  ',F12.6)
      STOP
      END
```

6J.COM

```
!       INDIRECT COMMAND FILE
!       FOR PROGRAM 6J
!
!
!       W.G.TONG
!
FORT/NOSWAP 6J/LIST
!
LINK 6J,DELTA
DIR 6J.*
```

```
.TYPE DELTA.FOR
C       ***** SUBROUTINE DELTA *****
C
C
C       SUBROUTINE DELTA FOR PROGRAM 6J
C
C
C       M.G.TONG.
C
        SUBROUTINE DELTA(A,B,C,D)
        DIMENSION F(30)
        I=1
        F(I)=(A+B-C)
        IF(F(I).EQ.0) GO TO 32
10      I=I+1
        F(I)=F(I-1)-1.
        IF(F(I).EQ.0) GO TO 20
        GO TO 10
20      II=I
        F1=1
        III=II-1
        DO 30 N=1,III
        F1=F1*F(N)
30      CONTINUE
        GO TO 33
32      F1=1
C
33      I=1
        F(I)=(A-B+C)
        IF(F(I).EQ.0) GO TO 62
40      I=I+1
        F(I)=F(I-1)-1.
        IF(F(I).EQ.0) GO TO 50
        GO TO 40
50      II=I
```

```
      F2=1
      III=II-1
      DO 60 N=1,III
      F2=F2*F(N)
60    CONTINUE
      GO TO 63
62    F2=1
C
63    I=1
      F(I)=(B+C-A)
      IF(F(I).EQ.0) GO TO 92
70    I=I+1
      F(I)=F(I-1)-1
      IF(F(I).EQ.0) GO TO 80
      GO TO 70
80    II=I
      F3=1
      III=II-1
      DO 90 N=1,III
      F3=F3*F(N)
90    CONTINUE
      GO TO 93
92    F3=1.
C
93    I=1
      F(I)=(A+B+C+1)
      IF(F(I).EQ.0) GO TO 122
100   I=I+1
      F(I)=F(I-1)-1.
      IF(F(I).EQ.0) GO TO 110
      GO TO 100
110   II=I
      F4=1
      III=II-1
      DO 120 N=1,III
```

```
      F4=F4*F(N)
120   CONTINUE
      GO TO 123
122   F4=1
123   D=(F1*F2*F3)/F4
      D=D**0.5
      RETURN
      END
```

```
C         ~~~~~ PROGRAM RATIO ~~~~~
C
C         3-D GRAPHICS WITH IMAGE ROTATION.
C         X=FREQUENCY
C         Y=RATIO OF CU63/CU65
C         Z=HYPERFINE INTENSITY
C         FTN FILES PREVIOUSLY ARRANGED.
C
C         COMPILE AND LINK WITH @RATIO.
C         23-JUL-1983.    N.G.TONG
C
          PROGRAM RATIO
          DIMENSION F(66,12),X(66,12)
          DIMENSION Y(66,12)
          DIMENSION XX(15),YY(200)
          DO 10 N=1,12
          IFILE=50+N
          READ(IFILE)(YY(M),M=1,200)
          KK=66
          DO 20 MM=1,200,3
          F(KK,N)=YY(MM)
20        KK=KK-1
10        CONTINUE
          CALL INIPLT(5,10.,7.)
50        CALL PRINT('ENTER XV,YV,ZV')
          READ(5,*)XV,YV,ZV
          CALL PLOT3D(F,X,Y,66,12,10.,5.,XV,YV,ZV,0,0.)
          CALL ENDPLT
          GO TO 50
          STOP
          END
```

```
      RATIO.COM
!        INDIRECT COMMAND FILE
!        FOR PROGRAM RATIO
!
!
!        W.G.TONG
!
SET ERROR NONE
DEL/NOQ RATIO.(OBJ,LST,SAV)
!
R FORTRA
RATIO,TT:=RATIO/L:0/W/U/N:17
^C
SQ/NOQ DK:
!
!        USING FLOATING POINT PROCESSOR.
!        RUN ON PDP 11/45.
!        LINKED WITH 3DLIB GRAPHICS LIBRARY.
LINK RATIO,3DLIB,FPLIB
```

```
C       ***** PROGRAM 3DRT *****
C
C       3-D GRAPHICS WITH IMAGE ROTATION.
C
C       PROGRAM FOR DISPLAYING THE SUM OF SQUARES OF THE
C       DEVIATIONS IN RATIO-TEMPERATURE SURFACE.
C
C       COMPILE AND LINK WITH @3DRT.
C       18-AUG-83.  W.G.TONG
C
        PROGRAM 3DRT
        DIMENSION F(20,10)
        DIMENSION X(20,10),Y(20,10)
        CALL PRINT('ENTER 1.....FTN INPUT')
        CALL PRINT('       2.....TT: INPUT')
        READ(5,*)NIF
        IF(NIF.EQ.2)GO TO 10
        READ(98)((F(NN,MM),NN=1,20),MM=1,10)
        GO TO 110
10      CALL PRINT('ENTER F VALUES OF 1ST ROW')
        DO 100 N=1,20
        CALL PRINT('ENTER 1 F VALUE PER LINE')
        DO 20 M=1,10
        READ(5,30)F(N,M)
30      FORMAT(F11.2)
20      CONTINUE
        CALL PRINT('ENTER F VALUES OF NEXT ROW')
100     CONTINUE
110     CALL INIPLT(5,10.,7.)
200     CALL PRINT('ENTER XV,YV,ZV')
        READ(5,*)XV,YV,ZV
        CALL PRINT('ENTER XSIZE,YSIZE (10.,5.)')
```

```
READ(5,*)XSIZE,YSIZE
CALL PLOT3D(F,X,Y,20,10,XSIZE,YSIZE,XV,YV,ZV,0,0.)
CALL ENDPLT
CALL PRINT('ENTER 1....REPLOT')
CALL PRINT('       2....EXIT')
READ(5,*)NIF
IF(NIF.EQ.1) GO TO 200
WRITE(99)(((F(NNN,MMM),NNN=1,20),MMM=1,10))
STOP
END
```

```
C         ***** PROGRAM GAUSN *****
C
C         PROGRAM FOR SIMULATION OF GAUSSIAN NOISE
C         ON HYPERFINE STRUCTURES.
C         USED FOR CHECKING THE NOISE EFFECT ON
C         RATIO CALCULATIONS.
C
C
C         COMPILE AND LINK WITH @GAUSN
C         FEBRUARY 1984.    W.G.TONG
C
C
          PROGRAM GAUSN
          DIMENSION R1(501),R2(501),ASIG(201),GSIG(201),FG(201)
          DIMENSION P(501),E(501),PINTEG(501),PN(501),PINTGN(501)
          DIMENSION ES(2),PNS(2),XPLUS(501),XMINUS(501)
          DIMENSION EBL(20),EBLN(20),EBLP(20),EBLS(4),EBLPS(4)
          EQUIVALENCE(R1(1),ASIG(1))
          EQUIVALENCE(P(1),XPLUS(1))
          EQUIVALENCE(PINTEG(1),XMINUS(1))
          EQUIVALENCE(PN(1),GSIG(1))
C         E=EPSILON
50        CALL PRINT('')
          CALL PRINT('ENTER SIGMA')
          READ(5,*)SIGMA
          CALL PRINT('ENTER # POINTS. (200)')
          READ(5,*)NP
          NPHALF=NP/2
          ANP=NP
          HALFNP=NPHALF
          ESTART=-(SIGMA*4.)
          EEND=(SIGMA*4.)
          ERANGE=EEND-ESTART
          EINCR=ERANGE/ANP
          CALL PRINT('ENTER II,JJ FOR 1ST RANDOM # GENERATOR')
```

```
        CALL PRINT('(1000,1000)')
        READ(5,*)II,JJ
        DO 100 N=1,NP
        R1(N)=RAN(II,JJ)
100     R2(N)=RAN(1100,1100)
C
C
        PI=3.1415927
        CALL PRINT('')
D       CALL PRINT('AN;X;P;INTEGRAL P;       NORM.P; NORM.INTEGRAL P')
        E(0)=ESTART
        PINTEG(0)=0.0
        ANORM=(1./(((2.*PI)**.5)*SIGMA))
        DO 300 N=1,NP
        E(N)=E(N-1)+EINCR
        P(N)=EXP(-((E(N)**2.)/(2.*(SIGMA**2.))))
        PINTEG(N)=PINTEG(N-1)+P(N)
300     CONTINUE
        DO 400 N=1,NP
        PN(N)=P(N)/(PINTEG(NP))
        PINTGN(N)=PINTEG(N)/(PINTEG(NP))
D       WRITE(5,302)N,E(N),P(N),PINTEG(N),PN(N),PINTGN(N)
400     CONTINUE
302     FORMAT(I4,3F12.5,5X,2F12.5)
C
        CALL INIPLT(5,9.5,8.5)
        CALL WINDOW(1.5,7.5,1.,7.5)
C
C       PLOT NORMALIZED INTEGRATED PROPABILITY VS EPSILON
        CALL PRINT('')
        CALL PRINT('READY ?')
        READ(5,*)IDUM
        CALL VUPORT(E(0),E(NP),0.,PINTGN(NP))
        XTIC=E(NP)/4.
        YTIC=PINTGN(NP)/2.
```

```
      CALL AXIS(XTIC,YTIC,'EPSILON (SIGMA)',15,2,2,'N.I.P',5,2,3)
      CALL LINE(E,PINTON,NP,0,0,0,0)
      CALL ENDPLT
C
C     PLOT PROPABILITY VS EPSILON
      CALL PRINT('')
      CALL PRINT('READY ?')
      READ(5,*)IDUM
      CALL VUPORT(E(0),E(NP),0.,PN(NPHALF))
      XTIC=E(NP)/4.
      YTIC=PN(NPHALF)/2.
      CALL AXIS(XTIC,YTIC,'EPSILON (SIGMA)',15,2,2,'N.P. ',4,2,3)
      DO 450 N=1,NP
      ES(1)=E(N)
      PNS(1)=0.0
      ES(2)=E(N)
      PNS(2)=PN(N)
450   CALL LINE(ES,PNS,2,0,0,0,0)
      CALL ENDPLT
C
C     CALCULATE RANGE OF EPSILON FOR EACH RANDOM NUMBER
D     CALL PRINT('#,RANDOM#,RHALF#,N.INT.P.,N.INT.P.HALF,XPLUS,XMINUS')
      CALL PRINT('#,RANDOM#,XPLUS,XMINUS')
      DO 600 M=1,NP
      R1HALF=R1(M)/2.
      N1=NPHALF+1
      DO 500 N=N1,NP
      PIN=PINTON(N)-PINTON(NPHALF)
      IF(R1HALF.GT.PIN)GO TO 500
      GO TO 550
500   CONTINUE
550   XP=N
      XPLUS(M)=(XP-HALFNP)*EINCR
      XMINUS(M)=-XPLUS(M)
600   CONTINUE
```

```
      CALL PRINT('ENTER 1.PRINT TABLE')
      CALL PRINT('       2.NO TABLE')
      READ(5,*)IPRINT
      IF(IPRINT.EQ.2)GO TO 610
      DO 605 N=1,NP
D     WRITE(5,602)N,R1(N),R1HALF,PINTON(N),PIN,XPLUS(N),XMINUS(N)
605   WRITE(5,302)N,R1(N),XPLUS(N),XMINUS(N)
C
C     CALCULATE # OF RANDOM #(DATA) FOR EACH RANGE OF EPSILON
610   CALL PRINT('')
      CALL PRINT('ENTER EBLOCK FOR CALCN OF % OF TOTAL DATA #')
      READ(5,*)EBLOCK
      EBL(0)=0.0
      DO 700 N=1,NP
      EBL(N)=EBL(N-1)+EBLOCK
      IF(EBL(N).LT.EEND)GO TO 700
      NBL=N
      N=NP
700   CONTINUE
      CALL PRINT('')
      CALL PRINT('#, EPSILON RANGE, # DATA, % DATA')
      DO 800 M=1,NBL
      NN=0
      DO 900 N=1,NP
      IF(XPLUS(N).GT.EBL(M)) GO TO 900
      IF(XPLUS(N).LE.EBL(M-1))GO TO 900
      NN=NN+1
900   CONTINUE
      EBLN(M)=NN
      EBLN(M)=EBLN(M)/2.
C     EBLP=PERCENT OF EBLN
      EBLP(M)=EBLN(M)*(100./ANP)
800   WRITE(5,802)M,EBL(M),EBLN(M),EBLP(M)
802   FORMAT(I5,F12.5,F12.0,F12.5)
C
```

```
C         PLOT % OF TOTAL RANDOM # (DATA) VS EPSILON RANGE
          CALL PRINT('')
          CALL PRINT('READY ?')
          READ(5,*)IDUM
          CALL VUPORT(E(0),E(NP),0.,20.)
          XTIC=E(NP)/4.
          YTIC=10.
          CALL AXIS(XTIC,YTIC,'EPSILON (SIGMA)',15,2,2,'% DATA',6,2,2)
          DO 920 N=1,NBL
          NNBL=NBL+N
          EBL(NNBL)=-EBL(N)
920       EBLP(NNBL)=EBLP(N)
D         EBLS(1)=0.0
D         EBLPS(1)=0.0
D         EBLS(2)=0.0
D         EBLPS(2)=EBL(1)
D         CALL LINE(EBLS,EBLPS,2,0,0,0,0)
          DO 950 N=1,NNBL
          EBLS(1)=EBL(N)
          EBLPS(1)=0.0
          EBLS(2)=EBL(N)
          EBLPS(2)=EBLP(N)
          EBLPS(3)=EBLP(N)
          IF(N.GT.NBL)GO TO 930
          EBLS(3)=EBL(N)-EBLOCK
          GO TO 940
930       EBLS(3)=EBL(N)+EBLOCK
940       EBLS(4)=EBLS(3)
          EBLPS(4)=0.0
950       CALL LINE(EBLS,EBLPS,4,0,0,0,0)
          CALL ENDPLT
C
C
C         ADD GAUSSIAN NOISE TO THE HYPERFINE STRUCTURE
```

```
          CALL PRINT('')
          CALL PRINT('ENTER FTN #, # POINTS')
          READ(5,*)IFILE,NPTS
          READ(IFILE)((ASIG(I),I=1,NPTS),(FQ(I),I=1,NPTS))
          DO 1000 N=1,200
          IF(R2(N).GT..5)GO TO 1100
          GSIG(N)=ASIG(N)+(XMINUS(N)*SIGMA)
          GO TO 1000
1100      GSIG(N)=ASIG(N)+(XPLUS(N)*SIGMA)
1000      CONTINUE
          CALL PRINT('ENTER NEW FTN #')
          READ(5,*)JFILE
          WRITE(JFILE)((GSIG(I),I=1,NPTS),(FQ(I),I=1,NPTS))
          CALL EXIT
          END
```

```
C        ***** PROGRAM GSN3D *****
C
C        3-D GRAPHICS WITH IMAGE ROTATION.
C
C        NOISE CONSIDERATIONS FOR RATIO CALCULATIONS
C        USING GAUSSIAN NOISE SIMULATION.
C        X=FTN FILES
C        Y=VARIOUS AMPLIFICATION OF AMPLITUDE GAUSSIAN NOISE.
C        Z=% ABUNDANCES CALCULATED
C
C
C        COMPILE AND LINK WITH @GSN3D .
C        FEBRUARY 1984.   W.G.TONG
C
         PROGRAM GSN3D
         DIMENSION F(20,29),X(20,29),Y(20,29)
         IX=20
         IY=29
         CALL PRINT('ENTER 1.FTN INPUT(98)')
         CALL PRINT('      2.TT: INPUT')
         READ(5,*)NIF
         CALL PRINT('ENTER XSIZE,YSIZE  (6.,7.5)')
         READ(5,*)XSIZE,YSIZE
         CALL PRINT('ENTER   0.  BOTH LINES.')
         CALL PRINT('        1.  X DIRECTION LINES ONLY')
         CALL PRINT('        2.  Y DIRECTION LINES ONLY')
         READ(5,*)LINE
         IF(NIF.EQ.2) GO TO 10
         READ(98)((F(NN,MM),NN=1,IX),MM=1,IY)
         GO TO 110
10       DO 20 NN=1,IX
         DO 30 MM=1,IY
30       F(NN,MM)=0.
20       CONTINUE
```

```
      CALL PRINT('ENTER F VALUES OF 1ST NONZERO ROW')
      DO 100 M=6,(IY-5)
      CALL PRINT('ENTER ONE F VALUE PER LINE')
      DO 90 N=1,IX
      READ(5,*)F(N,M)
90    CONTINUE
      CALL PRINT('ENTER F VALUES OF NEXT ROW')
      DO 97 I=1,7
      M=M+1
      IF(I.GT.3)GO TO 96
      DO 95 N=1,IX
95    F(N,M)=F(N,M-1)
      GO TO 97
96    F(N,M)=0.0
97    CONTINUE
100   CONTINUE
C
110   CALL INIPLT(5,XSIZE,YSIZE)
200   CALL PRINT('ENTER XV,YV,ZV')
      READ(5,*)XV,YV,ZV
      CALL PLOT3D(F,X,Y,IX,IY,XSIZE,YSIZE,XV,YV,ZV,LINE,0.)
      CALL ENDPLT
      CALL PRINT('ENTER 1.REPLOT')
      CALL PRINT('      2.EXIT')
      READ(5,*)NIF
      IF(NIF.EQ.1) GO TO 200
      WRITE(99)(((F(NNN,MMM),NNN=1,IX),MMM=1,IY))
      CALL EXIT
      END
```

```
      GSN3D.COM
!        INDIRECT COMMAND FILE
!        FOR PROGRAM GSN3D
!
!
!        H.O.TONG
!
SET ERROR NONE
DEL/NOQ GSN3D.(LST,SAV)
!
FORT/NOSWAP GSN3D/LIST
SQ/NOQ DK:
SET ERROR ERROR
!
!        USING FLOATING POINT PROCESSOR
!        RUN ON PDP 11/45
LINK GSN3D,FPLIB,3DLIB
DIR/FULL/ALP


.
```

```
C       ***** PROGRAM PSNAD1 *****
C
C
C       PROGRAM FOR COLLECTING DOPPLER-FREE
C       POLARIZATION SPECTRUM FROM LOCK-IN AMPLIFIER
C       AND LASER FREQUENCY VALUES FROM THE WAVEMETER.
C       SODIUM D1 LINE.
C
C
C       COMPILE AND LINK WITH  @PSNAD1
C       APRIL 1984.    W.G.TONG
C
        PROGRAM PSNAD1
        DIMENSION SIG(650),FO(650)
        WRITE(5,5)
5       FORMAT(' ENTER FILE #, # PTS.')
        READ (5,10)IFILE,NPTS
10      FORMAT(3I6)
C       HIT RETURN KEY TO START
        READ(5,10)ISTART
15      DO 50 I=1,NPTS
        ICMF=0
        CALL SETR (4,0,500.,ICMF)
        CALL WAVE3(FO(I))
        SIG(I)=FLOAT(IADC(0))
        CALL LED(SIG(I),'F6.1')
        IF(FO(I).GT.0.50) GO TO 20
        FO(I)=FO(I)+1.00
20      IF (ICMF.EQ.0)GO TO 20
50      CONTINUE
        IF(IFILE.EQ.0)GO TO 15
        WRITE(IFILE)((SIG(I),I=1,NPTS),(FO(I),I=1,NPTS))
C
C       FREQUENCY COORDINATE
        FOPEAK=16956.12
```

```
      FOBARE=16955.00
      FO(1)=(FOPEAK-FOBARE)-0.45
      FOI=0.05
      DO 54 NW=2,NPTS
      FOD=FO(NW)-FO(NW-1)
      IF(FOD.GT.(FOI)) GO TO 53
      IF(FOD.LT.(-FOI))GO TO 53
      GO TO 54
53    FO(NW)=FO(NW-1)
54    CONTINUE
C
C     DISPLAY THE SPECTRUM.
      CALL INIPLT(5,9.5,8.5)
      CALL WINDOW(1.5,7.5,1.,7.5)
      CALL VUPORT(16955.6,16956.6,-400.,4000.)
      CALL AXIS(.2,400.,'FREQUENCY',9,2,1,'DFPS',4,2,0)
      DO 100 NOR=1,NPTS
100   FO(NOR)=FO(NOR)+FOBARE
      CALL LINE(FO,SIG,180,0,0,0,0)
      CALL ENDPLT
      CALL EXIT
      END
```

```
!        INDIRECT COMMAND FILE
!        FOR PROGRAM PSNAD1
!
!
!        W.G.TONG
!
R FORTRA
PSNAD1,TT:=PSNAD1/L:0/W/U
^C
!
FORTRA WAVE3
SQ/NOQ DK:
!
!        LINKED WITH SUBROUTINE WAVE3.
LINK PSNAD1,WAVE3,3DLIB,SY:LPSLIB
```

```
C       ***** PROGRAM PS3D *****
C
C
C       3-D GRAPHICS WITH IMAGE ROTATION.
C
C       POLARIZATION SPECTROSCOPY
C       SODIUM D1 LINE.
C       X=LASER FREQUENCY
C       Y=DIFFERENT EXTINCTION RATIO,
C         CROSS ANALYZER ROTATION.
C       Z=POLARIZATION SIGNAL
C       FTN FILES PREPARED AND STORED BY GRAPH4.
C
C
C       APRIL-1984.   W.G.TONG
C
        PROGRAM PS3D
        DIMENSION F(60,12),X(60,12)
        DIMENSION Y(60,12)
        DIMENSION XX(15),YY(200)
C       READ DATA FILES PREPARED AND STORED BY GRAPH4 PROGRAM.
        DO 10 N=1,12
        IFILE=70+N
        READ(IFILE)(YY(M),M=1,180)
        KK=60
        DO 20 NN=1,180,3
        F(KK,N)=YY(NN)
20      KK=KK-1
10      CONTINUE
C
        CALL PRINT('ENTER XSIZE,YSIZE.(10.,7.)')
        READ(5,*)XSIZE,YSIZE
        CALL INIPLT(5,XSIZE,YSIZE)
50      CALL PRINT('ENTER XV,YV,ZV')
        READ(5,*)XV,YV,ZV
```

```
C
      CALL PLOT3D(F,X,Y,60,12,XSIZE,YSIZE,XV,YV,ZV,0,0.)
      CALL ENDPLT
      GO TO 50
      STOP
      END
```

```
!       INDIRECT COMMAND FILE
!       FOR PROGRAM PS3D
!
!
!       W.G.TONG
!
SET ERROR NONE
DEL/NOQ PS3D.(OBJ,LST,SAV)
!
R FORTRA
PS3D,TT:=PS3D/L:0/W/U/N:17
^C
SQ/NOQ DK:
!
!       LINKED WITH 3DLIB GRAPHICS LIBRARY.
LINK PS3D,3DLIB
FORT PS3D/LIST
DIR PS3D
```

```
C        ----- PROGRAM GRAPH4 -----
C
C        PLOT OPTOGALVANIC SIGNAL VS LASER FREQUENCY.
C        FOR SODIUM D1 TRANSITION.
C
C        APRIL-1984, W.G.Tong
C
         PROGRAM GRAPH4
         DIMENSION XX(1,201),SSIG(220)
         DIMENSION SIG(200),XAREA(1)
         DIMENSION BLINE(200),SIGN(201)
         DIMENSION FO(201),X(200),ASG(220)
         DIMENSION FOA(200),XFO(1,200)
         DIMENSION AFO(200),ASIG(200)
         DIMENSION XPLT(200),YPLT(200)
         INTEGER*2 C(10,21)
         EQUIVALENCE (BLINE(1),FOA(1))
         EQUIVALENCE (ASIG(1),SSIG(1))
C
         CALL INIPLT(5,10.5,8.5)
         CALL WINDOW(1.5,8.5,.7,7.7)
         CALL VUPORT(16955.6,16956.6,-4000.,4000.)
         CALL ENDPLT
C
601      CALL PRINT('ENTER FILE #, # PTS')
         READ(5,*)IFILE,NPTS
22       NPTSS=NPTS-15
         NSS=NPTSS-5
         READ(IFILE)((X(J),J=1,NPTS),(FO(I),I=1,NPTS))
C
C        FREQUENCY COORDINATE
         FOPEAK=16956.12
         FOBARE=16955.00
         FO(1)=(FOPEAK-FOBARE)-0.45
```

```
      FOI=0.05
      DO 24 NW=2,NPTS
      FOD=FO(NW)-FO(NW-1)
      IF(FOD.GT.(FOI)) GO TO 23
      IF(FOD.LT.(-FOI)) GO TO 23
      GO TO 24
23    FO(NW)=FO(NW-1)
24    CONTINUE
C
C     DETERMINE BASELINE
      CALL PRINT('----BASELINE DETERMINATION----')
      CALL PRINT('1. AUTO')
      CALL PRINT('2. MANUAL')
      CALL PRINT('------ENTER YOUR CHOICE-------')
      READ(5,*,ERR=24)IBASE
      IF(IBASE.EQ.2)GO TO 41
C     AUTO BASELINE DETERMINATION
28    BSTART=0.
      NS=NPTS/20
      DO 30 JJ=1,NS
      BSTART=BSTART+X(JJ)
30    CONTINUE
      BNS=NS
      BSTART=BSTART/BNS
      BEND=0.
      NEN=NPTS-NS+1
      DO 40 JJ=NEN,NPTS
      BEND=BEND+X(JJ)
40    CONTINUE
      BNS=NPTS-NEN+1
      BEND=BEND/BNS
      BPTS=NEN-1
      BINCR=(BEND-BSTART)/BPTS
      DO 44 J=1,NPTS
      BJ=J
```

```
        BLINE(J)=BSTART+(BINCR*BJ)
44      SIG(J)=X(J)-BLINE(J)
        GO TO 55
C       MANUAL BASELINE DETERMINATION
41      CALL PRINT('ENTER STARTPT,ENDPT,#AVE PT')
        READ(5,*,ERR=41)NSTA,NEND,NAVE
        BSTART=0.
        DO 42 JJ=NSTA,NSTA+NAVE
42      BSTART=BSTART+X(JJ)
        BNAVE=NAVE+1
        BSTART=BSTART/BNAVE
        BEND=0.
        DO 43 JJ=NEND,NEND+NAVE
43      BEND=BEND+X(JJ)
        BNAVE=NAVE+1
        BEND=BEND/BNAVE
        BPTS=NEND-NSTA
45      BINCR=(BEND-BSTART)/BPTS
        DO 47 J=1,NSTA
        BJ=J
        BLINE(J)=BSTART-(BINCR*BJ)
47      SIG(J)=X(J)-BLINE(J)
        DO 50 J=NSTA,NPTS
        BJ=J
        BLINE(J)=BSTART+(BINCR*BJ)
        SIG(J)=X(J)-BLINE(J)
50      CONTINUE
        KK=1
        NN=NPTS/20
55      CONTINUE
C
C       DETERMINE THE 1ST PEAK HEIGHT OF THE COLLECTED
C       SPECTRUM AND ITS POSITION ALONG THE
C       WAVENUMBER COORDINATE.
        DIFF(I)=SIG(I)-SIG(I-1)
```

```
      DO 80 I=2,NPTS
      IF(DIFF(I).GT.50.) GO TO 70
      GO TO 80
70    IF(DIFF(I).LT.1.)GO TO 75
      I=I+1
      GO TO 70
75    CONTINUE
      JVV=(I-1)
      SMAX=SIG(I-1)
      I=NPTS
80    CONTINUE
      WRITE(5,90)JVV
90    FORMAT(' 1ST PEAK LOCATED AT PT #',I6,/)
C
C     FIND AREA
      AREA=0.
      DO 100 J=1,NPTS
      AREA=AREA+ABS(SIG(J))
100   CONTINUE
      SAREA=AREA
      CALL PRINT('CALCULATED AREA: ')
      WRITE(5,*)SAREA
      CALL PRINT(' ')
      CALL PRINT('IF NO THEORECTICAL FILE IS AVAILABLE')
      CALL PRINT('ENTER XAREA(NNN) FOR NORMALIZATION ')
      READ(5,*)XAREA(1)
      NNN=1
C
C     FREQUENCY AVERAGING, 5 PTS.
C     OVERLAP 5 PTS.
      DO 618 I=6,NPTSS
      FOS=0
      DO 612 II=(I-5),(I+5)
612   FOS=FO(II)+FOS
      FO(I)=FOS/11
```

```
        IE=I+5
        FOS=0
        DO 614 II=(IE-5),(IE+5)
614     FOS=FO(II)+FOS
        FO(IE)=FOS/11
        FODIFF=FO(IE)-FO(I)
        FOI=FODIFF/(IE-I)
        FOA(I)=FO(I)
        DO 616 K=(I+1),IE
616     FOA(K)=FOA(K-1)+FOI
        I=I+5
618     CONTINUE
C
C       PLOT FRAME
110     CALL AXIS(.2,400.,'FREQUENCY',9,2,1,'DFPS',4,2,0)
D       CALL PLTSTR(250,530,'HYPERFINE STRUCTURE',19,1,2)
        CALL ENDPLT
C
        CALL PRINT(' -------------GRAPH4 MENU -------------- ')
        CALL PRINT('1. PLOT THEORECTICAL PROFILE')
        CALL PRINT('2. PLOT NORMALIZED, B.SURSTRACTED EXPTL')
        CALL PRINT('3. PLOT BASELINE SUBSTRACTED EXPTL')
        CALL PRINT('4. PLOT ALIGNED, N., B. SUBSTRACTED EXPTL')
        CALL PRINT('5. PLOT ORIGINAL, UNTREATED EXPTL')
        CALL PRINT('6. READ THEORECTICAL PROFILE')
        CALL PRINT('7. READ ANOTHER FTN DATA FILE')
        CALL PRINT('8. EXIT')
        CALL PRINT('----- ENTER ROUTINE # OF YOUR CHOICE ----')
        READ(5,*,ERR=110)LL
        IF(LL.EQ.8)GO TO 603
        IF(LL-6)480,500,601
480     IF(LL-4)490,240,250
490     IF(LL-2)500,580,170
500     CALL PRINT(' ENTER ROW #, COLUMN # OF PT.')
```

```
      READ(5,*,ERR=500)MM,NNN
      IF(MM.GT.0)GO TO 535
      GO TO 600
535   IFILE=MM+70
      READ(IFILE)((XX(1,N1),N1=1,200),(XFO(1,N2),N2=1,200),XAREA(1))
      IF(LL.EQ.6) GO TO 110
C
C     THEORETICAL DOPPLER PROFILE.
      DO 536 NTH=1,200
536   XFO(1,NTH)=XFO(1,NTH)+FOBARE
      CALL LINE(XFO,XX,180,0,0,0,0)
D     CALL PLTSTR(350,420,'THEORECTICAL',12,1,1)
      CALL ENDPLT
      GO TO 110
C
C     NORMALIZED, BASELINE SUBSTRACTED EXPT'L PROFILE.
580   DO 150 J=6,NPTSS
      SIGN(J)=(SIG(J)/SAREA)*XAREA(NNN)
      XPLT(J)=FOA(J)+FOBARE
150   YPLT(J)=SIGN(J)
152   CALL PEAKDI(YPLT,6,NPTSS)
      CALL MENU(LINTYP)
      CALL DASHLN(XPLT,YPLT,NSS,0,0,0,0,LINTYP)
      CALL ENDPLT
      GO TO 110
C
C     BASELINE SUBSTRACTED EXPT'L PROFILE.
170   DO 172 J=6,NPTSS
      XPLT(J)=FOA(J)+FOBARE
172   YPLT(J)=SIG(J)
      CALL MENU(LINTYP)
      CALL DASHLN(XPLT,YPLT,NSS,0,0,0,0,LINTYP)
      CALL ENDPLT
      GO TO 110
C
```

```
C         ALIGNED,NORMALIZED,BASELINE SUBSTRACTED EXPT L PROFILE.
C         ASSIGN PTS ALONG FO COORD WITH .0050 INCR FOR 1.0/200 PT  SCAN
C         AND FIND CORRESPONDING INTENSITIES.
240       CALL PRINT('-----PLEASE WAIT-----')
C         AFO(1)=.650 FOR NA D1 LINE
          AFO(1)=.650
          DO 310 I=2,NSS
310       AFO(I)=AFO(I-1)+.0050
          DO 315 I=5,NPTSS
315       SIGN(I)=(SIG(I)/SAREA)*XAREA(NNN)
          DO 390 JA=1,NSS
          DO 380 I=6,NPTSS
          IF(FOA(I).LT.AFO(JA)) GO TO 380
          IF(FOA(I).GT.AFO(JA)) GO TO 320
          ASIG(JA)=SIGN(I)
          GO TO 390
320       FOG=FOA(I)-FOA(I-1)
          FOGG=AFO(JA)-FOA(I-1)
          ASIG(JA)=SIGN(I-1)+((SIGN(I)-SIGN(I-1))*(FOGG/FOG))
          GO TO 390
380       CONTINUE
390       CONTINUE
          CALL PRINT('-----DATA SMOOTHING----')
          CALL PRINT('1. YES')
          CALL PRINT('2. NO')
          CALL PRINT('---ENTER YOUR CHOICE---')
          READ(5,*,ERR=390)ISM
          IF(ISM.EQ.1) GO TO 248
          DO 402 J=1,NSS
          XPLT(J)=AFO(J)+FOBARE
402       YPLT(J)=ASIG(J)
          CALL MENU(LINTYP)
          CALL DASHLN(XPLT,YPLT,NSS,0,0,0,0,LINTYP)
D         CALL PLTSTR(350,410,'ALIGNED EXPTL',13,1,1)
```

```
      CALL ENDPLT
      GO TO 110
C
C     SMOOTHED,NORM'D,B SUBSTRACTED EXPT'L PROFILE
248   CALL PRINT(' ENTER # OF SMOOTHING PTS')
      CALL PRINT(' 5,7,9,11,13,15,17,19 OR 21')
      READ(5,*)NSMO
      CALL SMOOTH(NSS,NSMO,ASIG,SSIG)
      DO 702 J=1,NSS
      XPLT(J)=AFQ(J)+FQBARE
702   YPLT(J)=SSIG(J)
      CALL PEAKDI(YPLT,1,NSS)
      CALL MENU(LINTYP)
      CALL DASHLN(XPLT,YPLT,NSS,0,0,0,0,LINTYP)
D     CALL PLTSTR(350,410,'SMOOTHED, AL. EXPTL',19,1,1)
      CALL ENDPLT
C
C     STORE THE SMOOTHED FILE
      CALL STORE(AFQ,YPLT,IFTN,NSTORE,NSS)
      GO TO 110
C
C     ORIGINAL, UNTREATED EXPT'L PROFILE
250   DO 251 NOR=1,NPTS
251   FQ(NOR)=FQ(NOR)+FQBARE
      CALL MENU(LINTYP)
      CALL DASHLN(FQ,X,NPTS,0,0,0,0,LINTYP)
D     CALL PLTSTR(350,400,'ORIGINAL DATA',13,1,1)
      CALL ENDPLT
      GO TO 110
600   CONTINUE
603   CALL EXIT
      END
C
      SUBROUTINE MENU(LINTYP)
      CALL PRINT('----- GRAPH MENU -----')
```

```
      CALL PRINT('1. SOLID LINE PLOT')
      CALL PRINT('2. DASHED LINE PLOT')
      CALL PRINT('-- ENTER YOUR CHOICE --')
      READ(5,*)ISD
      IF(ISD.EQ.2) GO TO 1000
      LINTYP=0
      GO TO 1100
1000  LINTYP=4
1100  RETURN
      STOP
      END
C
      SUBROUTINE PEAKDI(YPLT,N1,N2)
      DIMENSION YPLT(200)
      CALL PRINT('----- PEAD DIRECTION -----')
      CALL PRINT(' 1. PLOT ORIGINAL DIRECTION')
      CALL PRINT(' 2. FLIP PEAK UPSIDE DOWN')
      CALL PRINT('-- ENTER YOUR CHOICE --')
      READ(5,*)IDIREC
      IF(IDIREC.EQ.1) GO TO 1150
      DO 1120 J=N1,N2
1120  YPLT(J)=-(YPLT(J))
1150  RETURN
      STOP
      END
C
      SUBROUTINE STORE(AFO,YPLT,IFTN,NSTORE,NSS)
      DIMENSION AFO(200),YPLT(200)
      CALL PRINT('----- GRAPH STORE -----')
      CALL PRINT('1. NO DATA STORAGE')
      CALL PRINT('2. STORE DATA.')
      CALL PRINT('-- ENTER YOUR CHOICE --')
      READ(5,*)NSTORE
      IF(NSTORE.EQ.1) GO TO 1200
```

```
        CALL PRINT('ENTER NEW FTN # AND # POINTS')
        CALL PRINT('AVAILABLE NPTS IS:')
        WRITE(5,*)NSS
        READ(5,*)IFTN,NSTORE
        WRITE(IFTN)((TPLT(I),I=1,NSTORE),(AFO(J),J=1,NSTORE))
1200    RETURN
        STOP
        END


.

.TYPE GRAPH4.COM
!       COMMAND FILE FOR GRAPH4
!
!       NGTong
!       APRIL-1984
!
SET ERROR NONE
DEL/NOQ GRAPH4.(LST,SAV)
SQ/NOQ DK:
SET ERROR ERROR
FORT/NOLINENUMBERS/UNITS:14 GRAPH4
SQ/NOQ DK:
LINK GRAPH4,SMOOTH,3DLIB
!
SET USR SWAP
UNLOAD LS


.
```

```
C     ***** PROGRAM PS3D2 *****
C
C
C     3-D GRAPHICS WITH IMAGE ROTATION.
C
C     POLARIZATION SPECTROSCOPY
C     SODIUM D1 LINE.
C     X=FREQUENCY
C     Y=DIFFERENT POCKEL CELL MODULATION VOLTAGE PAIR,
C       CONSTANT VOLTAGE GAP 140V.
C     Z=POLARIZATION SIGNAL
C     FTN FILES PREPARED BY PROGRAM GRAPH4.
C
C
C     APRIL-1984.   W.G.Tong
C
      PROGRAM PS3D2
      DIMENSION F(60,9),X(60,9)
      DIMENSION Y(60,9)
      DIMENSION XX(15),YY(200)
C     READ DATA FILES PREPARED AND STORED BY GRAPH4 PROGRAM.
      DO 10 N=1,9
      IFILE=90+N
      READ(IFILE)(YY(M),M=1,180)
      KK=60
      DO 20 NN=1,180,3
      F(KK,N)=YY(NN)
20    KK=KK-1
10    CONTINUE
C
      CALL PRINT('ENTER XSIZE,YSIZE.(10.,7.)')
      READ(5,*)XSIZE,YSIZE
      CALL INIPLT(5,XSIZE,YSIZE)
50    CALL PRINT('ENTER XV,YV,ZV')
```

```
          READ(5,*)XV,YV,ZV
C
          CALL PLOT3D(F,X,Y,60,9,XSIZE,YSIZE,XV,YV,ZV,0,0.)
          CALL ENDPLT
          GO TO 50
          STOP
          END


.



!         INDIRECT COMMAND FILE
!         FOR PROGRAM PS3D2
!
!
!         W.G.TONG
!
SET ERROR NONE
DEL/NOQ PS3D2.(OBJ,LST,SAV)
!
R FORTRA
PS3D2,TT:=PS3D2/L:0/W/U/N:17
^C
SQ/NOQ DK:
!
LINK PS3D2,3DLIB
DIR PS3D2


.
```